THE MAGELLANIC STREAM

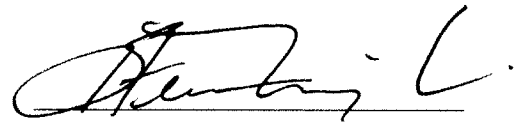David Lee Nidever
Charlottesville, Virginia

B.S./B.A., San Francisco State University, 2000

M.S., University of Virginia, 2006

A Dissertation Presented to the Graduate
Faculty of the University of Virginia
in Candidacy for the Degree of
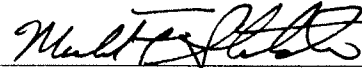Doctor of Philosophy

Department of Astronomy
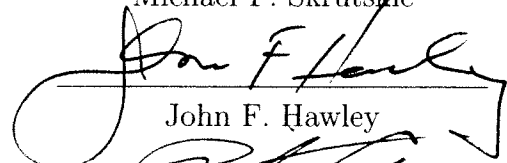
University of Virginia
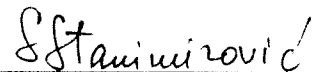December, 2009

Steven R. Majewski

W. Butler Burton

Michael F. Skrutskie

John F. Hawley

Peter Arnold

Snežana Stanimirović

Abstract

We have performed a detailed HI study of the Magellanic Stream (MS). Using the LAB all-sky HI survey, we expose the MS to be composed of two filaments distinct both spatially (as first pointed out by Putman et al. 2003) and in velocity. One of the MS filaments and parts of the Leading Arm (LA) can be traced back to their origin in the SouthEast HI Overdensity (SEHO) of the LMC, which includes 30 Doradus. Therefore, at least one-half of the trailing Stream and most of the LA originates in the LMC, contrary to previous assertions that they originate in the SMC and/or in the Magellanic Bridge. The two MS filaments show periodic spatial and velocity patterns that we speculate are an imprint of the LMC rotation curve. If true, then the drift rate of the Stream gas away from the Magellanic Clouds is $\sim$49 km s^{-1} and the age of the MS is $\sim$1.74 Gyr. High-resolution HI data of the LMC show gas outflows from supergiant shells in the SEHO that seem to be creating the LA and LMC filament of the MS. We lay out a new model, the "Blowout Hypothesis", for the formation of the MS that fits all of the available data and solves some longstanding problems. We also conducted a $\sim$200 deg^2 HI survey with the GBT at the tip of the MS in order to bridge the gap between the $\sim$100°–long "classical" MS and the MS–like emission reported by Braun & Thilker (2004). Our survey shows that the MS gas is continuous across the gap and that the MS is at least $\sim$140° long. A previously unknown velocity inflection in the MS-tip is also revealed in the data. The mass of the newly-found $\sim$40° extension of the MS–tip is $\sim$5$\times$10^7 M$_\odot$ which increases the total mass of the MS by $\sim$10%. We estimate that the age of the $\sim$140°–long MS is $\sim$2.5 Gyr which coincides with bursts of star formation in the Magellanic Clouds and a possible close encounter of these two galaxies with each other. These new observational characteristics of the MS offer additional new constraints on MS simulations.

Acknowledgements

Many people have helped me over the years and I would like to express my gratitude for their support and encouragement.

First, I would like to sincerely thank my adviser Steve Majewski, an admirable scientist, an inspiring teacher and a wonderful mentor. When I first visited the University of Virginia as a prospective student I wasn't sure what topic I wanted to work on in Astronomy. But that soon changed when I heard Steve's talk about using tidal streams around the Milky Way to understand the history of the Galaxy's formation. I knew then that I wanted to come to UVa and work with Steve. Over the years I have learned a great deal from Steve about observational Astronomy and our galaxy, especially how to think about the bigger science questions related to my research. One of my fondest memories of Steve is of observing with him in Chile when we discovered a new Milky Way stellar stream and we spent most of the time there excitedly modeling the stream and writing the paper while at the same time observing for a completely different project of ours.

It is interesting that this thesis started as a class project in Butler Burton's radio Astronomy class my first semester. Many thanks to Butler Burton for encouraging me to study the Magellanic Stream with the Leiden-Argentine-Bonn survey and to pursue publishing it. I also greatly appreciate his help with the GBT project, his advice over the years, and his patience with me as it took so long for me to finish the two Magellanic Stream projects.

I would also like to thank the students and faculty in the Department of Astronomy, and those down the street at NRAO, for providing a positive academic and social environment.

Thanks to my parents for all of their love and encouragement throughout my life.

It's been a strong foundation on which I've been able to build my life since I always knew they would be there for me no matter what happened.

Without the inspiration and mentoring of Erik J. Anderson in my high school science classes in Germany, I probably never would have pursued science in college (I originally wanted to be a mechanical engineer) and I wouldn't have learned the valuable skill of thinking "for myself". I am also grateful to Dr. Steven White and Kathy Harrison for taking me under their wing at Fresno State University and for encouraging me to major in physics. It was in Dr. White's introductory Astronomy class that I first fell in love with Astronomy.

I was fortunate enough to get to work with Geoff Marcy and Debra Fischer at San Francisco State University on the Extrasolar Planets Project. I was extremely excited to work for them and observe for the Project at Lick Observatory. They taught me how to take careful observations and how to program in IDL which is a skill I've been using almost every day for ten years now. It was while working under their tutelage that I realized how much I enjoy Astronomy research. Without the help and experience I gained from working for them I probably wouldn't have pursued a career in Astronomy. I also have Geoff to thank for meeting Amy. It was Geoff, the "matchmaker", that sent Amy observing with me where we became great fiends and eventually fell in love "under the stars".

I will always cherish the long and in depth conversations that I have had over the years with Bill Kunkel. His passion for understanding the Magellanic Clouds helped keep me intrigued in the subject and gave me lots of ideas of how to attempt to understand what's going on in that crazy and fascinating system. I truly marvel over Bill's exuberant mind and I hope I can be as mentally acute as he his when I'm older. He is like a kind grandfather to me and I always look forward to our next meeting.

I am especially thankful to my amazing wife, Amy, for her continual insight, guidance, support, encouragement and love. Without her help I would not have been able to finish this thesis – truly! Special thanks to my baby girl, Eila, who always makes me happy. Whenever I'm down or feeling discouraged about my work I just need some "Eila therapy" to cheer me up again. Amy and Eila are the most special and important pieces of my life. They give my life joy, meaning and purpose, and without them I would be lost.

I would like to thank the internal members of my thesis committee, Steve, Butler, Mike and John, for their guidance and suggestions over the years. I would also like to thank my entire committee for taking the time to read my dissertation and giving me their comments.

Many thanks to the multitude of people with whom I have had useful discussion with over the years about my research on the Magellanic Clouds: Gurtina Besla, Chiara Mastropietro, Erik Muller, John Hibbard, Pavel Kroupa, Remy Indebetouw, Ed Murphy, Zhi-Yun Li, Jake Simon, John Hawley, Jay Lockman, Mary Putman, Lou Nigra, Snežana Stanimirović, and, of course, Amy Reines.

Finally, I am very grateful to the kind ladies of the ARCS Foundation for their support for four years. I am also grateful for the support of a President's fellowship and an academic excellence award from the University of Virginia, a graduate scholarship from the Virginia Space Grant Consortium, and GBT student support from NRAO.

Table of contents

List of Figures

List of Tables

Chapter 1

General Introduction

Under the prevailing concordance cold dark matter cosmology, large structures like galaxies form through hierarchical accretion and merging of dark matter subhalos (e.g., White & Rees 1978; Davis et al. 1985; Navarro, Frenk & White 1996, 1997; Moore et al. 1999). While much of the merging took place at early times, the process of accretion onto large spiral galaxies, such as our Milky Way (MW), continues at a reduced rate until late times (e.g., Bullock & Johnston 2005). Disruption and accretion of small galaxies gives rise to gaseous and stellar tidal streams that continue to orbit the accreting galaxy as fossil relics of the cannibalistic activity. Many striking examples of disruption around our Milky Way have been discovered in recent years: the Pal 5 stream (Odenkirchen et al. 2001; Grillmair & Dionatos 2006); the Sagittarius stream (e.g., Ibata et al. 2001; Newberg et al. 2002; Majewski et al. 2003); the Triangulum-Andromeda overdensity (e.g., Rocha-Pinto et al. 2004; Majewski et al. 2004); the Monoceros stream (e.g., Yanny et al. 2003; Rocha Pinto et al. 2003; Crane et al. 2003); the orphan stream (Belokurov et al. 2006; Grillmair 2006a); and the anticenter stream (Grillmair 2006b). There are likely numerous more such streams of stripped debris remaining to be discovered.

But the most prominent and earliest discovered stream is the Magellanic Stream (MS), which stretches over 100° across the southern sky behind the Large and Small Magellanic Clouds (LMC and SMC). From the mid-1960s onwards there were many efforts to detect high-velocity HI clouds, but Wannier & Wrixon (1972) were the first to recognize the large extent of what was to become known as the Magellanic Stream. Mathewson et al. (1974) associated the Stream with the Magellanic Clouds and more fully demonstrated its ∼100° span. Following these initial discoveries, several investigators observed parts of the MS at high angular resolution and sensitivity (e.g., Haynes 1979; Cohen 1982; Morras 1983, 1985; Wayte 1989; Stanimirović et al. 2002). Putman et al. (2003, hereafter P03) presented the first high angular-resolution maps of the entire MS using the HI Parkes All Sky Survey (HIPASS; Barnes et al. 2001), and, subsequently, Brüns et al. (2005, hereafter Br05) presented both high angular and kinematic resolution data of the entire MS also using Parkes data. Both of these surveys gave the first detailed look into the complex spatial and kinematical structure of the MS. Whereas, except for the MS, all the above mentioned streams are *stellar* and attributed to tidal forces for their origin, the MS is still only recognized as a *gaseous* feature[1] — despite numerous efforts to detect a stellar component of the MS (e.g., Philip 1976a,b; Recillas-Cruz 1982; Brück & Hawkins 1983; Kunkel et al. 1997; Guhathakurta & Reitzel 1998) — and is one such structure whose origin is still debated.

Due to their proximity to each other and as the most massive of the MW satellites, the Magellanic Clouds (MCs) have long been considered to have influenced each other as well as the growth and evolution of their host galaxy. Thus, the MW-LMC-SMC system is regarded as an important laboratory with which to study the

---

[1]There is a sparse stellar population at the location of the Magellanic Bridge feature (Irwin et al. 1990), but their connection to the HI Bridge is unclear, as is the connection of the Bridge to the classical MS.

formation, evolution, and interaction of galaxies and their stellar populations. To this end, extensive mappings of the MCs have recently been conducted at a number of wavelengths. Surveys have been made in HI emission at 21-cm (HIPASS: Barnes et al. 2001; Br05; Staveley-Smith et al. 1997, 2003; Stanimirović et al. 1999; and Muller et al. 2003), in molecular spectral CO lines (NANTEN: Fukui et al. 1999; Mizuno et al. 2001), as well as in the radio continuum (Haynes et al. 1991; Dickel et al. 2005), in the thermal infrared (IRAS: Beichman et al. 1988; MSX: Mill et al. 1994; SAGE: Meixner et al. 2006; S^3MC: Bolatto et al. 2007), in the near-infrared (DENIS: Epchtein et al. 1997; 2MASS: Skrutskie et al. 2006), in broadband optical colors (MCPS: Zaritsky et al. 2002, 2004) as well as in optical emission lines (MCELS: Smith et al. 1998), and at ultraviolet (Smith, Cornett & Hill 1987) and X-ray wavelengths (ROSAT: Snowden & Petre 1994; Chandra and ACIS: Townsley et al. 2006). While these surveys have deepened our understanding of the Clouds themselves — e.g., their star formation history, their stellar content, and their overall structure (van der Marel 2001) — the HI investigations are central to understanding the most obvious product of the MW-MC interaction — the Magellanic Stream.

Obviously, the overall appearance of the MS is shaped by the dynamics of the MCs which are moving almost entirely tangentially in the sky (Kallivayalil et al. 2006a,b; Piatek et al. 2008) and have recently just passed perigalacticon in their polar orbit around the MW (Besla et al. 2007). The earliest dynamical studies of the MCs used the MS to constrain the orbit of the LMC and thereby obtained an LMC space velocity of $\sim$350 km s^{-1} (Murai & Fujimoto 1980; Lin & Lynden-Bell 1982; Heller & Rohlfs 1994). However, most proper motion measurements of the LMC (summarized in van der Marel et al. 2002, hereafter vdM02) have favored a lower space velocity of around 250 km s^{-1}. Murai & Fujimoto (1980), and similar subsequent MS modeling

papers, used these space velocities and an isothermal sphere MW potential to derive orbits for the MCs with an orbital period $\sim$1.5 Gyr and a last apogalacticon distance of $\sim$120 kpc. All of these models agree that the MCs had a close encounter with each other $\sim$200 Myr ago. However, the new HST proper motions of the MCs (Kallivayalil et al. 2006a,b) give MC space velocities $\sim$100 km s^{-1} higher than those produced by the earlier proper motion surveys and that increase the orbital period to $\sim$2–3 Gyr and increase the orbital ellipticity (i.e. the last apogalacticon distance at $\sim$150–200 kpc; Kallivayalil et al. 2006b; Besla et al. 2007). But the addition of a more realistic NFW potential for the MW produces the startling suggestion of *hyperbolic* orbits for the MCs (Besla et al. 2007). Even with a high MW mass model, while the MCs "become bound" again, the LMC orbital period is $\sim$7 Gyr and the last apogalacticon distance is $\sim$400 kpc. Clearly, whether the MCs are bound or not, and the shape of their orbits, has a direct influence on the interactions that produce and shape the MS.

Large-area 21-cm radio surveys have produced most of the information now available about the detailed structure of the MS. Since its discovery as a long stream of HI gas trailing the MCs a number of models have attempted to explain the dynamics and origin of the MS. Early N-body simulations with hundreds of particles by Lin & Lynden-Bell (1977, 1982) and by Murai & Fujimoto (1980) were able to reproduce the general features of the Stream (such as its length and velocity distribution) through tidal stripping by the MW. Later on, it was proposed that the MS could have been created by ram pressure forces (Meurer, Bicknell, & Gingold 1985; Moore & Davis 1994) as the MCs move through the hot gaseous halo of the MW. Ram pressure strips some gas from the Clouds and creates a *trailing* gaseous stream. A persistent problem with the tidal models is that they predict a stellar MS component that, to date, has

not been observed despite numerous efforts. Because ram pressure only affects gas and not stars, these models seemed initially to be more consistent with a gas-only structure.

However, more recent large scale HI surveys have revealed new complexities in the MS that are difficult to account for in a ram pressure model. For example, Putman et al. (1998) used the HIPASS data (Barnes et al. 2001) to discover a gaseous *leading* arm of the MS. This is a feature readily accounted for by the tidal models but creating a leading arm by ram pressure forces remains a formidable problem. The HIPASS data have also shown that the trailing MS is spatially bifurcated (P03), although Cohen (1982) and Morras (1983) previously pointed out that the MS splits into two branches. Mastropietro et al. (2005) performed a large ram pressure+tidal force simulation of the Magellanic Stream (with only the LMC as a progenitor) and were able to reproduce the general features of the Stream, including its extent, shape, column density gradient, and velocity gradient; however, Mastropietro et al. could not reproduce the spatial bifurcation of the Stream nor the Leading Arm Feature. The recent N-body tidal simulations by Connors et al. (2004, 2006), in which most particles are stripped from the SMC during a close encounter with the LMC and MW ∼1.5 Gyr ago, give the closest reproduction of the Stream to date, including the spatial bifurcation of the Stream, the Leading Arm (and its bent shape), and the MS velocity distribution. However, a problem with most tidal models, including those by Connors et al., is that they have trouble reproducing the column density gradient along the Stream, whereas ram pressure models match this particular feature of the observations better, and, of course, account for an entirely gaseous Stream. While there is some evidence that stellar tails may be offset (or completely missing) from the gaseous tails in tidally interacting galaxies (Mihos 2001; Hibbard, Vacca, & Yun

2000), the study of Johnston (1998) indicates that stellar debris from the LMC should have already been found.

Most of the current literature has supported either the SMC or Magellanic Bridge as the source of the MS gas (e.g., P03, B05) since it appears to emanate from these regions in maps of HI column density on the sky. Moreover, the mass of the SMC is much less than that of the LMC (by an order of magnitude) and it is therefore, presumably, much easier for SMC gas to be stripped than LMC gas. Many of the tidal models have used the SMC-origin assumption in their N-body simulations (Gardiner & Noguchi 1996; Yoshizawa & Noguchi 2003; Connors et al. 2004, 2006). On the other hand, Mastropietro et al. were able to reproduce the general characteristics of the MS by ram pressure stripping from the LMC alone. Therefore, the exact origin site of the MS remains unclear.

Recently, Braun & Thilker (2004, hereafter BT04) conducted a deep and wide-field HI survey of the M31 region with the Westerbork Synthesis Radio Telescope (WSRT). They serendipitously discovered some faint emission in the western portion of their survey that appeared to be consistent with a spatial and kinematical extension of the MS, but at much lower column densities. This suggested that the MS was plausibly longer than previously recognized. However, a $\sim 10°$ gap between the "classical" MS and the BT04 survey left the MS affiliation of the BT04 gas somewhat uncertain (see BT04 Fig. 5 and our Fig. 3.5).

The Besla et al. (2007) orbit simulations indicate that the MCs have spent most of their lives isolated from the MW, a scenario that has major consequences for the viability of the two primary MS formation mechanisms – ram pressure stripping and tidal stripping. To effectively remove the MS gas, both of these mechanisms require the MCs to be relatively close to the MW for a prolonged encounter time. If the

orbits of the MCs, as suggested by Besla et al. (2007), have kept them more isolated in the past, then it becomes difficult for either ram pressure or tidal forces to create the MS. The finding of an even longer MS would exacerbate this problem for the two standard mechanisms since a greater length would require gas to be pulled out of the MCs at even larger MW–distances where the density of a ram pressure medium and tidal forces are even lower.

The goal of this thesis is to study the spatial and kinematical structure of the MS and attempt to answer many of the outstanding questions related to the Stream and the Magellanic Clouds: (1) where do the MS and LAF originate, (2) what formation mechanism creates the MS, (3) how old is the MS, (4) how long is the MS, and (5) are the MCs bound to the MW.

In Chapter 2, we use a Gaussian decomposition of the Leiden-Argentine-Bonn HI all-sky survey (LAB; Kalberla et al. 2005) to investigate the origin and formation mechanism of the Magellanic Stream and the Leading Arm. We present new features of the MS, answer the question of where the MS originates, and postulate a new MS formation mechanism that is consistent with all currently available data and solves some of the problems with previous MS formation mechanisms. This study was published in May 2008 in *The Astrophysical Journal*, 679, 432-459.

In Chapter 3, we investigate the length of the MS with our 200 deg^2 GBT HI survey of the gap between the "classical" MS and the MS–like emission reported by BT04. We show that the MS is continuous across the gap and that the MS is therefore much longer than previously thought. The relevance of this result to the MS formation mechanisms and orbits of the MCs is discussed. This study has been submitted to *The Astrophysical Journal* for publication.

In Chapter 4, we summarize our results and further discuss their relevance to the

Magellanic Clouds. We also discuss other projects, beyond the scope of this thesis, that we are pursuing in order to answer other questions pertaining to the Magellanic Clouds and the Magellanic Stream.

Chapter 2

The Origin of the Magellanic Stream and Its Leading Arm

2.1 Introduction

In this project we follow the tradition of using large-area 21-cm data to investigate the relation of the MS and the MCs. We take advantage of the high velocity resolution of the Leiden-Argentine-Bonn (LAB) HI datacube (Kalberla et al. 2005) to investigate the detailed structure of both the leading and trailing arms of the MS across their entire known length. Particular attention is paid to disentangling MS features from other overlapping structures in the datacube, including the MW disk, other Intermediate- and High-Velocity Clouds, and the MCs themselves. This has allowed us to uncover several key aspects of the MS that differ from the earlier interpretations and models of the MS and that lead us to a new mechanism to explain the origin of the Stream.

First, we show that one of the two trailing MS filaments as well as the Leading Arm originate in the LMC, *not* in the SMC or in the Bridge as previously suggested.

Moreover, the specific site that is the source of this gas we identify as the South-East H I Overdensity (SEHO), a region of dense H I and intense star-formation in the southeast of the LMC. Analysis of the high spatial resolution H I Parkes data of the LMC (Staveley-Smith et al. 2003) indicates that supergiant shells in the SEHO are probably responsible for blowing out much of the gas from the LMC, creating (at least one of) the filaments of the MS and Leading Arm. Once blown out and free of the gravitational grip of the LMC, the gas experiences tidal stretching from the MW potential and separates into the leading and trailing components. This blowout mechanism for releasing Magellanic gas represents an alternative to the tidal and ram pressure models. Finally, we propose that the periodic sinusoidal weaving of the trailing Stream filament may be a result of the off-center position of the SEHO in the rotating LMC disk. Coupled with knowledge of the rotation period of the LMC at the SEHO radius, we can use the sinusoidal patterns to estimate the total age of the MS as $\sim$1.74 Gyr under the proposed scenario.

2.2 Brief Description of Leiden-Argentine-Bonn (LAB) data

The Leiden-Argentine-Bonn all-sky H I survey (Kalberla et al. 2005) is a combination of the Leiden/Dwingeloo Survey (LDS: Hartmann & Burton 1997), covering the sky north of $\delta = -30°$, and the Instituto Argentino de Radioastronomía Survey (IAR: Arnal et al. 2000; Bajaja et al. 2005) at more southern declinations. The combined material has a velocity resolution of 1.3 km s^{-1}, a spatial resolution of 36$'$ on a grid spacing of 0°.5 in Galactic latitude (b) and 0°.5/cos(b) in Galactic longitude (l), and is corrected for stray radiation. The velocity range of -450 km s^{-1} to $+400$ km s^{-1} is

adequate for (almost) all Galactic work. The root mean square noise is 0.09 K. Here, we exploit the extensive sky coverage of the LAB data and its relatively high velocity resolution to follow the MS in detail over its full length, and to unravel its filaments.

2.3 Description of Automated Gaussian Decomposition

To improve our ability to trace structures of the MS and disentangle them from MW gas we wrote an automated Gaussian analysis program in the Interactive Data Language (IDL)[1] using an algorithm similar to that used by Haud (2000). Kalberla & Haud (2006) have also performed a Gaussian decomposition of the LAB database but with different goals, namely the physical interpretation of the structure of High Velocity Clouds. Our use of Gaussian decomposition is predicated upon the expected continuity of the filamentary structures in terms of velocity, position, velocity-dispersion, and integrated column density, which allows us to track features even through complex, crowded HI environments.

The general algorithm to decompose an HI velocity profile into Gaussians proceeds in two stages. In the first stage new Gaussians are added to the model fit until the root mean square of the residuals (observed − fitted profile; rms) drops below the noise level, or any new Gaussians do not improve the model fit significantly (δrms <2%). In the second stage an attempt is made to reduce the number of Gaussians in the fit without increasing rms appreciably. The details of these stages are discussed in the following sections.

One of the benefits of the Gaussian analysis performed here is that faint HI struc-

---

[1]A product of ITT Visual Information Systems, formerly Research Systems, Inc.

tures can be enhanced by plotting the integrated column density of each Gaussian at its central velocity. This avoids spreading the flux of the Gaussian over a range of velocities and instead concentrates it to one point. Figures 2.4, 2.6, 2.9, 2.10, 2.11, 2.14 and 2.17 in this paper use this technique.

2.3.1   Gaussian Fitting

In order to find the best-fitting Gaussian decomposition to a velocity distribution along a given line-of-sight we use the general purpose IDL curve-fitting package MP-FIT written by Craig Markwardt.[2] MPFIT is a set of routines for robust least-squares minimization (curve fitting) based on the MINPACK-1 FORTRAN package.

In order to adopt MPFIT to our purposes we wrote an IDL function that returns the output of the Gaussian function, $T_{\mathrm{B}} = T_{\mathrm{B},0} \exp(-(v - v_0)^2/2\sigma_v^2)$, given an array of velocities and the Gaussian parameters (T_{B}, v_0, and σ_v). The necessary inputs for MPFIT are the set of values for the independent and dependent variables (the observed data: velocity – v, and brightness temperature – T_{B}) and a first guess for the Gaussian parameters. One can also give upper and lower limits for each parameter that is allowed to vary in the fit; this is a useful feature for constraining the Gaussians to meaningful solutions. MPFIT returns the parameters for the best fit, the formal 1-σ uncertainties for those parameters, and χ^2 of the fit. We also used rms (root mean square of the residuals) as another means to ascertain the "goodness" of the fit.

Our Gaussian decomposition program uses MPFIT to fit Gaussians to peaks in the HI profiles or to peaks in the residuals (profile − previous best fit). For the initial guess of the Gaussian parameters for a given single peak we use the height of the peak

---

[2] Available at http://cow.physics.wisc.edu/~craigm/idl/idl.html

for $T_{\text{B},0}$, and the velocity of the peak for v_0. To get an initial guess for σ_v we used the fact that the ratio of the derivative of the Gaussian to itself is a line with a slope of $-1/\sigma_v^2$; $T_{\text{B}}'/T_{\text{B}} = (-1/\sigma_v^2) \times (v - v_0)$. A line was fit to this ratio near the central part of the peak, and σ_v computed from its slope. In MPFIT the parameters were constrained to lie between the limits: $0.01 \text{ K} < T_{\text{B},0} < 2 \times T_{\text{B,max}}$, $v_{\min} < v_0 < v_{\max}$, $0.5 \text{ km s}^{-1} < \sigma_v < \frac{1}{2} \times (v_{\max} - v_{\min})$; where $T_{\text{B,max}}$ is the maximum T_{B} of the whole profile, and $v_{\min}$ and $v_{\max}$ are the minimum and maximum velocities of the whole profile (-450 and $+400 \text{ km s}^{-1}$). $T_{\text{B},0}$ was also constrained so that only peaks higher than a certain threshhold above the noise level were chosen for Gaussian fitting (see §2.3.2 below).

To obtain the noise level we smoothed the HI profile with a [16,16,2] Savitzky-Golay filter (Savitzky & Golay 1964) (where the numbers in brackets refer respectively to the number of data points to the left and right of each point to include in the filter, and the order of the derivative desired) and then subtracted this from the original HI profile to remove any real features. Then we found the standard deviation of points with $|v| > 250 \text{ km s}^{-1}$ after 5σ outliers were rejected. This was used as the noise level for the given HI profile.

2.3.2   Adding New Gaussians

Gaussians were added to the velocity profile fit one at a time. The current best fit was subtracted from the observed HI profile to find the residuals. These residuals were then searched for peaks higher than 5 times the noise level (although this was lowered to 2 times the noise level if no peaks were found) and MPFIT was used to find the best-fitting Gaussian for each peak along with its rms using the first guesses described in the previous section. To smooth over the noise and search for features

on various scales five smoothed versions of the residuals were created using Savitzky-Golay filters of [4,4,2], [16,16,2], [30,30,2], [50,50,2] and [100,100,2] and Gaussians were fit to all the peaks in these smoothed profiles.

The best-fit Gaussians to peaks in the six versions of the residuals (the original and the five smoothed) that had parameters within our acceptble limits (see above) were kept for further fitting. Each one of these candidate Gaussians is taken in turn and added to the current best-fit Gaussian decomposition of the entire HI profile. MPFIT is then rerun with this new Gaussian decomposition as a first guess, fitting the multiple Gaussians at once, and the change of rms compared to the previous best-fit was computed. The candidate Gaussian that gives the greatest decrease in rms is then added to the overall decomposition of the HI profile.

This procedure is repeated and Gaussians added to the decomposition until the rms drops to or below the noise level, or the decrease in rms is less than 2%.

2.3.3   Removing Gaussians

The best-fitting Gaussian decomposition is that which minimizes *both* the rms as well as the number of Gaussians. To achieve this goal, we attempt to remove Gaussians that do not significantly improve the fits to the velocity profiles. The Gaussians in the best-fit decomposition are sorted in order of area ($A = T_{\mathrm{B},0} \times \sigma_v \sqrt{2\pi}$ K km s^{-1}), and the smallest half of the Gaussians were picked for possible removal. Each one in turn was temporarily removed from the decomposition and the new best-fit and rms for the whole profile are found with MPFIT. If the increase in rms is less than 2% the Gaussian is permanently removed from the decomposition. Even though it might appear at first glance that this is repeating work done in the "Adding Gaussians" stage, this particular decomposition might not have been looked

at before because of the order in which Gaussians were added. Gaussians are also removed from the decomposition if two quite similar Gaussians were found at the same velocity. In that case they are replaced by a single Gaussian with parameters given by Equations 11–13 in Haud (2000).

2.3.4   Selecting the Next Position

We initially used the same procedure as Haud (2000) (see his section 3.3) to select the next position on the sky to decompose. If the profile at a neighboring position has already been decomposed but has a worse decomposition (either larger rms or more Gaussians) than the decomposition at the current position, then the program tries to re-decompose the neighboring profile using the best-fit solution of the current position as the initial guess. The scheme also allows the program to wander around re-decomposing HI profiles until the re-decomposition is not an improvement. We found that this "wandering" scheme was too CPU intensive and did not improve the solutions substantially. Therefore, we used a modified scheme that forced the program to return to the previous position after re-decomposing a neighboring position. For new positions, that hadn't been decomposed yet, the best-fit solution at the previous position was always used for the initial guess.

For low latitudes the program was not allowed to re-decompose profiles since it took much longer in these regions. Our program did not take into account any self-absorption, so some low latitude profiles near the Galactic center will not be correctly represented by the Gaussian decomposition. This does not affect our study of the MS here because it should not have significant self-absorption, if any.
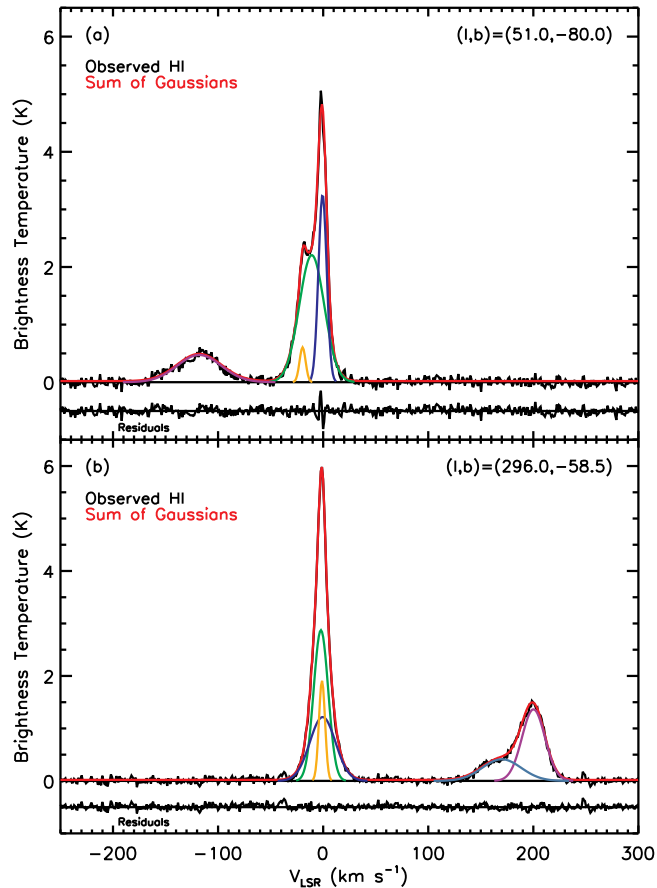
Fig. 2.1.— Examples of Gaussian decomposition for LAB H I profiles (top plot in each panel) and their residuals (bottom plot in each panel). (*a*) The Gaussian decomposition at $(l, b) = (51.0°, -80.0°)$, with four Gaussian components (each shown by a different color, their sum by red), showing the Magellanic Stream at negative velocities. (*b*) The Gaussian decomposition at $(l, b) = (296.0°, -58.5°)$, with five Gaussian components, showing two separated Magellanic Stream components at positive velocities.

2.3.5   Statistics of the Gaussians

Our automated Gaussian decomposition program was run on all 259,920 H I profiles (720 values of l × 361 values of b, in steps of 0°.5) of the LAB all-sky survey. In the end, the entire sky was decomposed into 1,370,801 Gaussians. Several examples of
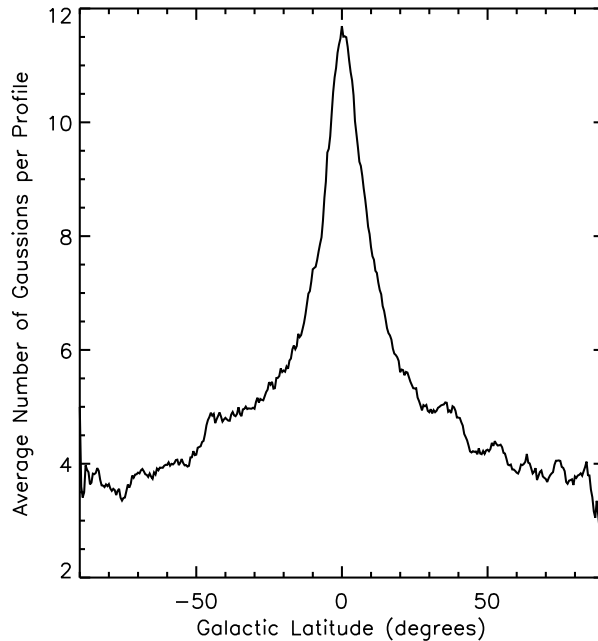
Fig. 2.2.— Average number of Gaussians in the H I decomposition per position as a function of Galactic latitude b.

Gaussian decompositions at various sky positions are shown in Figure 2.1. We find that the majority of H I profiles (at latitudes above the disk, $|b| > 15°$) are well fit with four to six Gaussians. The average number of Gaussians per profile as a function of b is shown in Figure 2.2; the number peaks at 12 at the Galactic center and levels off to four near the poles. The majority of Gaussians at higher latitudes are from local MW, zero-velocity gas. The distribution of fitted Gaussian parameters for various populations are shown in Figure 2.3, a "2D histogram" indicating the number of Gaussians with a particular height ($T_{B,0}$) and Gaussian width (σ_v). An intriguing structure is apparent in the distribution of zero-velocity gas Gaussians in Figure 2.3b following a $1/\sigma_v$ trend (for $8 < \sigma_v < 35$ km s^{-1} and $1 < T_{B,0} < 3$ K) and nearly conserving its area at $\sim$35 K km s^{-1}. It is not clear what this structure corresponds to. The distributions of all Gaussians as a function of l, b, and v_{LSR} are shown in
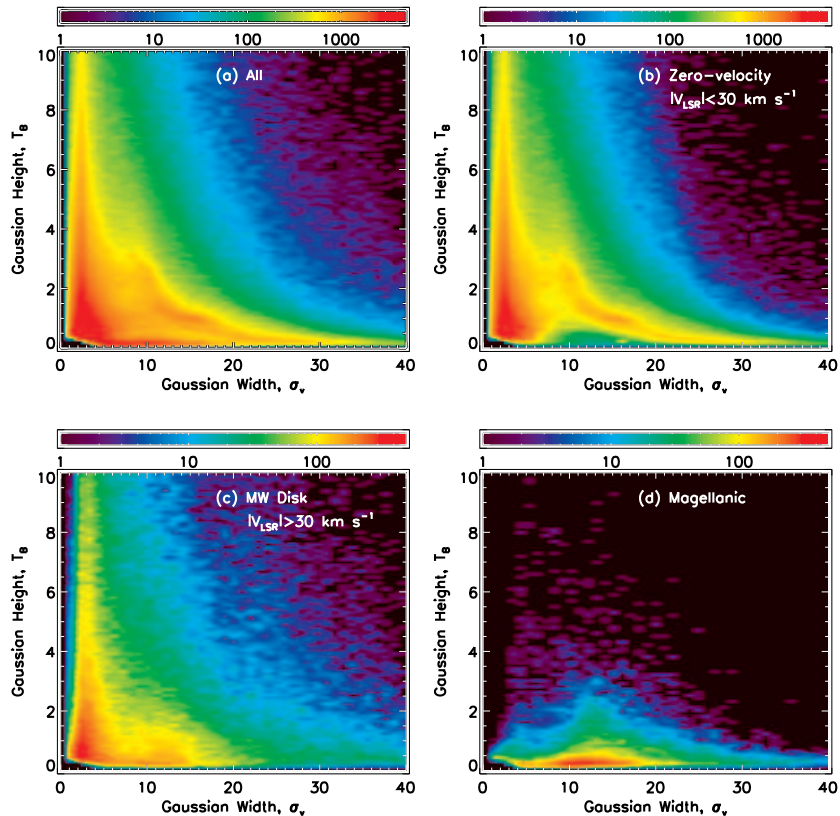
Fig. 2.3.— The distribution of Gaussian parameters (T_B and σ_v) for various HI populations. (a) All Gaussians; (b) local zero-velocity Gaussians ($|V_{LSR}| < 30$ km s^{-1}); (c) Milky Way disk Gaussians with $|V_{LSR}| > 30$ km s^{-1} (see §4.2 for how these are defined); (d) Magellanic Clouds and Stream Gaussians. Note the different color scalings for a+b and c+d.

Figure 2.4. The disk of the MW, the local zero-velocity MW gas, and the Magellanic Clouds and Stream are readily apparent.

2.3.6   Validity of the Gaussian Decomposition

It might be asked whether Gaussian decomposition is the correct way to analyze these data. Though Gaussian decomposition has been widely used as a tool to analyze all forms of HI data going back to the 1960s (e.g., Kaper et al. 1966; Takakubo &
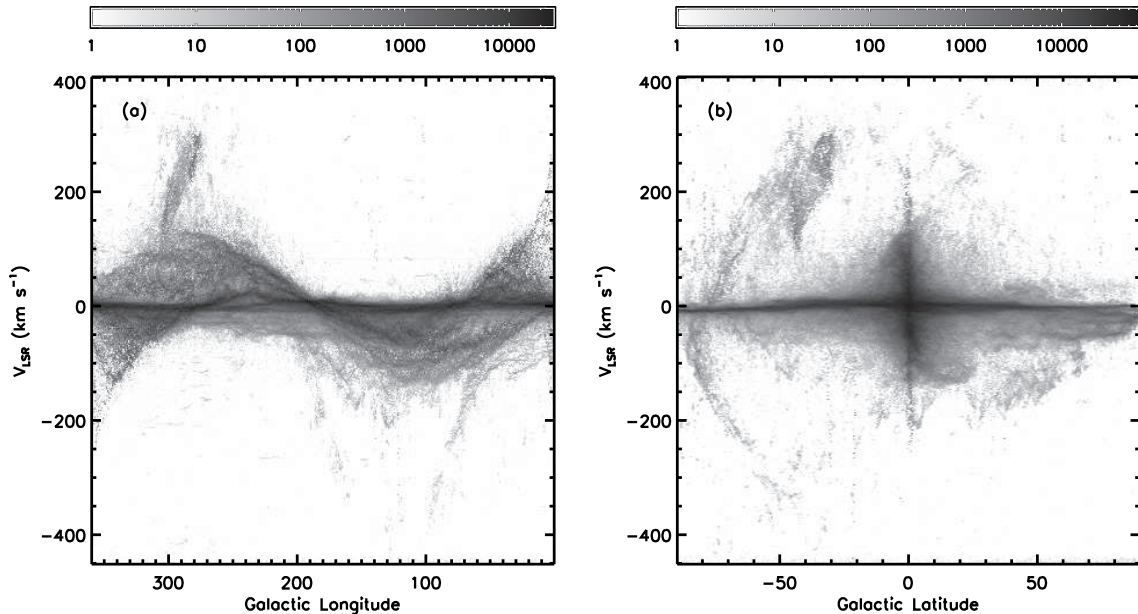
Fig. 2.4.— Position-velocity distribution of detected HI Gaussians in the LAB datacube where each is represented by a single point with weight equal to the Gaussian area and the results summed over all Gaussians. (a) V_{LSR} vs. l, summed along b, showing the characteristic velocity curve of the Milky Way as well as the Magellanic Clouds and Stream at larger velocities; (b) V_{LSR} vs. b, summed along l, showing the zero-velocity gas (even at high latitudes), Milky Way disk ($l \sim 0$), Magellanic Clouds (to upper left) and Stream (arcing on left side). The greyscales are in units of K km s^{-1}.

van Woerden 1966; Burton 1970; Schwarz & van Woerden 1974; see review by Haud 2000), it is only physically well-motivated for isolated, internally virialized clouds, and here it finds its most common application (e.g., Brüns, Kerp & Pagels 2001; Wakker, Oosterloo, & Putman 2002; Kalberla & Haud 2006). In contrast, here we are using Gaussian decomposition primarily as a tool to disentangling overlapping HI structures under the presumption that HI structures along the line-of-sight only slowly vary those properties encapsulated by a Gaussian description (velocity, position, velocity-dispersion, and integrated column density).

We have looked at various isolated HI clouds in the LAB data and found that they

are well-fit by Gaussians. Moreover, by using Gaussians we are able to disentangle different H I filaments even when they are overlapping in velocity. In those situations it is clear that the Gaussian decomposition traces structures that are real and they may even hold physical information about the structures. We are still successful in tracking tenuous structures through even more complicated environments even though the decompositions of those environments (local MW zero-velocity gas, the MW disk, and the Magellanic Clouds) likely holds no physical meaning. Whether or not it holds physical meaning, we are primarily interested in how the Gaussian decomposition provides a representation of the data that enables us to track large features of the MS. In addition the decomposition allows us to reduce our data to a manageable size (from a datacube to a database of Gaussians).

There are a high number of Gaussians with low $T_{\mathrm{B},0}$ and σ_v which are most likely due to fitting of noise features. We make a simple parameter space boundary $T_{\mathrm{B},0} > -0.08\sigma_v + 0.45$ to remove these "noise" Gaussians. The presence of possibly extraneous narrow or wide Gaussians does not influence our interpretation of the LAB data, which is based on significant features in the database.

2.4 Removal of Milky Way gas

In order to study the MS, we need to separate the Gaussians of MS gas from those of MW gas, which is a particulary difficult problem at low $|b|$, and at any latitude when the velocity of the MS differs little from the velocities expected for gas in the conventional MW disk. The velocities of the conventional MW disk gas roughly follow the expectations for material moving in circular orbits around the Galaxy, i.e.

$$V_{\mathrm{LSR}}(l, b, R) = \left[\frac{R_0}{R} V(R) - V_0 \right] \sin(l)\cos(b) \tag{2.1}$$

where V_0 and R_0 are the solar velocity and Galactocentric distance, respectively, and $V(R)$ is the rotation curve at R. At high latitudes the gas is (mostly) concentrated to velocities of $V_{\mathrm{LSR}} \approx 0$ (zero-velocity gas) because the gas is (mostly) nearby, since we are looking out of the plane of the disk, and therefore $R_0/R \sim 1$. Essentially, this gas is local ISM gas moving in nearly the same orbit as the Sun around the MW. At lower latitudes the MW disk gas has a larger range of velocities of approximately, $-V_0\cos(b) < V_{\mathrm{LSR}} < +V_0\cos(b)$, but of course there is a strong $\sin(l)$ dependence. Due to the different characteristics of high-latitude versus low-latitude MW gas different methods were employed to separate them from the MS gas. It is worth emphasizing that ultimately no conclusions in this paper depend on the details or ultimate accuracy of these population decompositions; our care in pursuing these strategies is to make improved maps of the MS.

2.4.1 Zero-Velocity Gas at High Latitudes

At most positions in the sky, the zero-velocity MW disk gas is easily distinguishable from the MS gas because they have very different velocities. However, since the MS stretches from $V_{\mathrm{LSR}} \approx 300$ km s^{-1} to $V_{\mathrm{LSR}} \approx -400$ km s^{-1} it must cross $V_{\mathrm{LSR}} = 0$ at some point. This happens in the region $-84° < b < -78°$ and $288° < l < 327°$. In this area it becomes challenging to distinguish the zero-velocity MW gas from the MS gas. It is difficult to disentangle the two populations of gas without some decomposition scheme as we have used here. Most earlier column density maps of the MS show gaps in this region (see Figs. 4–5 in P03, and Fig. 2 in B05) which we intend to remedy in our maps.
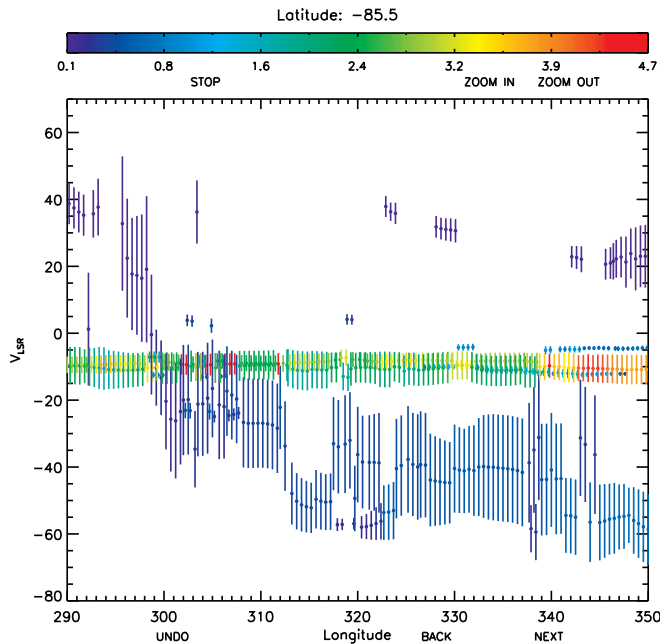
Fig. 2.5.— A snapshot of the analysis used to remove the zero-velocity Milky Way Gaussians in the region where they overlap the Magellanic Stream. At a given Galactic latitude the central velocity of each Gaussian is plotted against its Galactic longitude. Each Gaussian is represented as a line, where its length corresonds to $2\sigma_v$ and the color corresponds to T_B (the colorbar shows the scale). The continuity of features in position, velocity, T_B, and σ_v is used to identify them as due either to local Milky-Way zero-velocity gas or to the Magellanic Stream. An interactive program was developed whereby any Gaussian can be removed from the datacube by clicking on it on the display screen. The labels "STOP", "ZOOM IN", etc. are buttons on the interactive display to perform actions during the Gaussian de-selection process.

We attempted to separate the zero-velocity MW Gaussians from the low-velocity MS Gaussians by using the Gaussian parameters σ_v and $T_{B,0}$ alone, since velocity would not be of much use in this case. However the zero-velocity MW and MS Gaussians also overlap in $\sigma_v - T_{B,0}$ space (see Fig. 2.3) which makes this separation strategy untenable. The zero-velocity gas was eventually removed interactively. We made V_{LSR} vs. l plots of all of the Gaussians at a single b in the region where the MS crosses $V_{LSR} = 0$. Each Gaussian was represented by a vertical line, where the length

of the line corresponded to the Gaussian's $2\sigma_v$ and the color of the line to its $T_{\mathrm{B},0}$. Figure 2.5 shows an example of one of these plots, and demonstrates the relative ease with which such a representation makes it possible to distinguish the MS Gaussians from MW Gaussians because of the nearly-constant, but different, $T_{\mathrm{B},0}$ and σ_v trends for each and the straight versus arcing trends that differentiate them. An interactive program allows us to remove any Gaussian represented in this way by clicking on it. All of the Gaussians consistent with being zero-velocity MW Gaussians were removed at a given b, and the process was repeated for all b where the MS and zero-velocity MW gas overlapped. This process was iterated a few times to ensure that no residual zero-velocity patterns were left over. The results of this zero-velocity MW Gaussian removal scheme can be seen in Figure 2.6. For the regions where there is no overlap between MS gas and Milky Way zero-velocity gas all Gaussians with $|V_{\mathrm{LSR}}| < 45$ km s^{-1} have been removed. A separate scheme was used to remove the MW gas at somewhat higher velocities (i.e. $|V_{\mathrm{LSR}}| > 45$ km s^{-1} which is described in the next section.

2.4.2 Milky Way Disk Gas at Low Latitudes

Since we were interested in investigating the Leading Arm, we also needed to remove the MW gas at low latitudes, because the Leading Arm passes through $b = 0°$. We first attempted to use a simple, symmetric analytical model of the MW to remove the disk gas, but this failed to remove a significant portion of MW gas because of the exaggerated simplicity of the model. We instead adopted an empirical method to remove the disk gas. At a given l and V_{LSR}, the T_{B} due to the MW disk gas drops off quickly with b. The basis for our empirical strategy is to find where this drop-off occurs and call that the end of the disk. We used the profiles from the original HI
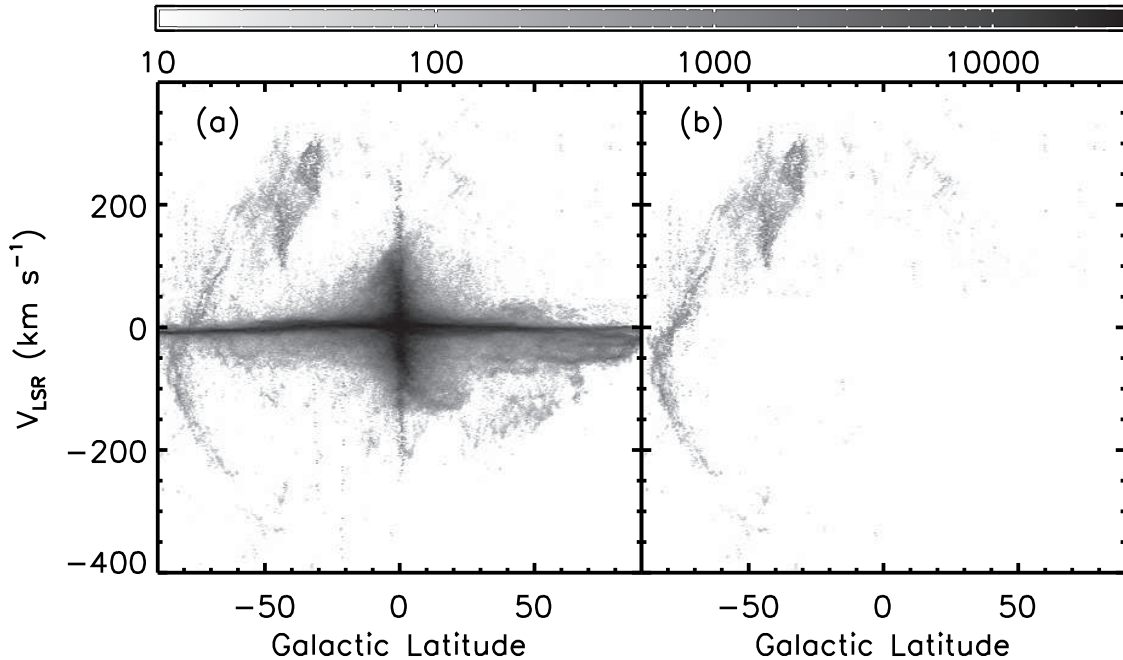
Fig. 2.6.— V_{LSR} vs. b of HI Gaussians (summed along l) (a) before the Milky Way and zero-velocity HI gas has been removed, and (b) after it has been removed. The greyscale is in units of K km s^{-1}.

datacube to accomplish this. In order to see the global trend and remove noise, each profile was smoothed with a Savitzky-Golay [15,15,2] filter. For each l and $V_{\mathrm{LSR}} > 30$ km s^{-1} the "edges" of the disk (where it fell below 5% of the central T_{B} value) in b were found. The values of these "edges" were then used to remove all Gaussians that fell within this b range at that particular l and V_{LSR}. In addition, all Gaussians with $V_{\mathrm{LSR}} < 30$ km s^{-1} have been automatically removed. The Gaussians left-over after the MW disk-gas removal (primarily HVCs, some IVCs, and MS gas) can be seen in Figure 2.7. The distributions of the Gaussian parameters ($T_{\mathrm{B},0}$, σ_v) of the MW disk gas Gaussians and the left-over Gaussians are shown in Figure 2.3c.
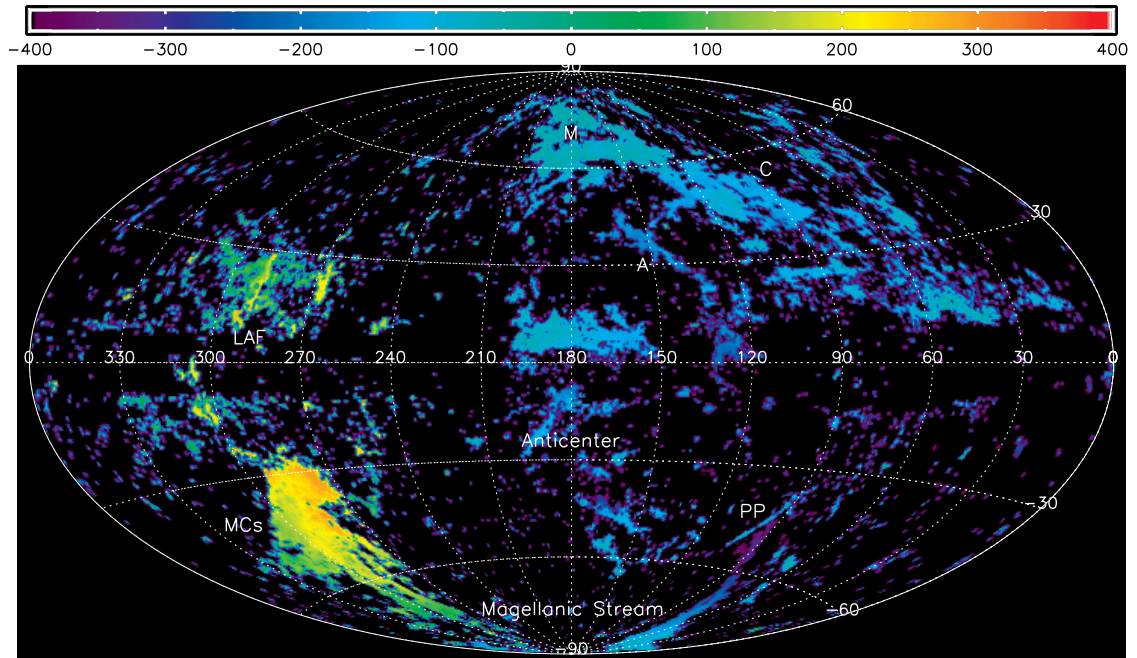
Fig. 2.7.— Sky distribution of IVC and HVC H I gas in Galactic coordinates, where the color represents V_{LSR} in km s^{-1} and the individual Gaussian components are collapsed into single points (compare to Wakker 2004). The Magellanic Clouds (lower left) and Stream (arcing across the bottom) as well as Complex C (upper right) and other HVC complexes are clearly visible.

2.4.3   General Features Observed in the HVC and IVC Distributions

Though a thorough analysis of Figure 2.7 is beyond the scope of this paper, several general characteristics of this figure are worth pointing out, especially in consideration of similar all-sky maps produced earlier. We specifically compare our figure to Figure 1a of Wakker (2004). Many of the same general features may be seen in both maps, but some structures are not consistently seen because different schemes were used to discriminate MW disk from other gas. Wakker employed a symmetric, analytical model for the Milky Way disk, whereas we define and remove the Milky Way gas

empirically. Morever, because of the two to four times higher net spatial resolution of the LAB data, our Figure 2.7 map shows some finer structures, and our colorscale levels reveal more detail because of the > 10 times higher velocity resolution. Most germane to the present discussion is that the tendril-like structure of the MS and Leading Arm Feature (LAF) is more obvious in Figure 2.7 than in the Wakker maps. The same kind of fine-structure is also seen in other HVC complexes in our maps (e.g., Complexes A, C, and M). In this regard, our data are more similar to those of P03 and B05, with only slightly lower spatial resolution, equivalent or higher velocity resolution, but covering the entire sky. It is because of the higher velocity resolution data and the analysis techniques we use to analyze them (§2.3) that we are able to build on P03's previous work on the MS. The B05 data, which are higher in spatial resolution than the LAB data, were unavailable to us when we began this analysis.

2.5 Results of the Gaussian Decomposition

2.5.1 Magellanic Stream Coordinate System

Because the Magellanic Stream consistently follows such a long trace across the sky, it is useful to have a coordinate system for which the equator lies along the great circle of the MS. A Magellanic coordinate system was defined by Wakker (2001), in terms of the great circle along the $l = 90°$ and $l = 270°$ Galactic meridian. Although this is close to the MS, the equator of that coordinate system is not exactly along the Stream. We define here a new coordinate system which we call the "Magellanic Stream" coordinate system and whose equator more closely bisects the Magellanic Stream. The equator of the system was set by finding the great circle best-fitting the MS. The pole of this great circle is at $(l, b) = (188.5°, -7.5°)$; the longitude scale is

defined in such a way that the center of the LMC ($l, b = 280.47°, -32.75°$; van der Marel et al. 2002) has $L_{\rm MS} = 0°$. Like the Magellanic coordinate system of Wakker, $L_{\rm MS}$ decreases along the MS (towards its tail). Many subsequent figures in this paper will use the Magellanic Stream coordinate system ($L_{\rm MS}$, $B_{\rm MS}$).

2.5.2 Representations of the Magellanic Stream

The results of the Gaussian decomposition, with the MW disk gas and local zero-velocity gas removed, can be seen in Figures 2.8 and 2.9, which show integrated intensity of the Gaussians in three perspectives ($B_{\rm MS}$ vs. $L_{\rm MS}$, $V_{\rm LSR}$ vs. $L_{\rm MS}$, $V_{\rm LSR}$ vs. $B_{\rm MS}$). Figure 2.8a also shows the Gaussians of the Magellanic System in $B_{\rm MS}$ vs. $L_{\rm MS}$ with color representing $<V_{\rm LSR}>$. The large velocity gradient is evident in this figure. Figure 2.9b similarly shows the sum of Gaussian centers of the Magellanic System in $V_{\rm LSR}$ vs. $L_{\rm MS}$ with color representing $<B_{\rm MS}>$. Some readily apparent, prominent features in these figures, such as the LMC, SMC, the MS, and the LAF are labeled in Figure 2.8.

2.5.3 The Two Filaments of the Magellanic Stream and their Source

The two-filament structure of the MS, previously pointed out by Cohen (1982) and by Morras (1983), and studied recently by P03, is clearly visible and separated in our datacube of Gaussian centers. The MS filaments can be distinguished between $-40° < L_{\rm MS} < 0°$ in the $V_{\rm LSR}$ vs. $L_{\rm MS}$ plot (Fig. 2.9b). For $L_{\rm MS} < -45°$ it becomes difficult to disentangle the two MS filaments in any projection of the data and we therefore focus here on the $L_{\rm MS} > -45°$ region of the Magellanic System. Figure 2.9 allows us to distinguish both filaments in the head of the Stream. Until now the
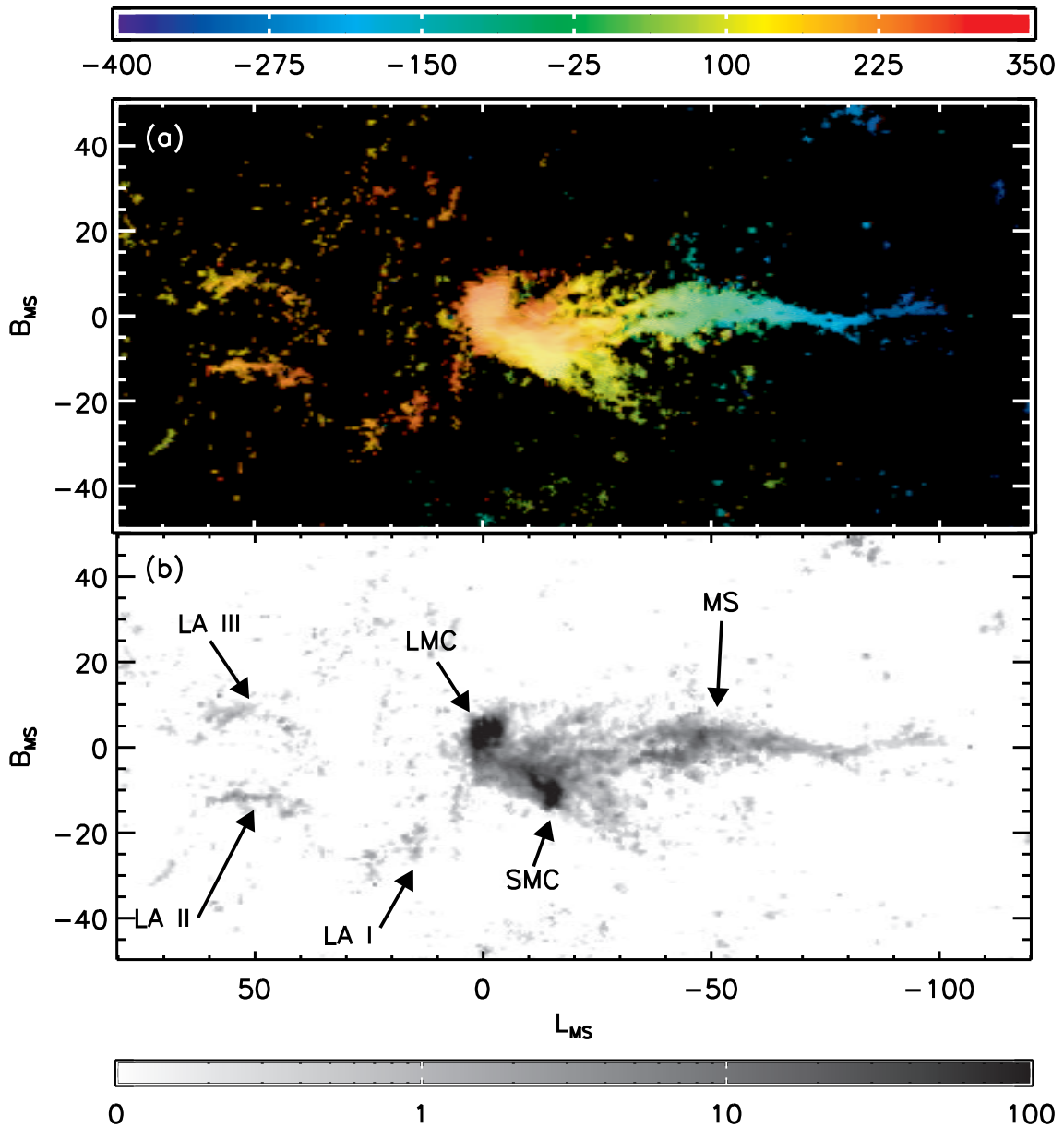
Fig. 2.8.— The Magellanic Clouds and Stream HI Gaussians as distributed on the sky. (*a*) Hue indicates $<V_{\mathrm{LSR}}>$ and intensity indicates N_{HI} (on a logarithmic scale). (*b*) The three Leading Arm complexes I–III (including the three "clumps" of LA I clearly seen in panel (*a*)), the Large Magellanic Cloud (LMC), Small Magellanic Cloud (SMC), and the Magellanic Stream (MS) are shown in this greyscale representation of HI column density, N_{HI}, in units of 10^{19} atoms cm^{-2}.
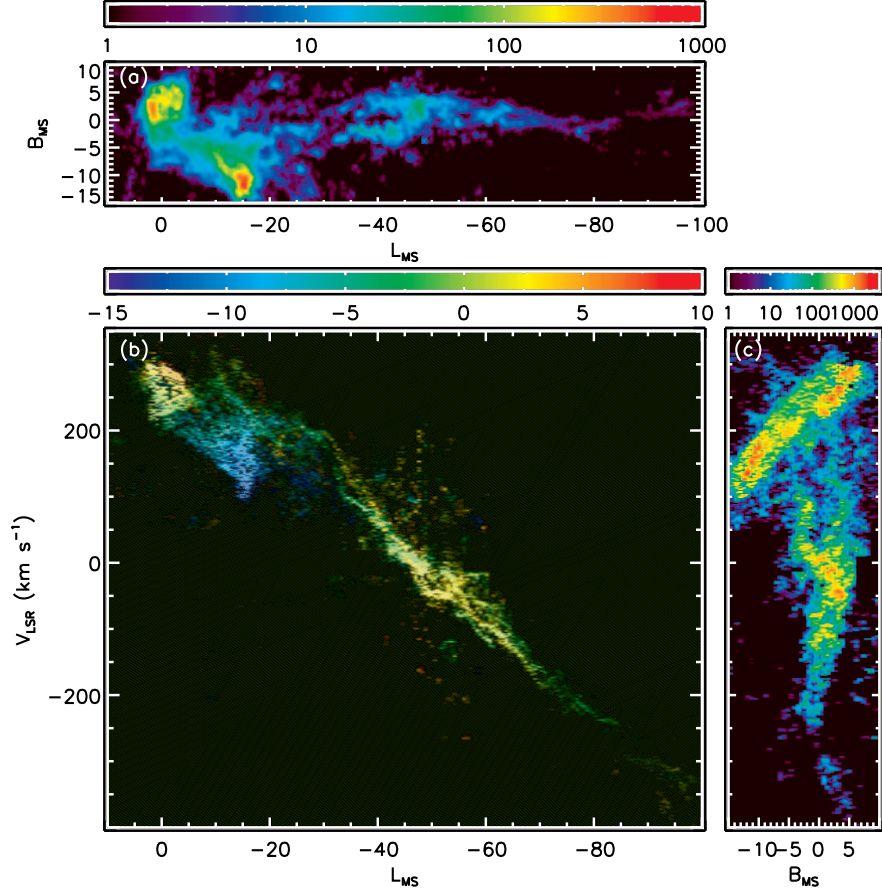
Fig. 2.9.— Integrated intensity (sum of Gaussian areas) of the Magellanic Cloud and Stream H I Gaussians (at their central V_{LSR} velocity). (a) Column density, N_{HI}, in units of 10^{19} atoms cm^{-2} (a blowup of Figure 2.8b). A spatial bifurcation of the Magellanic Stream into two filaments (first pointed out by P03) can be seen for $-40° < L_{\mathrm{MS}} < -20°$. Other bifurcations are seen farther down the Stream. (b) V_{LSR} vs. L_{MS} (hue indicates B_{MS}, and brightness indicates integrated intensity along B_{MS}). This panel shows the two filaments of the Magellanic Stream also to be bifurcated in velocity from $-40° < L_{\mathrm{MS}} < -20°$. One of the filaments is discernible all the way to $(L_{\mathrm{MS}}, V_{\mathrm{LSR}}) \approx (-5, +247$ km s$^{-1})$ where it connects to the LMC. The second filament can be followed only to $(L_{\mathrm{MS}}, V_{\mathrm{LSR}}) \approx (-16.5, +220$ km s$^{-1})$. More velocity bifurcations (or multiple splits) are evident at more negative velocities. The two filaments show strong periodic patterns for $-40° < L_{\mathrm{MS}} < -5°$, after which they follow a fairly linear negative velocity gradient ($-95 < L_{\mathrm{MS}} < -40°$). ($c$) Integrated intensity of H I Gaussians in V_{LSR} vs. B_{MS} (colorscale in units of K km s^{-1}). The bifurcation of the MS is discernible as well as some spiraling patterns of the filaments.

Stream was only known to be *spatially* bifurcated and since the Magellanic Bridge gas overlaps the MS filaments near the Clouds it was not possible to distinguish or separate the filaments for $L_{\mathrm{MS}} > -20°$. The *velocity* bifurcation at the head of the Stream allows us to trace the filaments back further to their source than previously possible. One striking characteristic of the filaments is their oscillating pattern (Fig. 2.9b and 2.10), which is discussed further in §2.5.5.

Figure 2.10a is a close-up view of Figure 2.9b and gives a clearer picture of the two filaments (traced with red and green lines in the lower-left inset). The filaments cross near $L_{\mathrm{MS}} \approx -28°$, but a narrower B_{MS} range $(-8.0° < B_{\mathrm{MS}} < -1.0°)$ shows the continuity of the "green" filament at this point (Fig. 2.10b) and allows us to track the filament across this longitude. Near $L_{\mathrm{MS}} \approx -16°$ the "red" filament crosses the SMC/Bridge gas. Another B_{MS} range $(-4.5° < B_{\mathrm{MS}} < 2.0°)$ reveals the continuity of the "red" filament through this region (Fig. 2.10c). Beyond this point the "red" filament connects to the LMC (hereafter the "red" filament will be called the "LMC" filament and the "green" filament the "second" filament). Putman et al. (1998) pointed out an "emission filament" emanating from the LMC (seen in the sky channel maps), but claimed it went into the Bridge; McGee & Newton (1986) earlier also saw possible indications of an LMC filament. However, the P–V representation of Figure 2.10 may be the first conclusive evidence that any part of the MS comes from the LMC. P03 claimed that the two MS filaments came from the SMC and Bridge, and most subsequent tidal simulations (Connors et al. 2006, and references therein) have adopted these origins as their starting point (e.g., by modeling the SMC as an N-body and the LMC as a rigid potential). We argue here that the assumptions that are the foundation of these simulations need to be reconsidered.

In order to track the LMC filament back to the location of its origin in the LMC,
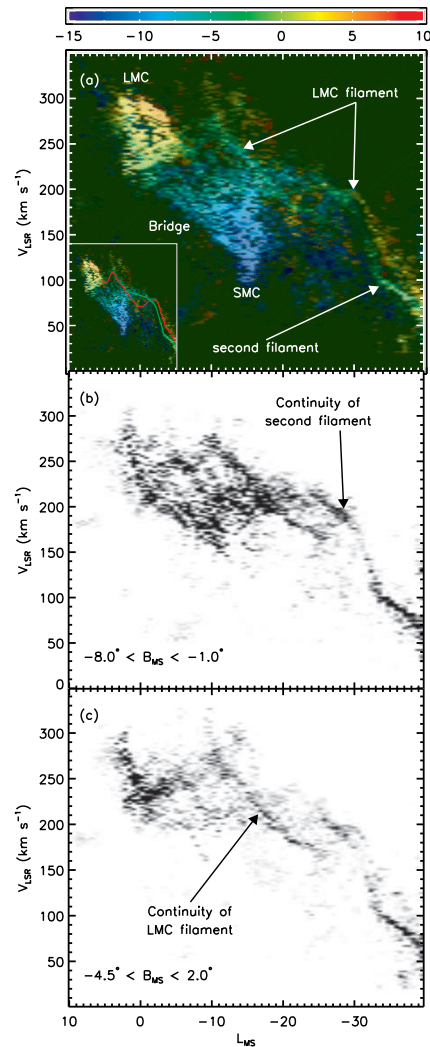
Fig. 2.10.— (*a*) Close up of the V_{LSR} vs. L_{MS} distribution of Magellanic Clouds and Stream H I Gaussians from Figure 2.9b (hue indicates B_{MS}, and brightness indicates integrated intensity along B_{MS}). The bifurcation of the two Magellanic Stream filaments is clearly discernable as are strong periodic patterns in the radial velocities of the filaments. The inset illustrates the shape of the two filaments (red – LMC filament, green – second filament). (*b*) A narrower range in B_{MS} to show that the second filament is continuous at the point (near $L_{\mathrm{MS}} \approx -28°$) where the two filaments cross in this projection (on a linear scale from 0–100 K km s^{-1} [white to black]). (*c*) A slightly different range in B_{MS} to indicate that the LMC filament is continuous as it crosses the SMC/Bridge gas near $L_{\mathrm{MS}} \approx -16°$ (on a linear scale from 0–200 K km s^{-1} [white to black])

we isolated the filament in the V_{LSR} vs. L_{MS} plot by eye with the dashed lines shown in Figure 2.11a. Figure 2.11b shows the distribution of the LMC filament on the sky. The filament appears to have a spatially periodic pattern. The filament emanates from a region of dense HI on the southeastern, or leading, edge of the LMC, namely the SEHO (throughout this paper we will use the term SE HI overdensity to mean the entire region of high–density HI in the southeast of the LMC, $05^{\mathrm{h}}34^{\mathrm{m}}< \alpha < 05^{\mathrm{h}}52^{\mathrm{m}}$, $-68°28'< \delta < -71°53'$). The connection to the LMC can be even more clearly seen by overlaying the high spatial resolution HI data of the LMC from Staveley-Smith et al. (2003; hereafter S03) on our map (Fig. 2.12b). The LMC filament is clearly arm "B" seen by S03.

The SEHO is a natural place for an HI stream to originate, due to the high-density of HI there (the highest concentration of HI in the LMC). Furthermore, the SEHO is near the end of the LMC bar, is rich in CO (Yamaguchi et al. 2001), Hα emission (Kim et al. 1999), giant molecular clouds (Yamaguchi et al. 2001), and young star clusters (Bica et al. 1999). There are also several supergiant shells (Kim et al. 1999) and two CO filaments (Yamaguchi et al. 2001) in this region. Their relation to the MS is further explored in §2.6.

The origin of the second filament is not as well defined. In our maps (Figs. 2.9 and 2.10) the second filament can only be clearly traced to higher longitude as far as the Magellanic Bridge (near $L_{\mathrm{MS}} \approx -15°$, $V_{\mathrm{LSR}} \approx +200$ km s^{-1}). It is not clear whether the second filament eventually connects to the SMC, to the Bridge, or to the LMC. We used a by-eye selection in the V_{LSR} vs. L_{MS} plot (similar to the one used for the LMC filament above) to extract the second filament gas from the database of Gaussians (the dashed lines in Fig. 2.11c); its distribution on the sky is shown in Fig. 2.11d.
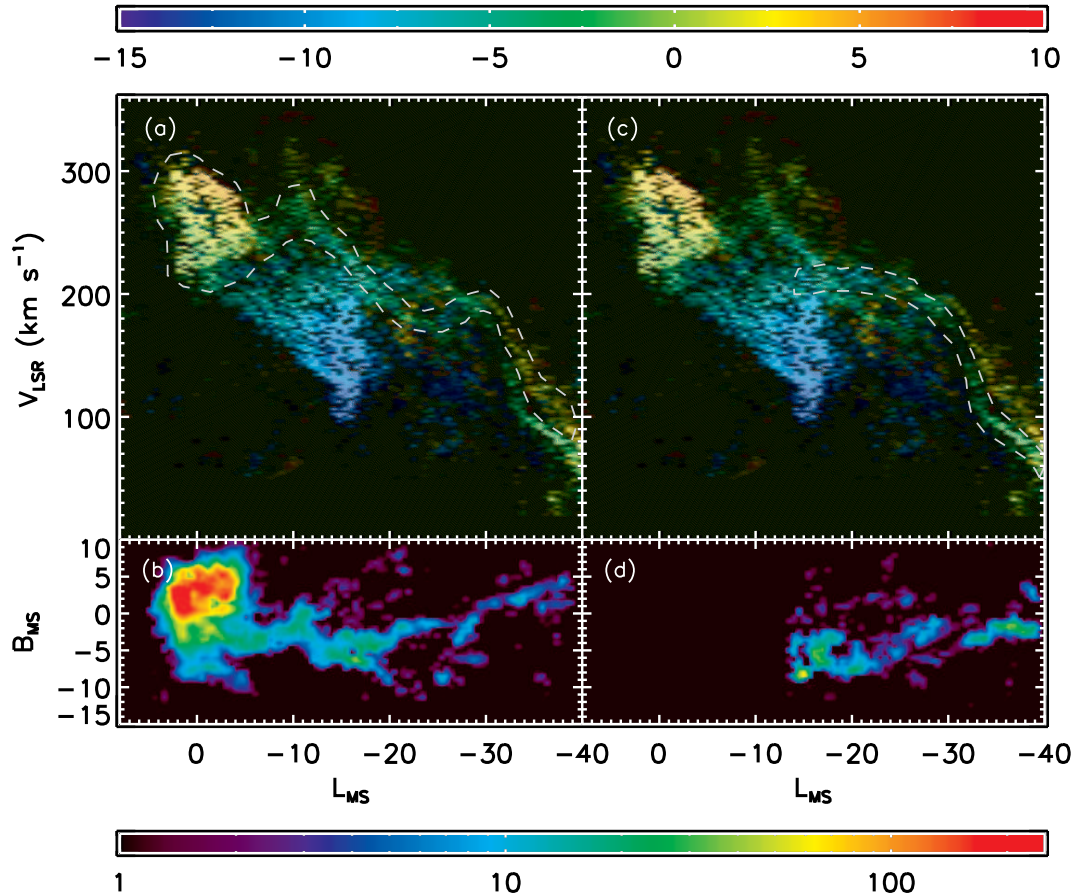
Fig. 2.11.— The two Magellanic Stream filaments isolated by velocity. **The LMC filament:** (a) $V_{\rm LSR}$ vs $L_{\rm MS}$ distribution for the Magellanic Cloud and Stream H I Gaussians showing two Magellanic Stream filaments (same as Fig. 2.9b). The gray dashed lines show the velocity limits used to isolate the LMC filament. (b) Sky distribution of the column density, $N_{\rm HI}$, of the H I Gaussians for the LMC filament selected by the velocity limits shown in panel (a). The association of the LMC filament with the LMC and the spatial periodic patterns are apparent. **The second filament:** (c) $V_{\rm LSR}$ vs. $L_{\rm MS}$ for the Magellanic Cloud and Stream H I Gaussians showing the two filaments (same as Figure 2.9b). The gray dashed lines show the velocity limits used to isolate the second filament. (d) As in panel (b), but for the second filament selected by the velocity limits shown in panel (c). The second filament can only be distinguished for $V_{\rm LSR} < -17°$ and its source remains unclear. The top color bar indicates $B_{\rm MS}$ for panels (a) and (c), while the bottom color bar indicates column density, $N_{\rm HI}$ (in units of 10^{19} atoms cm^{-2}), for panels (b) and (d).
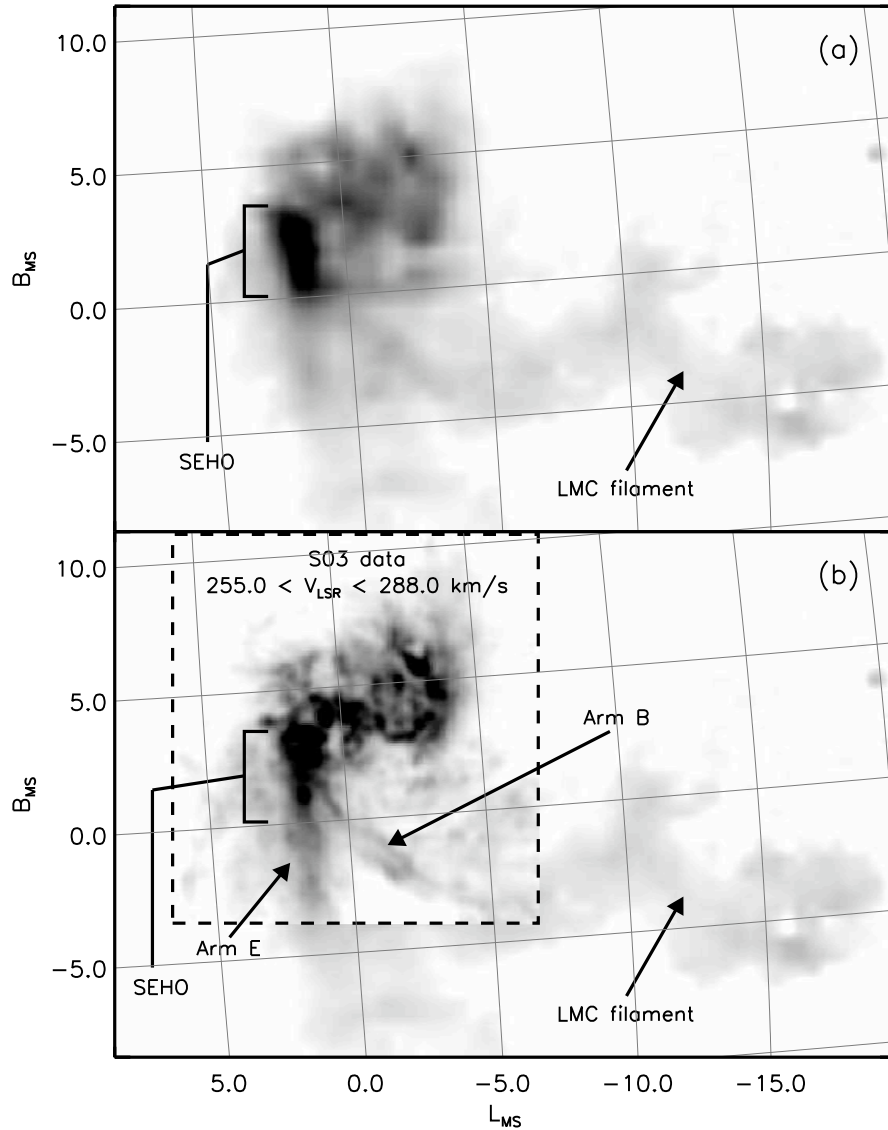
Fig. 2.12.— Close-up of the Fig. 2.11b map of the integrated intensity (sum of Gaussian areas) of the LMC and LMC filament HI Gaussians on the sky after a velocity filter (see Fig. 2.11a) is applied. These maps show that the LMC filament is emanating from the SEHO in the LMC when viewed with either (*a*) the LAB data only, or (*b*) the high-resolution HI data ($255.0 < V_{\mathrm{LSR}} < 288.0$ km s^{-1}) from S03 are substituted in the region outlined by the dashed lined box. The filament can be associated with S03 arm B. A square root transfer function is used in these greyscale images.
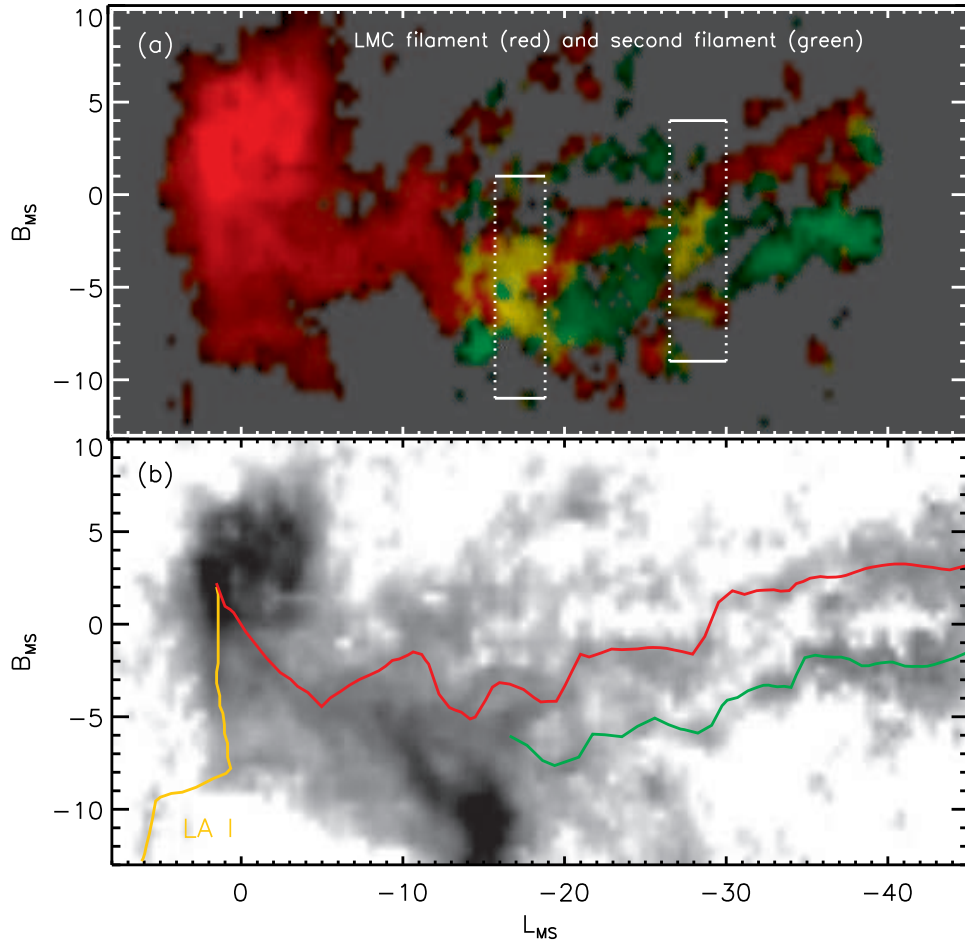
Fig. 2.13.— (*a*) The sky distribution of the two Magellanic Stream filaments as we have extracted them with velocity filters shown in Figure 2.11a,c (using a logarithmic transfer function for the intensity). The LMC filament is shown in red and the second filament in green. Most of the LMC is included in the velocity filter of the LMC filament. The two velocity filters (and the filaments) overlap in V_{LSR} and L_{MS} near $L_{\mathrm{MS}} \sim -17°$ and $L_{\mathrm{MS}} \sim -28°$ (as indicated by the dotted lines). Therefore, in these regions the separation of the filaments using the velocity selection *alone* is not as good. However, in these regions the filaments are spatially well-separated (the continuity of the two filaments in these overlap regions can also be seen in Figs. 2.10b and c). (*b*) Column density, N_{HI}, of the HI Gaussians (on a logarithmic scale from 1–200×10^{19} atoms cm^{-2} [white to black]). The "guiding" centers of the LMC filament (red), the second filament (green), and LA I (orange, discussed in §2.5.4) are overplotted in order to indicate their positions relative to more familiar structures (e.g., SMC, Bridge, etc.).

Figure 2.13a compares the positions of the two filaments on the sky (after the velocity selections in Fig. 2.11a and c have been applied). The filaments can be more easily distinguished in this representation because the Bridge gas has been removed. The two velocity filters (and the filaments themselves) overlap in V_{LSR} and L_{MS} near $L_{\mathrm{MS}} \sim -17°$ and $L_{\mathrm{MS}} \sim -28°$ (as indicated by the dotted lines). Therefore, in these regions the separation of the filaments using the velocity selection *alone* is not as good, but, fortunately, the filaments are spatially well-separated in these regions. The continuity of the two filaments in these overlap regions can also be seen in Figure 2.10b and c. The patterns of the two filaments on the sky are similar (also see Fig. 2.8b), shifted by $\sim 5°$ in L_{MS} and $\sim 1°$ in B_{MS}. Possible physical explanations for these patterns are discussed in §2.5.5. Figure 2.13b shows the H I column density on the sky of the Magellanic Gaussians with the "guiding" centers of the LMC filament (red), the second filament (green), and the connection of LA I to the SEHO (orange, discussed in §2.5.4) overplotted in order to indicate their positions relative to more familiar structures (e.g., SMC, Bridge, etc.).

2.5.4 The Source of the Leading Arm Feature (LAF)

The LAF consists of three complexes of gas north of the MCs. Pieces of these structures were first seen by van Kuilenburg (1972) and Wannier et al. (1972). Although there was no direct connection, Mathewson et al. (1974) suggested a possible association of these features to the MCs and this hypothesis was further explored by Mathewson et al. (1979), Morras (1982), and Bajaja et al. (1989). With reprocessed HIPASS data Putman et al. (1998) demonstrated that the LAF gas is indeed associated with the Magellanic Clouds and is an extension of the Magellanic Stream. The association of the LAF with the Magellanic Clouds and the MS lent support to the

tidal origin of the MS over the ram-pressure model, because a leading feature of the MS would *not* be expected if ram-pressure were the dominant force.

The three primary complexes of the LAF can be seen in Figure 2.8 at positive L_{MS}: LA I: ($3° < L_{\mathrm{MS}} < 29°$, $-34° < B_{\mathrm{MS}} < -6°$); LA II: ($36° < L_{\mathrm{MS}} < 61°$, $-17° < B_{\mathrm{MS}} < -10°$); and LA III: ($35° < L_{\mathrm{MS}} < 62°$, $-2° < B_{\mathrm{MS}} < 11°$) (nomenclature by B05). Our analysis here focuses on LA I, the closest LAF complex to the Magellanic Clouds. LA I consists of three nearly rectangular $\sim 2.5° \times 8°$ concentrations of gas that each lie almost parallel to lines of constant L_{MS}, and, combined, form a linear structure making an $\sim 40°$ angle with the $B_{\mathrm{MS}}=0°$ line (Fig. 2.8). Putman et al. (1998) showed that the two concentrations nearest the LMC are nearly continuous (see their Fig. 3) and it is therefore likely that the entire LA I feature is a physically connected structure. The first concentration of LA I is close to the south–eastern edge of the LMC, both in position and in radial velocity. Putman et al. (1998) claim, however, that the Leading Arm material comes mainly from the SMC, based on a filamentary feature that is nearly parallel with the $B_{\mathrm{MS}}=0°$ line and that begins near the SMC and stretches to the first concentration of LA I (see their Fig. 1). However, S03 noted several HI features of the LMC (arms B, E, S, and W) and remarked that arm E pointed to the Leading Arm clouds, which lay beyond the coverage of their survey. S03 go on to say that deep, reprocessed HIPASS data (P03) shows a continuous connection between arm E and the Leading Arm. Nevertheless, S03 conclude that the Leading Arm gas mainly arises from the SMC, and only some LMC gas "leaks" into the Leading Arm. B05 showed that the first concentration of LA I is directly connected in position and velocity to the HI clouds close to the LMC, but claim that it is associated with the Bridge. We believe that there is a much firmer association of the Leading Arm with the LMC.
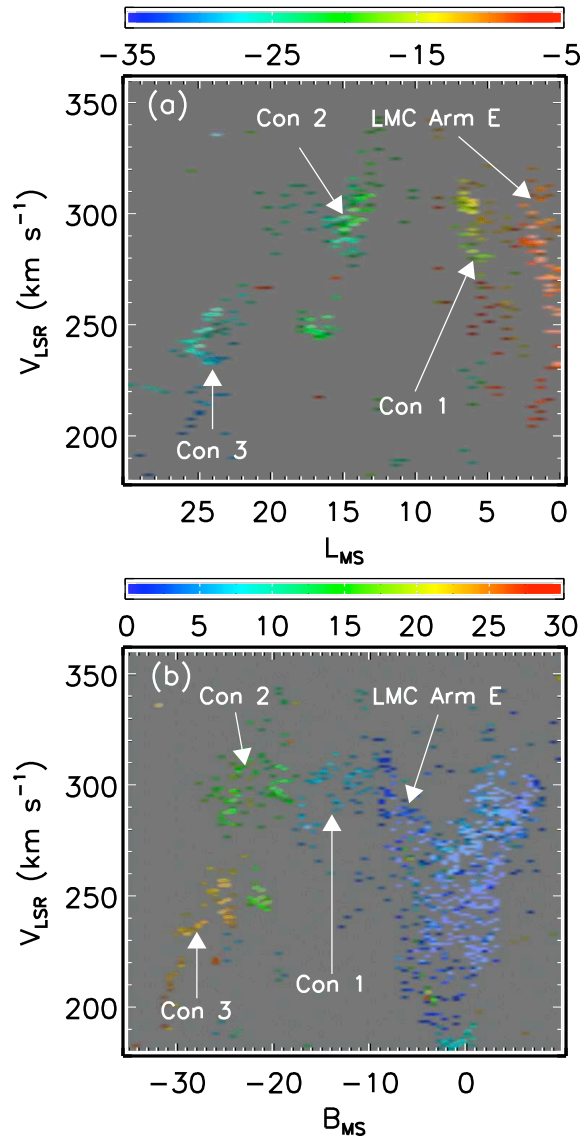
Fig. 2.14.— Integrated intensity distributions of the Leading Arm Feature (LA I) and some LMC H I Gaussians: (a) V_{LSR} vs. L_{MS} distribution (hue indicates $<B_{\mathrm{MS}}>$, brightness indicates integrated intensity along B_{MS}), and (b) V_{LSR} vs. B_{MS} (hue indicates $<L_{\mathrm{MS}}>$, and brightness indicates integrated intensity along L_{MS}). The three concentrations and the LMC arm E are labeled (also see Fig. 2.15). These two figures show that the first concentration of LA I ($-17° < B_{\mathrm{MS}} < -10°$) connects in position and radial velocity to an extension of the eastern part of the LMC ($-10° < B_{\mathrm{MS}} < -5°$), which is arm E of Staveley-Smith et al. (2003).

The radial velocities of the LA I complexes are quite similar to those of the LMC (Fig. 2.4b), but typically some $\sim$100 km s^{-1} higher than those of the SMC. This can be seen especially well in Figure 2.14b, where the first concentration of LA I ($-17° < B_{\mathrm{MS}} < -10°$) is connected in position and velocity to an extension of the LMC ($-10° < B_{\mathrm{MS}} < -5°$), namely S03's arm E. To better probe the association of LA I to the LMC we show the distribution of gas in the velocity range $250 < V_{\mathrm{LSR}} < 320$ km s^{-1} in Figure 2.15a. In Figure 2.15b we also overlay the S03 high resolution ATCA HI data over our own (using the same velocity cut) to confirm the basic geometry seen in the LAB data, namely S03's arm E extending out of the LMC and towards the first two concentrations of LA I (which are not covered by the S03 survey). Arm E has the same elongated shape (parallel to B_{MS}) and continues the spatial progression of the three LA concentrations (more negative B_{MS} towards higher L_{MS}). Arm E also continues the velocity trend with B_{MS} as seen in Figure 2.14b. There is a gap of a few degrees between the end of arm E and the beginning of the first concentration of LA I (although there is a small clump of gas between them at $[L_{\mathrm{MS}}, B_{\mathrm{MS}}] \approx [4°, -11°]$). However, our data also show gaps between the three concentrations of LA I that the deeper HIPASS data show are contiguous. Therefore, it is likely that arm E and the first concentration of LA I are also connected. For all of these reasons, we strongly suspect that LA I is physically connected to arm E (which starts in the SEHO) and has its origins in the LMC. Therefore, we conclude that both the trailing LMC filament of the MS and LA I have their origin in the SEHO of the LMC. We discuss the implications of these findings further in §2.6.

As previously mentioned, Putman et al. (1998) argue that the LAF comes from the SMC, based on a horizontal feature south of the LMC which seems to connect the SMC to the Leading Arm (see their Figs. 1 and 2). This feature is extended nearly
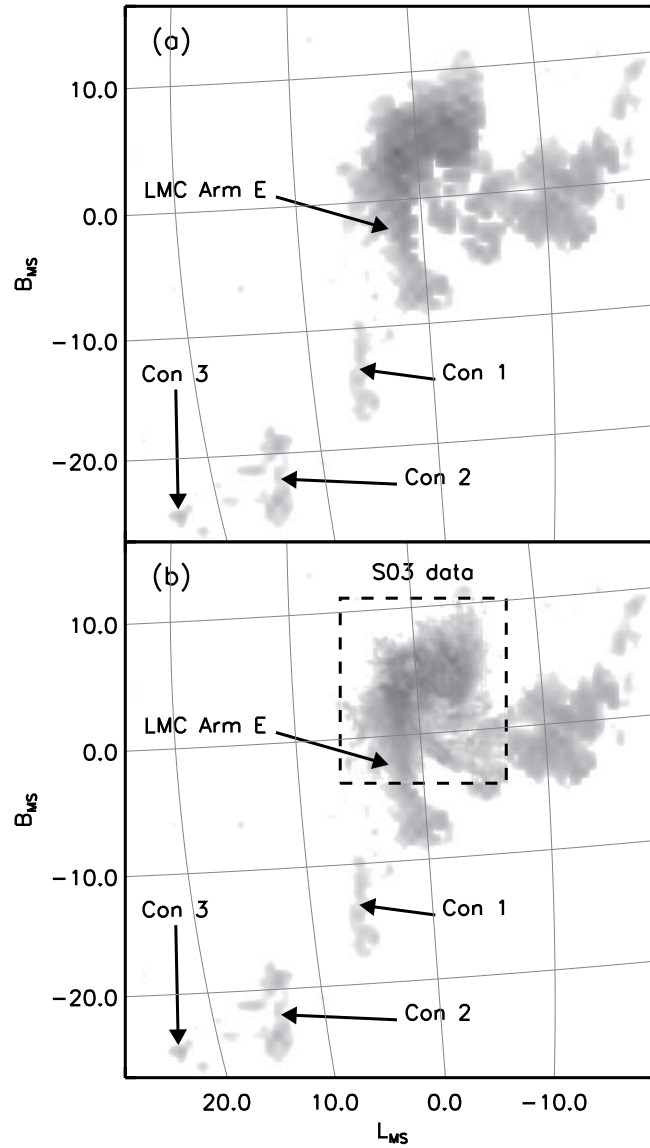
Fig. 2.15.— Maps of integrated intensity (sum of Gaussian areas) of the Leading Arm Feature (LA I) and the LMC H I Gaussians on the sky for gas with $250 < V_{\mathrm{LSR}} < 320$ km s^{-1} (on a logarithmic scale): (*a*) LAB data only; (*b*) LAB data augmented with the high-resolution H I data from Staveley-Smith et al. (2003) in the dashed lined box. The three concentrations of LA I and the LMC arm E are marked. These maps show that the first concentration of LA I is close to the southern end of LMC arm E. Arm E (which originates in the SEHO) is similar in shape to the three concentrations of LA I and continues the spatial progression. This indicates that LA I originates in the SEHO of the LMC.

parallel to the $B_{MS}=0°$ line and the first of these features is also visible in our maps (see Fig. 2.9a; $-10° < L_{MS} < 1°$ and $-8° < B_{MS} < -7°$) and does connect to the end of arm E in position as well as in velocity. It is this apparent connection, as well as the presence of the other "horizontal" cloud between the first feature and the SMC, that is the basis for Putman et al.'s claim that the LAF originates in the SMC. We cannot definitively refute this hypothesis but believe that the geometry of the gas in LA I and arm E is more suggestive of the LMC as the originator of the LAF: whereas arm E is already oriented in the same direction as the LA I concentrations and continues their staggered vertical striping spatial pattern (Figs. 2.8 and 2.15), the Putman et al. horizontal features are oriented orthogonally.

If this gas is moving towards the LMC, then it might be possible that the SMC is contributing some gas to the Leading Arm or creating its own leading arm. On the other hand, if the horizontal feature is moving from the LMC to the direction of the SMC, then it may be originating from the end of arm E and is part of the trailing MS. The structures and patterns of the horizontal features look much like the filaments of the MS, and, when extrapolated, the horizontal features seem to connect to the second MS filament (Fig. 2.9a). If this is the case, then the entire Magellanic Stream and the Leading Arm might originate from LMC gas; more work is needed to clarify this part of the Magellanic Bridge. Based on the evidence that we have presented in this section (summarized in Figs. 2.14 and 2.15), however, we conclude that most (if not all) of the Leading Arm gas originates in the SEHO of the LMC.

2.5.5   The Cause of the Periodic Pattern

As pointed out in §2.5.3, the two filaments of the MS have pronounced sinusoidal patterns in velocity and in position, especially for $L_{MS} > -40°$ (Fig. 2.9). P03

noted that the two filaments give the impression of a double helix and postulated that it might be due to the "pseudobinary motion of the LMC and SMC". This tumbling motion thus provides a first hypothesis as to the cause of these patterns. However, there are several problems with this hypothesis. The path of two bodies orbiting each other would create a double-helix pattern in our position–position–velocity (ppv) datacube and in the projections of the datacube. That is not seen for the two filaments at the head of the stream ($L_{MS} > -40°$), although they might cross farther downstream. Figure 2.16 shows the paths of the central concentrations of the two filaments, in the three projections (B_{MS} vs. L_{MS}, V_{LSR} vs. L_{MS}, and V_{LSR} vs. B_{MS}), and reveals that the two filaments do not cross or spiral around each other (at least in this L_{MS} range), but rather create two independent spirals parallel to each other. Therefore, the spiraling motion that we see cannot be explained by the tumbling of the LMC and SMC about each other (if they are indeed bound to one another). It is also not clear where the second filament originates, whereas its origin *must* lie in the SMC if the tumbling hypothesis is to work. The two filaments do eventually cross each other at $L_{MS} \sim -47°$ (Fig. 2.9a) and other places, beyond the large velocity oscillations seen at the head of the MS ($-40° < L_{MS} < -5°$). The spatial crossing of MS strands we see at $L_{MS} \sim -47°$ has become apparent in our maps because the zero-velocity gas has been removed; this MS crossing is also apparent in Figure 2 of B05, but was not noted by P03. It is possible that these "later", more widely separated from the MCs, crossings could be due to the binary motion of the Magellanic Clouds (if the second filament actually originates in the SMC), but the spirals at the head of the Stream cannot. There must be another explanation for these spiraling patterns close to the MCs.

We postulate instead that the spiraling motion is an imprint of the rotation curve
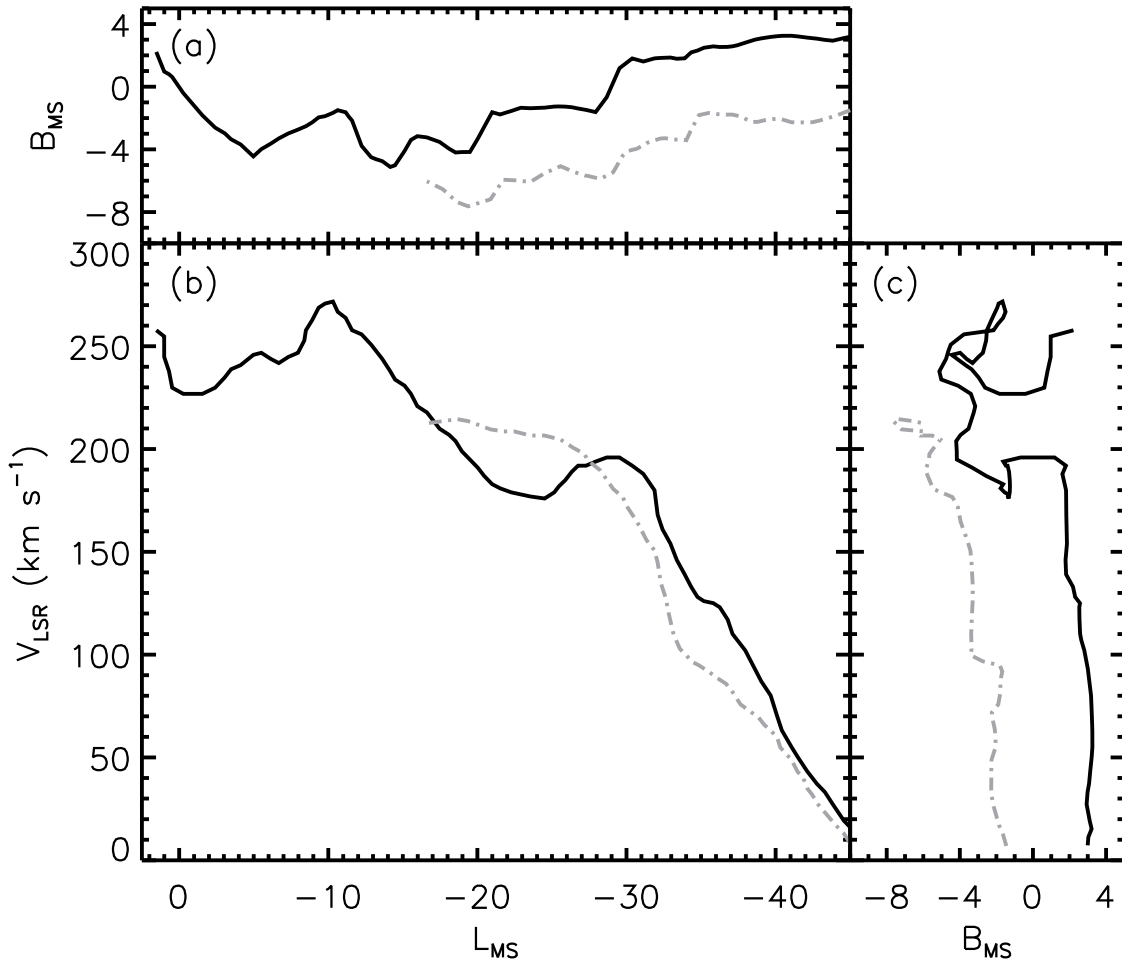
Fig. 2.16.— This figure is analogous to Figure 2.9. The path of the central concentrations of the two MS filaments from three perspectives: (*a*) B_{MS} vs. L_{MS}, (*b*) V_{LSR} vs. L_{MS}, and (*c*) V_{LSR} vs. L_{MS}. The LMC filament (solid) and the second filament (grey, dash–dotted) do not wrap around each other, but move parallel to one another, in this L_{MS} range.

of the LMC (and possibly the SMC). This scenario fits the data better than the previous hypothesis, especially for the LMC filament where the sinusoidal variation is pronounced and the filament can be reliably traced back to its origin in the LMC, which has a well-defined disk (e.g., Weinberg & Nikolaev 2001; van der Marel 2001) and rotation curve (e.g., Kim et al. 1998; van der Marel et al. 2002). The amplitude

of the spatial variations is $\sim 2°$ (Fig. 2.11b) which is close to the radius of the SEHO from the LMC center. A sinusoid+line fit to the LMC filament in V_{LSR} vs. L_{MS} gives

$$V_{\mathrm{LSR}} = (26.4\,\mathrm{km\,s^{-1}})\sin\left(\frac{360°}{20.9°}L_{\mathrm{MS}} - 5.9°\right) + (4.40\,\mathrm{km\,s^{-1}\,deg^{-1})}\,L_{\mathrm{MS}} + 291.75\,\mathrm{km\,s^{-1}}$$

$$(2.2)$$

and can be seen in Figure 2.17. Assuming that the linear portion is due to the orbital motion of the LMC about the MW, the sinusoidal amplitude of $26.4\,\mathrm{km\,s^{-1}}$ is not that different from the projected LMC rotation velocity at the radius of the SEHO ($\sim 2.5°$ from the center of the LMC), i.e. $V_{\mathrm{rot}}\sin i \approx 39.4\,\mathrm{km\,s^{-1}}\sin 34.7° = 22.4\,\mathrm{km\,s^{-1}}$ (vdM02; Kallivayalil et al. 2006a). It therefore seems that the data are reasonably consistent with the hypothesis that the spiral pattern in the LMC filament was created by the rotation of the SEHO (the filament's apparent birthplace) about the center of the LMC as the entire system orbited the MW. Our hypothesis is that some force — tidal, ram pressure or otherwise — must have pulled/pushed the HI gas out of the SEHO (see §2.6) and the trailing gas bears the imprint of the SEHO's particular velocity and position.

Assuming this hypothesis is true, we can estimate the drift rate of the HI gas in the LMC filament by using the angular period of the sinusoidal pattern. The orbital period of the SEHO around the LMC is $T = (2\pi \times 2.5° \times 0.875\,\mathrm{kpc\,deg^{-1}})/39.4\,\mathrm{km\,s^{-1}} \approx 340$ Myr. In this time the SEHO's radial velocity undergoes one full cycle, which we can identify with one full cycle of the LMC filament's velocity pattern. Even though we have a spatial period from the sinusoidal fit, it is apparent from Figure 2.17 that the sinusoid+line deviates slightly from the periodic pattern. We can get a more accurate estimate of the spatial period by looking at the maxima at $(L_{\mathrm{MS}}, V_{\mathrm{LSR}}) = (-10.3°,\ 271.4\,\mathrm{km\,s^{-1}})$ and at $(L_{\mathrm{MS}}, V_{\mathrm{LSR}}) = (-29.8°,\ 194.6\,\mathrm{km\,s^{-1}})$, which gives
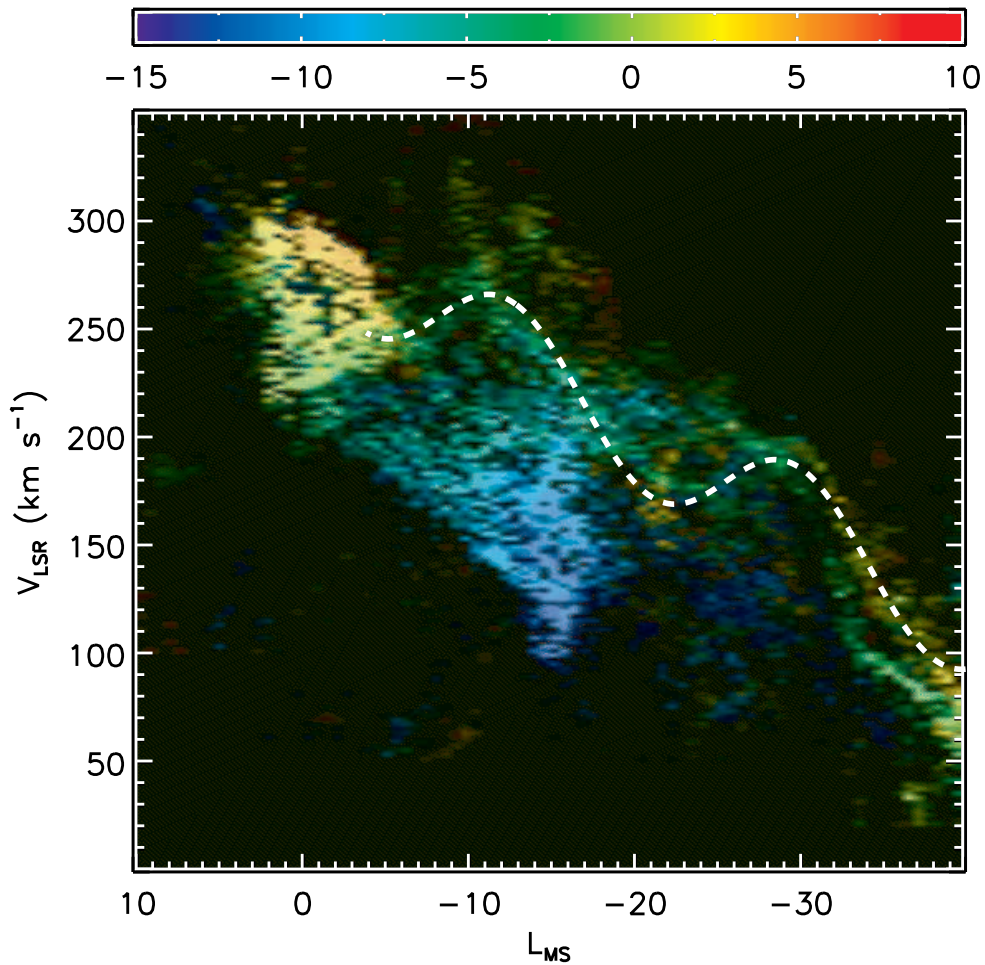
Fig. 2.17.— V_{LSR} vs. L_{MS} of the Magellanic Stream Gaussians (same as Fig. 2.10) with the sine+linear fit (Equation 2) to the LMC filament.

19.5° for the spatial period. The LMC filament gas is probably still close to the LMC distance from the Sun of ∼50 kpc which we can use to calculate the distance between the maxima as $D = 19.5° \times 0.875$ kpc deg^{-1} = 17.06 kpc. If the time difference between when these two points of gas were in the SEHO is just 340 Myr, the orbital period of the SEHO, and if the drift rate of the LMC filament gas away from the LMC is also roughly constant, then we can estimate it as $V_{\mathrm{drift}} = 17.06$ kpc/340 Myr

$= 49.1$ km s^{-1}. This is a lower limit since it does not include any radial component of motion. The drift velocity is $\sim 1/9$ the tangential velocity of the LMC, $v_{\mathrm{LMC,tan}} = 367$ km s^{-1} (Kallivayalil et al. 2006a).

Lastly, we can use the drift rate of the LMC filament gas to roughly estimate the age of the Magellanic Stream. If we assume that the drift rate has been approximately constant for the entire MS as well as an average distance of 50 kpc to the Stream, then the age of the Stream is $(100° \times 0.875$ kpc deg$^{-1})$ / 49.1 km s$^{-1} = 1.74$ Gyr. A more direct way of calculating this would be to count the number of oscillations along the MS and multiply by 340 Myr (the orbital period at the SEHO radius). However, the amplitude of the modulations decreases quite dramatically after about $\sim 40°$ from the LMC and the two filaments are not as well separated in velocity so it is not yet possible to do this in practice. If the distance to the tip of the MS is larger than 50 kpc (as predicted by the models of Connors et al. 2006, see their Fig. 6), then the MS would be older, and conversely, the MS would be younger if the MS tip is closer than 50 kpc (as suggested by the ram pressure models of Mastropietro et al. 2005, see their Fig. 7). A changing drift rate would also affect the MS age. Even so, an MS age of ~ 1.7 Gyr is fairly close to the 1.5 Gyr age of the Stream found by Murai & Fujimoto (1980) at which time their tidal simulations show an SMC-LMC-MW close encounter. However, the orbit calculations using the new HST proper motions (Kallivayalil et al. 2006a,b; Piatek et al. 2008) and an NFW MW potential by Besla et al. (2007) give past MC encounters at roughly 0.2, 3 and 6 Gyr ago (G. Belsa, private communication). These numbers are highly dependent on the mass ratio of the MCs ($\sim 1:10$) and the SMC's proper motion both of which are quite uncertain. A close encounter at ~ 2–2.5 Gyr would be consistent with the bursts in the star formation rate seen in the star formation histories of *both* MCs (Smecker-Hane et

al. 2002; Harris & Zaritsky 2004). Therefore, an age of $\sim$1.7 Gyr for the MS seems reasonable considering the uncertainties.

Even though the rotation hypothesis seems self-consistent there is one possible problem – the coherence of the sinusoidal pattern in the filaments. If the rotation hypothesis is correct then there should also be an oscillating pattern in the transverse velocity of the filaments. One would expect that the variation in velocities would pull apart or stretch the filament. At the very least the different velocities should place the gas in different MW orbits because of their differing energies, which would also destroy the coherence of the filament. Since this is not seen, and the structure is coherent over at least $\sim$40°, there must be something else holding the structure together. Konz et al. (2002) show how the interaction of a cold cloud with its surrounding ambient medium can create a magnetic barrier which helps keep the cloud intact. In addition to explaining the survival times of the MS filaments, the interaction of the clouds with their surrounding medium might help explain the coherence of the Stream over such large distances. More detailed N-body/hydrodynamic (and magneto-hydrodynamic) simulations are needed to investigate how the MS filaments, with their oscillating velocity patterns, can remain coherent over such distances.

For $L_{\mathrm{MS}} < -40°$ the sinsusoidal pattern diminishes substantially, and the amplitude of any leftover variations is much smaller (Fig. 2.9) and the behavior of the MS is more nearly linear ($V_{\mathrm{LSR}} \approx 7.60\ L_{\mathrm{MS}} +370$ km s^{-1}; for $L_{\mathrm{MS}} < -40°$). Something dramatic must happen at $L_{\mathrm{MS}} \sim -40°$ to cause this change. One possible explanation is that this is where drag from the MW halo gas becomes important, dampens the sinusoidal pattern, and causes the MS to follow a quite linear curve. Another possibility is that the LMC is actually much larger than previously thought (exceeding even the newly suggested limit in Muñoz et al. 2006) and the MS gas is escaping the

tidal radius of the LMC at $L_{\mathrm{MS}} \approx -40°$.

If the LMC tidal radius is 40 kpc then from equation (45) in vdM02 (and a MW mass interior to the LMC of 4.9×10^{11} M$_\odot$) this would imply a minimum LMC mass of 1.68×10^{11} M$_\odot$ (or 34% of $M_{\mathrm{MW}}(< 50 \mathrm{\ kpc})$). The total intrinsic visible luminosity of the LMC is $L_V = 3.0 \times 10^9 L_\odot$ (vdM02) which implies a mass-to-light ratio of $M/L_V = 56$. This would mean that the LMC is very dark matter dominated.

If we assume that ram pressure is the dominant force causing the MS to drift back behind the LMC then, with some other assumptions, we can estimate the density of the hot MW halo gas. The ram pressure on the MS is $P = \rho_{\mathrm{MW}} v_{\mathrm{MS}}^2$. If L_{MS} is the approximate diameter of the MS, then the acceleration that the MS experiences is $a_{\mathrm{MS}} \approx \rho_{\mathrm{MW}} v_{\mathrm{MS}}^2 L_{\mathrm{MS}}^2 / (\rho_{\mathrm{MS}} L_{\mathrm{MS}}^3) \approx \rho_{\mathrm{MW}} v_{\mathrm{MS}}^2 / (\rho_{\mathrm{MS}} L_{\mathrm{MS}})$. Solving for the ratio of densities gives $\rho_{\mathrm{MW}}/\rho_{\mathrm{MS}} \approx a_{\mathrm{MS}} L_{\mathrm{MS}}/v_{\mathrm{MS}}^2$. If we assume that the MS was undergoing a constant deceleration due to ram pressure in the recent past then we can estimate this deceleration from the sinusoidal pattern in the LMC filament, $a_{\mathrm{MS}} \approx 2\Delta\mathrm{x}/\Delta\mathrm{t}^2 \approx 2 \times 17.06 \mathrm{\ kpc}/(340 \mathrm{\ Myr})^2 \approx 295.2 \mathrm{\ kpc/Gyr}^2$. Approximating the diameter of the LMC filament at the head of the Stream as $L_{\mathrm{MS}} \sim 2$ kpc and $v_{\mathrm{MS}} \approx v_{\mathrm{LMC}} = 378$ km/s (Kallivayalil et al. 2006a; Piatek et al. 2008) we obtain $\rho_{\mathrm{MW}}/\rho_{\mathrm{MS}} \approx 0.004$. The average column density of the LMC filament is $N_{\mathrm{HI}} \approx 1 \times 10^{20}$ atoms/cm^2. Assuming a distance of 50 kpc and a width of ~ 2 kpc gives a number density of $n_{\mathrm{MS}} \approx 0.016$ atoms/cm^2. Finally, we derive the number density of the hot MW halo as $n_{\mathrm{MW}} \approx 6.3 \times 10^{-5}$ atoms/cm^2. This rough estimate of the density of the hot MW halo gas is consistent with most previous estimates (e.g. Stanimirović et al. 2002; Sembach et al. 2003).

2.6 The Cause of the Outflow from the SE Hi Over-density

2.6.1 LMC High Velocity Gas Ejection

What is causing the Leading Arm and LMC filament gas to flow out of the SEHO? It is difficult to assess this question with the LAB data due to its relatively low spatial resolution ($0.5°$); however, the higher spatial and velocity resolution of the S03 Hi data of the LMC from the Parkes telescope is well suited to a closer look at the SEHO. In Figure 2.18 we show the integrated intensity of the LMC Hi from three different perspectives: (a) δ vs. α, (b) V_{LSR} vs. α, and (c) V_{LSR} vs. δ. The CO clouds identified with NANTEN by Mizuno et al. (2001) are plotted as white dots in these figures.

The high density of the SEHO is readily apparent in the column density plot (Fig. 2.18a), as are great voids in the gas, which are evidence of supergiant shells.[3] The Leading Arm can be seen stretching southward of the SEHO and the LMC filament diagonally to the southwest (S03's arms E and B, respectively). A position-velocity diagram of the LMC (Fig. 2.18b; integrated along δ, which is nearly parallel to the LMC Hi kinematical line-of-nodes,[4] Kim et al. 1998) shows that the LMC is not symmetrical in Hi but is lopsided and contorted. Furthermore, there is a large build-up of neutral gas on its leading/eastern edge (where the SEHO is located). It has been suggested by de Boer et al. (1998) that this is a result of the LMC interacting with the diffuse MW halo gas (see further discussion of this point in §2.7.3).

The velocity profile of the LMC in the third view (Fig. 2.18c), a position-velocity

---

[3]These supergiant shells are even more pronounced in the much higher spatial resolution ATCA data used by Kim et al. (1999) in their study of the supergiant shells (as well as in the combined ATCA+Parkes HI data by Kim et al. 2003).

[4]Here we adopt the definition (used by Luks & Rohlfs 1992 and Kim et al. 1998) of the line-of-nodes as the axis of maximum velocity gradient. This differs from the definition of the line-of-nodes by vdM02 as the intersection of the galaxy plane with the plane of the sky.
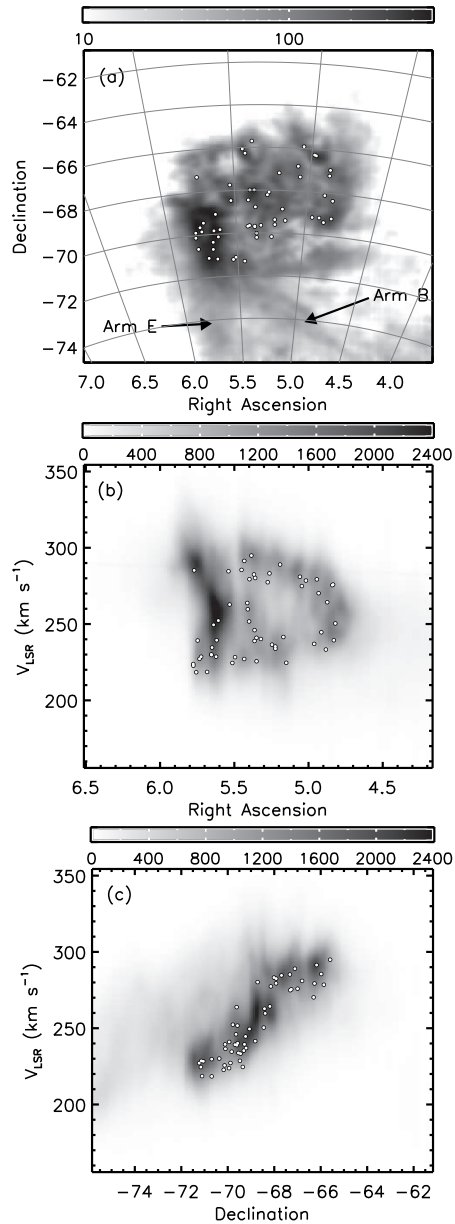
Fig. 2.18.— Integrated intensity of the LMC H I datacube (from S03) from three perspectives: (a) Column density, N_{HI}, in units of 10^{19} atoms cm^{-2}, (b) V_{LSR} vs. α (integrated in δ; greyscale in units of K), and (c) V_{LSR} vs. δ (integrated in α; greyscale in units of K). From (c) it is clear that there is gas coming off the LMC on the high-velocity end and moving to the south. The CO clouds from Mizuno et al. (2001) (white dots in all panels) are almost always associated with the LMC disk component (the regions with higher integrated intensity in panel (c)).
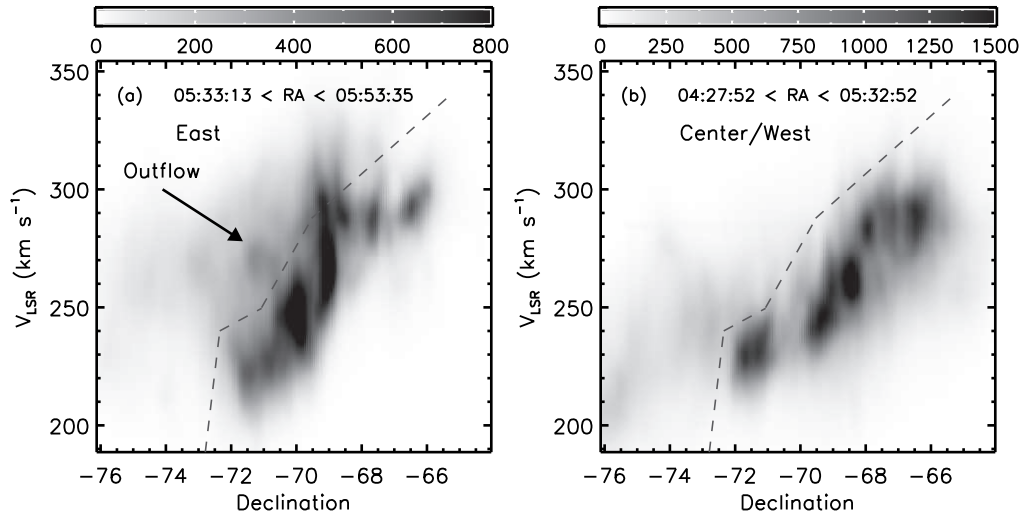
Fig. 2.19.— Integrated intensity of the eastern and central/western regions of the LMC from the S03 datacube. (*a*) The eastern region of the LMC showing the high and low velocity components (for $-72° < \delta < -69°$). (*b*) The central and western regions of the LMC showing a velocity distribution with less outflow. The high-velocity gas is coming mainly from the eastern part of the LMC. The grescales are in units of K. It is clear that the lower-velocity component in the south-east is the "disk" component by its high integrated intensity (compared to the high-velocity gas) and its similarity to the velocity distribution to the west. The velocity criterion used to separate the high-velocity gas from the LMC disk gas at each declination (see Fig. 2.20) is shown by the dashed line.

diagram integrated along α (i.e., nearly perpendicular to the Kim et al. line-of-nodes) appears, overall, to be much more symmetrical because it reflects very nearly the LMC rotation curve. However, one can see in Fig. 2.18c some gas at higher velocities than the LMC disk that has no corresponding, lower velocity counterpart. This gas appears to come off of the LMC disk (at the high-velocity side) and to stay at higher velocities than the disk. Both the high-velocity gas and the LMC disk gas follow a negative velocity trend with δ (i.e. lower velocities toward the south), but the high-velocity gas remains at higher velocities than the LMC disk at all positions.

In Fig. 2.19 we compare the eastern versus the central–western portions of the

LMC (where we have integrated along α). The first panel reveals the "high-velocity" gas clearly, with most of it coming from the south–eastern portion of the LMC, especially from $\alpha > 05^h30^m$ and $\delta < -70°$. We isolate the high-velocity gas by making a rough velocity selection (the dashed line in Fig. 2.19) in the V_{LSR} vs. δ plane, and show its sky distribution in Figure 2.20c. This high-velocity gas is indeed the Leading Arm and LMC filament (the same as S03's arm E and B), and it is clearly coming from the south-eastern region of the LMC, or the SEHO.

Another obvious feature in Figure 2.19a is a strong outflow of gas starting at $\delta \approx -70°$ and moving to higher velocities and southward; this feature might be coming from a supergiant shell (there are several in that region). The high spatial resolution HI data from Kim et al. (2003) show this region to have many thin outflows from the SEHO (see their Fig. 5, especially $05^h37^m < \alpha < 05^h48^m$) that are not resolved in the S03 data. As Kim et al. point out, these are probably outflows from several smaller giant shells (they identified 16 giant shells in this region). In their figures it appears that there are many small fountains of gas coming out of the SEHO which are contributing to the Leading Arm and trailing LMC filament. These outflows are explored in more depth in the next subsection.

Luks & Rohlfs (1992) found that the HI gas in the SEHO is disturbed and that there are two velocity components, which they called the high-velocity disk ("D") and low-velocity ("L") components. Figures 2.18–2.20 show, however, that the high-velocity component in the south-eastern LMC is not the LMC disk, but an out-flow that is the beginning of the Leading Arm and the trailing LMC filament. The low-velocity component has a much higher column density than the high-velocity component (Figs. 2.20a and c), and is contiguous with the rest of the LMC disk in position-velocity slices (Fig. 2.21). Also, the CO clouds in this region (Mizuno et
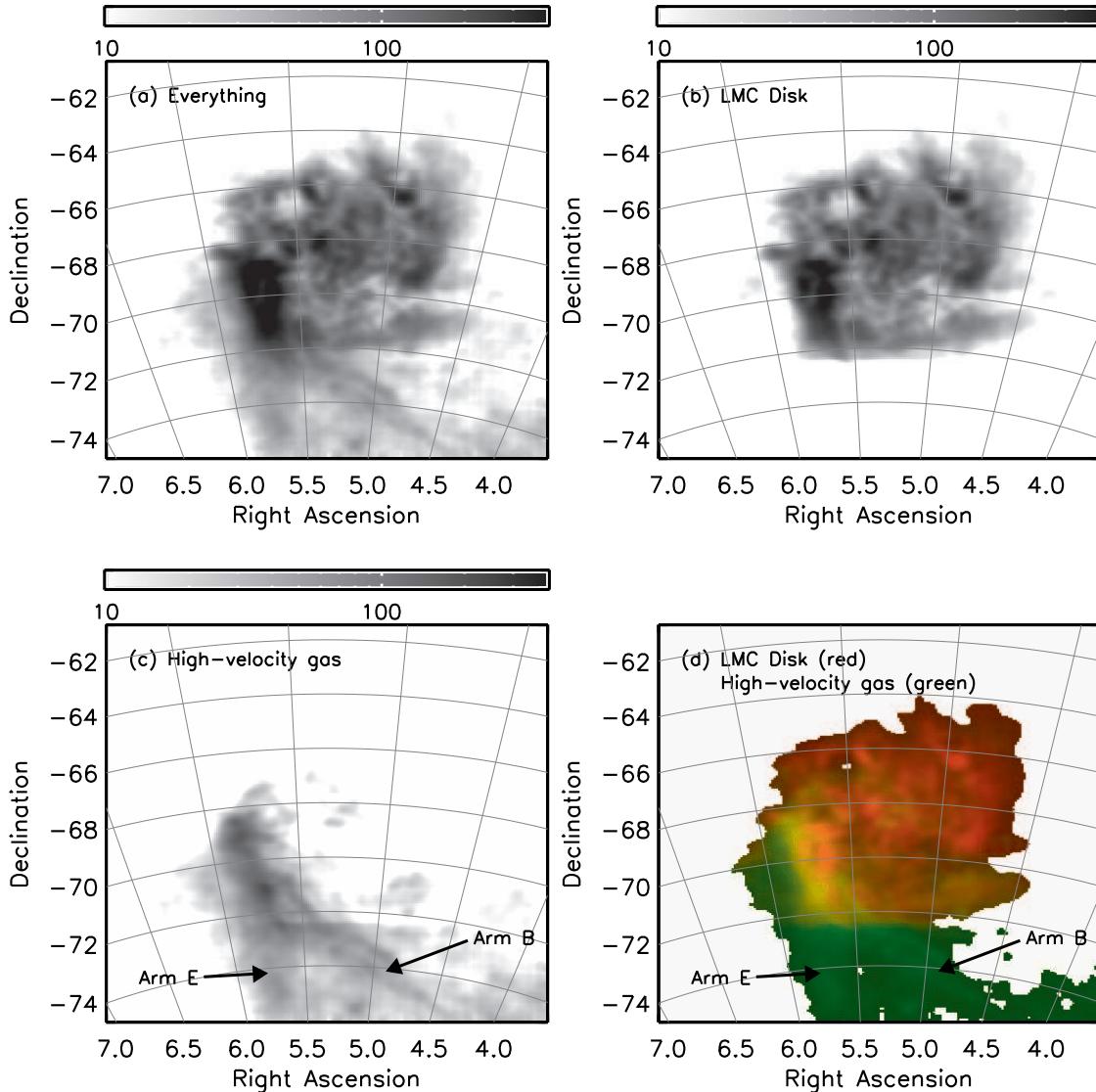
Fig. 2.20.— The sky distribution (column density, N_{HI}, in units of 10^{19} atoms cm^{-2}) of the different velocity components of the LMC: (*a*) All Magellanic-associated gas, (*b*) LMC disk gas only, and (*c*) high-velocity Magellanic gas only, using the velocity selection from Fig. 2.19. Arm E and B are part of the high-velocity component. (*d*) The distribution of both the LMC disk (red) and high-velocity (green) components of the LMC. Near the LMC disk the high-velocity gas is predominantly on the eastern/leading edge of the SEHO.

al. 2001) are *all* associated with the low-velocity compononent and none are associated with the high-velocity component (Figs. 2.18 and 2.21). Therefore, we conclude (contrary to Luks & Rholfs) that the *low-velocity* gas is the disk component (albeit a disturbed disk) in the south-eastern part of the LMC.

2.6.2 Source of the High-Velocity LMC Gas

What might the source be of this high velocity outflow? It has long been known that there are high-velocity gaseous flows emanating from star formation regions in the LMC, particularly in the form of supergiant shells (e.g., Meaburn & Blades 1980; Meaburn 1984; Meaburn et al. 1987); the most recent comprehensive study of these structures has been done by Kim et al. (1999). Several of these supergiant shells are also visible in the Parkes H I datacube and are, we believe, relevant to the origin of the MS. The $\alpha = 05^{\mathrm{h}}43^{\mathrm{m}}04^{\mathrm{s}}$ slice in Figure 2.21d shows a bubble feature with a void of gas in its center ($-70.5°< \delta < -69.0°$, 240 km s^{-1} $< V_{\mathrm{LSR}} <$ 280 km s^{-1}). This void of gas can also be seen in channel maps of the LMC (Fig. 2.22j–r; e.g., the U-shaped feature most obvious in Fig. 2.22n) and near the position of the supergiant shells SGS 19 and 20 (Kim et al. 1999). In fact, the void is probably SGS 19 and 20 and the bubble their combined envelope. There is a blob of gas that is "attached" near the edge of this bubble (Figs. 2.21d,e and Fig. 2.22e–g). The blob and this linking gas has a "tadpole"-like structure with the head farther south than the tail; together these features have an upside-down L shape and end near the position of the southern edge of SGS 20 (Figs. 2.21f,g). This seems to be evidence of an outflow from SGS 19 and 20. Figure 2.23 shows three perspectives of this outflow. SGS 1 also has an attached blob of gas that exhibits the same tadpole features (see Fig. 2.24c and §2.6.4). We conclude that both of these are outflows being expelled by the supernovae (SNe)
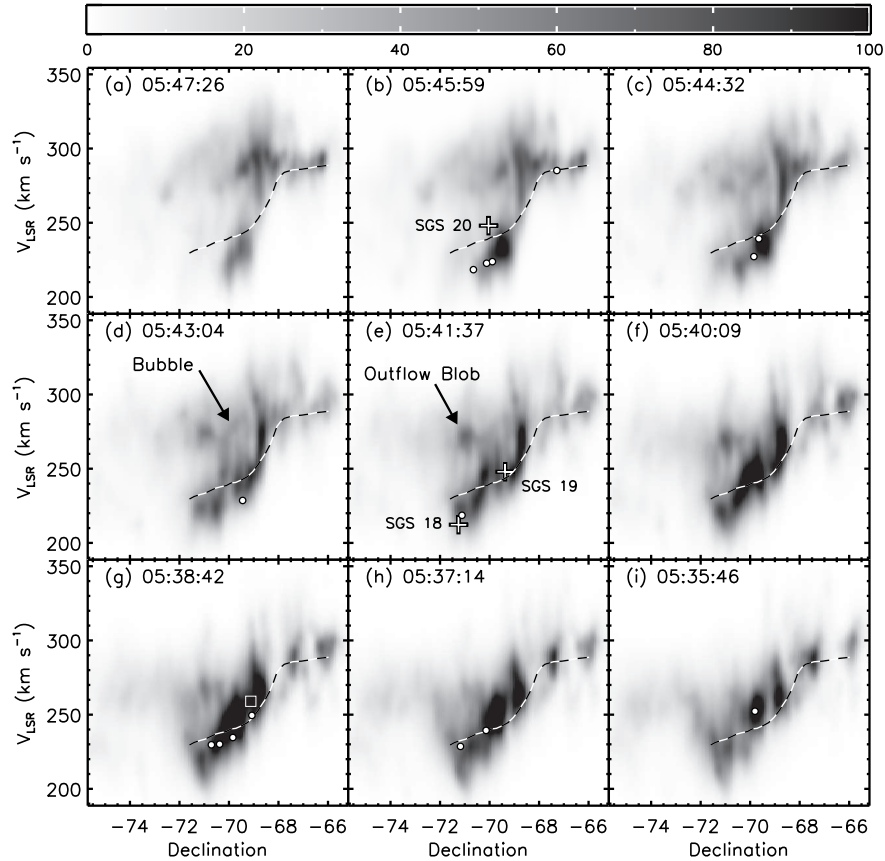
Fig. 2.21.— Position-velocity cuts in α of the eastern part of the S03 LMC H I datacube (going from east to west). Two α bins in the datacube were combined to create each panel. The central α is shown in the upper-left hand corner of each panel and the greyscale is in units of K. The dashed line shows the average rotation curve from the western part of the LMC, which helps separate the high-velocity gas from the disk component. White crosses indicate the central position and velocity of the three sugergiant shells from Kim et al. (1999) that are in this region (SGS 18, 19 and 20; the shells extend to the neighboring panels as well). This figure shows the large outflow of gas from this region to high velocity. A large bubble of gas, most clearly seen in panels (c)–(e), (centered at $\delta = -69°28'11''$, $V_{\rm LSR} = 265$ km s^{-1}) is near the position of SGS 19 and an outflow blob of gas, most apparent in (d)–(g), seems to be coming off the bubble. The CO clouds from Mizuno et al. (2001) (white filled dots) are clearly not associated with the high-velocity outflow gas but rather with the disk component. The central position and velocity of the 30 Doradus star cluster R136 is indicated by the white box in (g). R136 is a little bit west of where most of the high-velocity gas is being blown out.
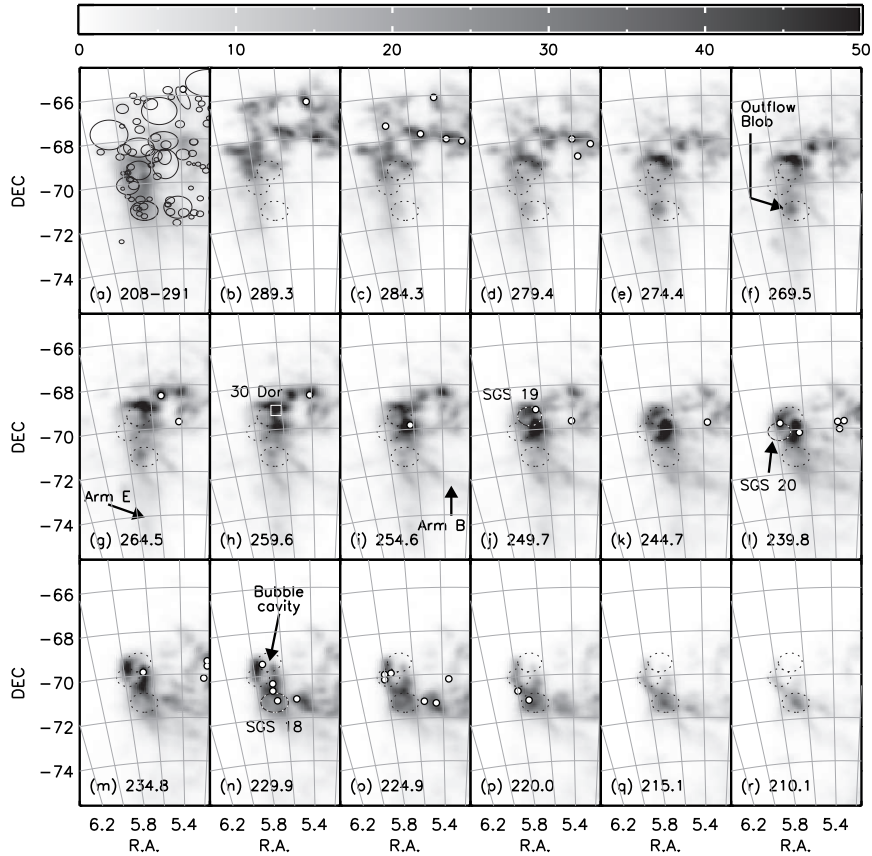
Fig. 2.22.— Channel maps of the eastern part of the S03 LMC H I datacube (from high to low velocity). Six velocity channels ($\sim$5 km s^{-1}) were combined to form each panel. The central V_{LSR} velocity (km s^{-1}) is shown in the lower-left hand corner of the panel. Panel (a) shows the column density (for 208–291 km s^{-1}) with the supergiant shells and giant shells from Kim et al. (1999) overplotted in black. The scale at the top indicates the column density, N_{HI}, for panels (b)–(r) in units of 10^{19} atoms cm^{-2}. White–black dashed lines indicate the three sugergiant shells SGS 18, 19 and 20 (at their central velocity, but they extend to many of the neighboring panels in velocity) from Kim et al. (1999). The outlines of these three supergiant shells are also shown as black dashed lines in panels (b)–(r) as reference positions. This figure shows the large outflow of gas from this region to high velocity including arms E and B. A large outflow blob of gas (also see Fig. 2.21), most clearly seen in panels (d)–(g), is near the position where SGS 18 and 20 intersect, but (Mizuno et al. 2001; white filled dots in all panels) are located in regions of dense H I and from which the outflows of gas originate (but at lower velocities than the outflows). The 30 Doradus star cluster R136 is indicated by the white box in h (at its central velocity).

and high stellar winds coming from the supergiant shells. A possible explanation for the tadpole-like structure is that once the outflow reaches a certain height above its origin site other forces, such as ram pressure and tidal forces, become dominant and push/pull the outflow southward (in the same direction that arms B and E are being pushed/pulled).

We propose the dynamical kick of SNe-driven SGSs as the mechanism that gave rise to the majority of the outflow in the SEHO. Meaburn (1984) previously found the 30 Doradus nebula to be a primary source of outflowing gas, but the Parkes data cube reveals this phenomenon to be more widespread, encompassing the entire SEHO.

2.6.3 Tracing Arms B and E

The HI arm B from the LMC can be traced back to its origin in the region around SGS 18 and 20, as can be seen in Figures 2.22f–r and Figure 2.25. There are two main strands of arm B, a northern and southern strand (Figs. 2.20a, c), each very thin (about $\sim 0.25°$ wide) but with distinct velocities. The northern strand appears to emanate around $(\alpha, \delta, V_{\mathrm{LSR}}) \approx (05^{\mathrm{h}}38^{\mathrm{m}}32^{\mathrm{s}}, -70°39'16'', 273$ km s$^{-1}) = (5.6422°,$ $-70.6544°, 273$ km s$^{-1})$ (Fig. 2.22f and Fig. 2.25b, c) near the intersection of SGS 20 and 18. The southern strand of arm B is at lower velocity than the northern strand (by ~ 30 km s^{-1}) and appears to emanate around $(\alpha, \delta, V_{\mathrm{LSR}}) \approx (05^{\mathrm{h}}38^{\mathrm{m}}09^{\mathrm{s}},$ $-71°07'08'', 200$ km s$^{-1}) = (5.6358°, -71.1189°, 200$ km s$^{-1})$ (Fig. 2.25a) in SGS 18. In Figure 2.25a there appears to be a second parallel filament at the same velocity as the southern strand farther to the south. Since we don't have distance information there are projection effects which make it difficult to pinpoint exact origins for the arm B filaments. Therefore, the locations given above should be considered rough estimates. However, it is clear that arm B originates in the SEHO region. Arm E is

wider, more diffuse, and on average at higher velocity than arm B. Arm E appears to emanate from many outflows across the SEHO region. There is a trend that, moving eastward, the outflow sites move to the north and to higher velocity, which is also a general trend in the SEHO.

It is unclear why the two arms are moving in the directions they are (arm E to the south, and arm B to the southwest) even though they originate in the same place. The two outflow blobs mentioned above show that the gas must first reach a certain positive velocity offset ($\sim$30 km s^{-1} for the SGS 1 outflow, and $\sim$20 km s^{-1} for the SGS 20 outflow) from the systematic SGS or LMC disk velocity before it starts to move appreciably from its place of origin. This might tell us something about the forces operating on the gas. The motions of the two arms/filaments might be related to which side of the disk they are on. Since the LMC disk is inclined relative to its direction of motion through the MW halo any gas blown out in "front" of the disk (towards the direction of LMC bulk motion) will experience more ram pressure than gas blown out "behind" the disk (away from the direction of motion). All of the outflow gas is at higher positive velocities and it would seem likely that the gas is on the opposite side of the LMC from our perspective and in "front" of the LMC as it moves through the MW halo (this is discussed further in §2.6.7). More investigation is needed to explain the motions of the two filaments.

2.6.4 Mass Accounting

We can estimate the mass of H$\textsc{i}$ gas in the outflow blob (Fig. 2.23) as well as the mass evacuated from the SGSs and see how they compare. The mass of the blob of gas (within $05^{\mathrm{h}}39^{\mathrm{m}}32^{\mathrm{s}} < \alpha < 05^{\mathrm{h}}47^{\mathrm{m}}37^{\mathrm{s}}$, $-71°26'02'' < \delta < -70°46'53''$, 267.4 km s^{-1} $< V_{\mathrm{LSR}} < 280.6$ km s^{-1}) is $\sim 1.5 \times 10^6$ M$_\odot$ (using an LMC distance of 50 kpc).

Fig. 2.23.— Integrated intensity of the LMC H I gas from S03 showing the outflow of gas from SGS 20, centered at $(\alpha, \delta, V_{\text{LSR}})= (05^{\text{h}}43^{\text{m}}09^{\text{s}}, -71°08'46'', 270 \text{ km s}^{-1})$. ($a$) Column density, N_{HI}, in units of 10^{19} atoms cm^{-2} (integrated from $266 < V_{\text{LSR}} < 277$ km s^{-1}), (b) V_{LSR} vs. α (integrated from $-71°26'34'' < \delta < -70°59'00''$; the greyscale is in units of K), and (c) V_{LSR} vs. δ (integrated from $05^{\text{h}}39^{\text{m}}48^{\text{s}} < \alpha < 05^{\text{h}}44^{\text{m}}54^{\text{s}}$; the greyscale is in units of K). The locations of SGS 20 and 18 are shown in all three panels. Even though the outflow is spatially more aligned with SGS 18 than SGS 20 (in panel (a)) it is clear from panels (b) and (c) that this is a projection effect. The outflow of gas is connected in position and velocity to the bubble of gas that is surrounding SGS 19 and 20 (see Figs. 2.21 and 2.22), but has moved farther to the south and hence is spatially in front of SGS 18. This figure shows that SGS 20 is blowing out a large amount of gas from the LMC.

We can estimate the mass of the HI gas that has been evacuated from SGS 19 and 20 by calculating the difference in N_{HI} inside and outside the SGSs. The average N_{HI} in SGS 19 and 20 is $\sim 3.54 \times 10^{21}$ cm^{-2} and $\sim 3.50 \times 10^{21}$ cm^{-2} respectively, while for the surrounding region it is $\sim 4.90 \times 10^{21}$ cm^{-2}. Using the area of SGS 19 and 20 from Kim et al. (1999) (circles with diameters of 52.0$'$ and 49.4$'$ respectively) we estimate the mass lost from SGS 19 to be $\sim 1.6 \times 10^{6}$ M$_{\odot}$ and $\sim 1.5 \times 10^{6}$ M$_{\odot}$ lost from SGS 20. These masses are remarkably close to the mass of the outflow blob. However, this estimate ignores the possibility that a sizeable fraction of this lost gas has probably been swept up by SGS winds and gone into compressing the surrounding ISM. Nonetheless, even if only half of the lost gas has been blown out of SGS 19 and 20 it is sufficient to explain the outflow blob.

There is another outflow blob of gas to higher velocity from SGS 1 (Fig. 2.24), which is a SGS in arm B (the LMC filament) located at $(\alpha, \delta) = (04^{\mathrm{h}}58^{\mathrm{m}}36^{\mathrm{s}}, -73°33'57'')$ with a mean velocity of $V_{\mathrm{LSR}} = 242$ km s^{-1}, size of $(48.6' \times 45.4')$ and age of 3.0 Myr (Kim et al. 1999). SGS 1 and the outflow can be seen in Figure 2.24. The outflow first shoots to higher velocity by ~ 27 km s^{-1} at nearly the same position and then moves south $\sim 0.5°$, where the densest portion is positioned (Fig. 2.24c). The blob appears to have two clumps that are separated in α by $\sim 0.5°$ (Fig. 2.24b) (Fig. 2.24a). The outflow must have substantial tangential motion in order to have moved $\sim 0.5°$ (corresponding to ~ 0.44 kpc) in ~ 3 Myr, or it is older than Kim et al. (1999) determined. The mass of the blob (within $04^{\mathrm{h}}49^{\mathrm{m}}30^{\mathrm{s}} < \alpha < 05^{\mathrm{h}}05^{\mathrm{m}}48^{\mathrm{s}}$, $-74°20'04'' < \delta < -73°31'10''$, 267.4 km s$^{-1} < V_{\mathrm{LSR}} < 288.0$ km s^{-1}) is $\sim 7.1 \times 10^{5}$ M$_{\odot}$, which is about half the mass of the outflow blob coming from SGS 19 and 20. These examples of SGSs blowing out massive amounts of gas are strong evidence that the SGSs in the SEHO are capable of blowing out substantial amounts of gas, and, if chained in a
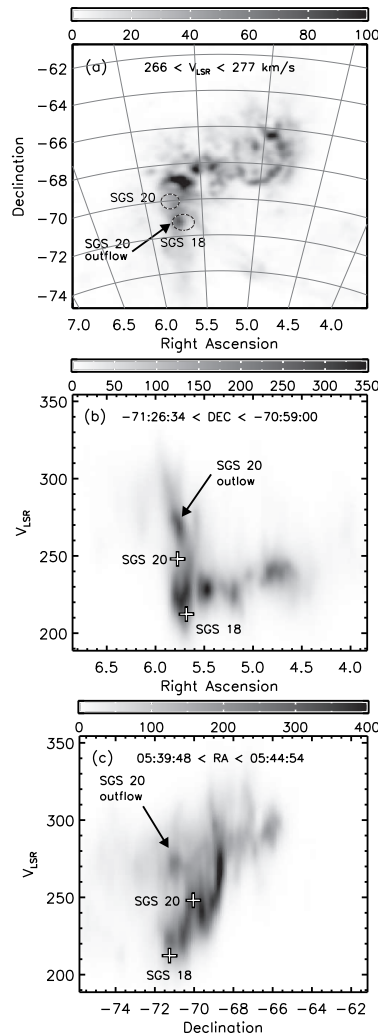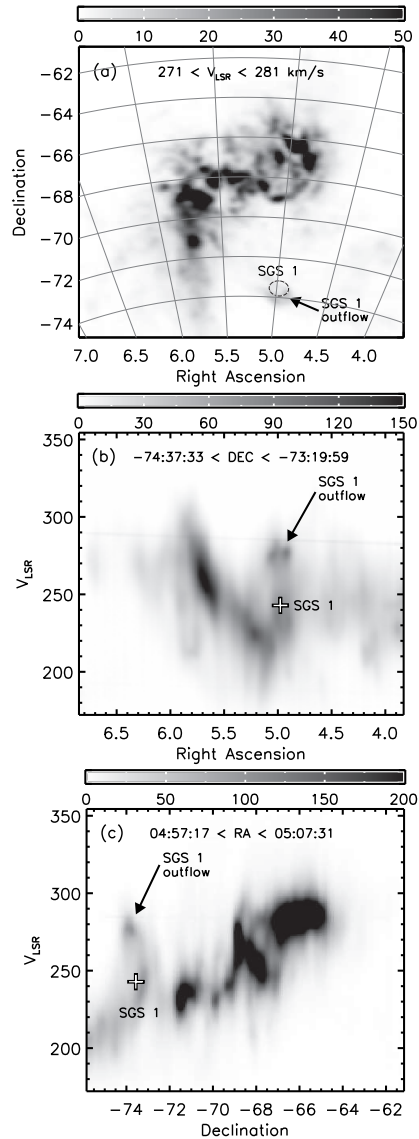
Fig. 2.24.— Integrated intensity of the LMC H I gas from S03 showing the outflow of gas from SGS 1, centered at $(\alpha, \delta, V_{\mathrm{LSR}}) = (04^{\mathrm{h}}58^{\mathrm{m}}36^{\mathrm{s}}, -73°33'57'', 275 \ \mathrm{km \ s^{-1}})$. (a) Column density, N_{HI}, in units of 10^{19} atoms cm^{-2} (integrated along V_{LSR} for $271 < V_{\mathrm{LSR}} < 281 \ \mathrm{km \ s^{-1}}$), (b) V_{LSR} vs. α (integrated along δ for $-74°37'33'' < \delta < -73°19'59''$; greyscale in units of K), and (c) V_{LSR} vs. δ (integrated along α for $04^{\mathrm{h}}57^{\mathrm{m}}17^{\mathrm{s}} < \alpha < 05^{\mathrm{h}}07^{\mathrm{m}}31^{\mathrm{s}}$; greyscale in units of K). This shows that SGS 1 is blowing a substantial amount of gas out of the LMC filament. This also suggests that there may be recent star formation going on in the Magellanic Stream and there might be some young stars there.
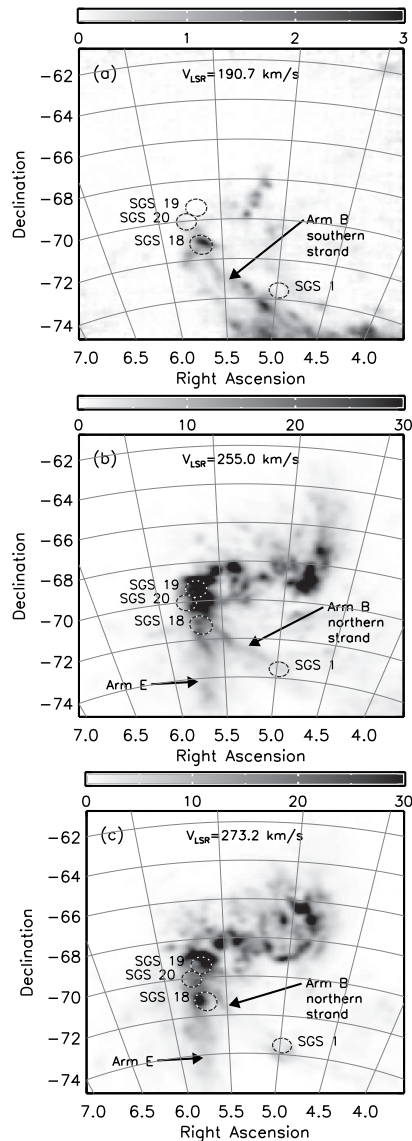
Fig. 2.25.— Velocity slices of the H I datacube from S03 showing where the filaments of arm B (the LMC filament) and arm E (the LAF) originate (the greyscales are in units of K). The outlines of SGS 1, 18, 19 and 20 from Kim et al. (1999) are also shown. In panel (a) at $V_{\mathrm{LSR}} = 190.7$ km s^{-1}, the two southern filaments of arm B (with fairly faint T_{B}) appear to originate in SGS 18. In panel (b) at $V_{\mathrm{LSR}} = 255.0$ km s^{-1}, the northern filament of arm B and a part of arm E seem to originate in SGS 18. Panel (c) at $V_{\mathrm{LSR}} = 273.2$ km s^{-1}, the northern filament of arm B emanates from the north-western part of SGS 18. Dense knots of H I gas around SGS 19 and 20 seem to be the source of some of the arm E gas.

series of propagated star formation events, creating the Leading Arm and the trailing LMC filament of the MS.

SGS 1 lies well outside (by $\sim 2°$) the LMC HI disk as defined in Figure 2.20, and matches arm B perfectly in position and velocity (Fig. 2.24). We have argued in §2.5.3 that arm B is the beginning of the LMC filament of the MS. If SGS 1 is indeed a part of arm B, as all evidence points, and our explanation of arm B is correct, then this implies that there is ongoing star formation at the head of the MS and that there are probably some young stars in the Stream.

The HI mass of the entire LMC is $\sim 4.8 \times 10^8$ $M_\odot$ (S03), while $\sim 1.3 \times 10^8$ $M_\odot$ of that is in the high-velocity gas. The mass of arm B is $\sim 4.9 \times 10^7$ $M_\odot$, that of arm E is $\sim 6.9 \times 10^7$ $M_\odot$, and $\sim 1.2 \times 10^7$ $M_\odot$ is to the west of arm B. This high-velocity gas constitutes 27% of the measured HI mass of the LMC and $\sim 1/3$ the combined mass of the MS and LAF (which have $\sim 3.8 \times 10^8$ $M_\odot$ and $\sim 3 \times 10^7$ $M_\odot$ respectively; B03). Thus the LMC has just recently blown out and lost a substantial amount of mass from the SEHO. It therefore seems plausible that over an even more extended period of time the SEHO might have produced the Magellanic Stream and LAF.

What is the mass ledger like for this hypothesis? The total mass within the volume of a SGS in the SEHO of the LMC with an average diameter of $50'$ (or 0.72 kpc) is $\sim 1 \times 10^7$ $M_\odot$. If 10% of the mass within a SGS is blown out of the LMC disk, then each SGS contributes $\sim 1 \times 10^6$ $M_\odot$ of gas to the MS and/or LAF. If the Magellanic Stream originated in the SEHO and was blown out by SGSs, then some ~ 410 shells would have been required to have created the Stream. If the Stream is ~ 1.74 Gyr old (from §2.5.5), then the average SGS creation rate would have to be 1 per ~ 4.2 Myr. If the shells are coherent and observable for ~ 10 Myr, which appears to be the maximum age of shells in the LMC (Kim et al. 1999), then approximately 2–3 should

be seen in the SEHO at any time. This is the number currently observed (SGS 18, 19, and 20).

Of course, one issue with the MS and LAF originating in the SEHO is that the current H I mass of the SEHO ($\sim$1.3$\times$10^8 M$_\odot$) is now smaller than the H I mass of the entire Stream. There are several possible explanations for this discrepancy: (1) the SEHO was more massive in the past, (2) the SEHO is continually being replenished by gas from the LMC disk, or (3) the SEHO is continually growing by accreting from the hot, coronal MW it is plowing through. Since the current H I masses of the LMC and SMC are roughly the same, moving the origin of the MS and LAF from the LMC to the SMC does not solve the mass problem. The system from which the MS and LAF originate has lost a substantial amount of gas recently and must have contained at least double the H I in the past.

On the other hand, is it possible for the SGS creation rate and gas outflow to be sustained for $\sim$1.74 Gyr? According to Kim et al. (1999), the continual creation of SGSs can be achieved by self-propagating star formation, which is observed in the 30 Doradus complex. Therefore, it appears plausible for there to have been continuous star formation and SGSs blowing out gas sufficient to form the MS+LAF for an extended amount of time in the SEHO. This is discussed further in section 2.7.2

2.6.5   Energetics of the Supergiant Shell Blowout

Is it energetically realistic to suppose that SGSs have blown out the MS and LAF? The energy that would be required to blow out the entire mass of the MS and LAF ($\sim$4.1$\times$10^8 M$_\odot$) to a velocity of $\sim$50 km s^{-1} is $E = (1/2)M_{\mathrm{MS}}v^2 \approx 1.0 \times 10^{55}$ ergs. Since the average kinetic energy released by a SNe is $\sim$10^{51} ergs (Woosley & Weaver 1986; Cho & Kang 2007) this would require $\sim$10,000 SNe. If half of the SNe kinetic

energy in an SGS goes into sweeping up gas and compressing the ISM in the disk and the other half blows out gas perpendicular to the disk, then the combined energy of $\sim$20,000 SNe are required. Spread out over $\sim$1.74 Gyr gives an average SNe rate of 1 every $\sim$87,000 years. This is fairly low compared to the MW SNe rate of 1 every $\sim$100 years and the LMC rate of 1 every $\sim$500 years (van den Bergh & Tammann 1991). If the SNe are divided into $\sim$410 SGSs then each SGS would contain $\sim$49 SNe. The 30 Doradus nebula contains 39 O stars, 12 Wolf-Rayet stars and 8 B supergiants that will all eventually go supernova (Melnick 1985) a tally that validates the plausibility of our estimates. Therefore, the energetics appear to be favorable to the SGS blowout hypothesis.

2.6.6   Magnetic Fields in the SE Hɪ Overdensity

Haynes et al. (1991) performed a radio continuum survey of the Magellanic Clouds at 2.45, 4.75, and 8.55 GHz. In the linearly polarized maps of the LMC Haynes et al. discovered that two thin, long ($\sim$3–4 kpc) filaments (stretching south of the 30 Doradus nebula) dominated the emission (most obvious at 2.45 GHz or 12 cm; see Fig. 2.26a here or their Fig. 7). Xu et al. (1992) separated the thermal (free-free) from the nonthermal (synchrotron) emission and found that, while there is relatively uniform, nonthermal radiation present across most of the LMC (indicating pervasive magnetic fields), the region extending south of the 30 Doradus nebula (where the filaments are located) contains almost entirely thermal emission (see their Figs. 10a and b).

With the addition of observations at 1.4 GHz, Klein et al. (1993) used the radio continuum data to study the 3D magnetic field structure of the LMC, and found that the magnetic field in the region of the filaments was significantly aligned (i.e. not
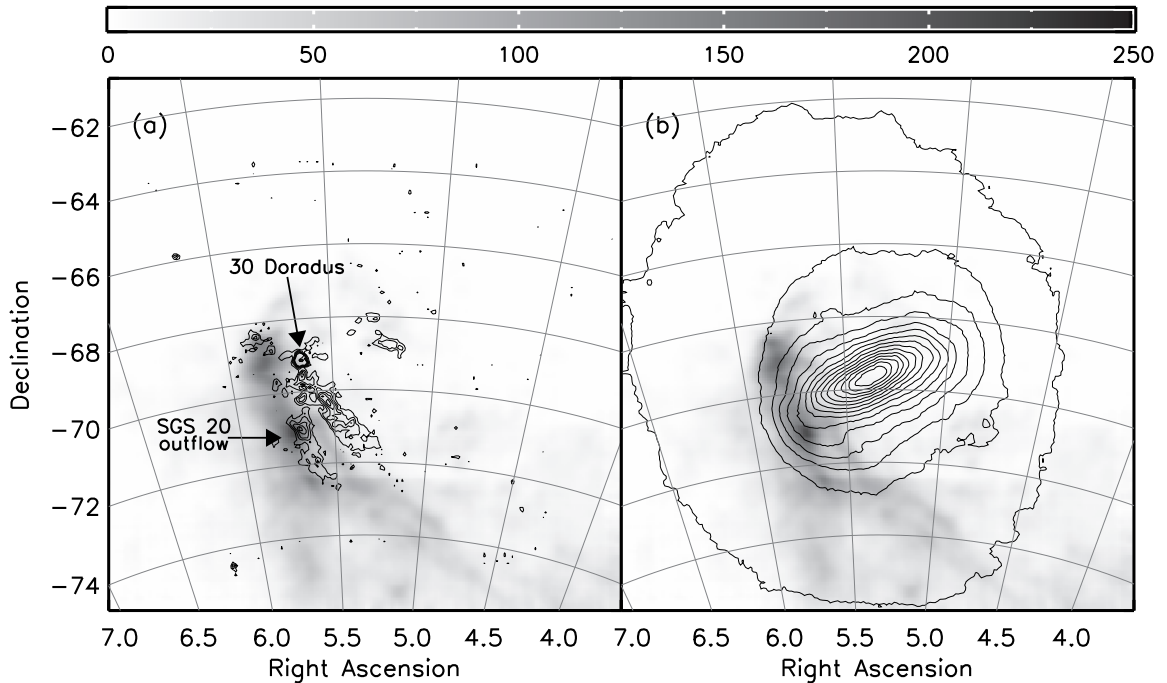
Fig. 2.26.— The sky distribution (column density, N_{HI}, in units of 10^{19} atoms cm^{-2}) of the high-velocity component of the LMC HI gas from the S03 datacube (same as Fig. 2.20c). (*a*) The 12 cm linearly polarized radio emission from Klein et al. (1993) is overplotted as contour lines and shows the two magnetic "filaments". There is strong emission from 30 Doradus, the SGS 20 outflow blow (also see Fig. 2.23), as well as two filaments which are parallel to the high-velocity gas, especially arm B. The eastern polarized filament appears to be associated with the SGS 20 outflow blob. The polarized and HI sets of filaments seem to be anti-correlated and a small correlation coefficient of 0.30 bears this out. (*b*) The density of 2MASS LMC red giant branch stars (Skrutskie et al. 2006) is overplotted with contour lines showing the central stellar LMC bar. The eastern end of the bar is near the region where most of the high-velocity gas is originating. The proximity of the end of the bar might be partly responsible for the high-density of HI gas and perturbed dynamics in this region of the LMC.

random), and oriented more or less parallel to the filaments' direction. In addition, the most extreme rotation measures (RM) — an indication of the magnetic field parallel to the line-of-sight — were in this region. Klein et al. conclude that there is a giant magnetic loop bending out of the plane of the LMC towards us (see their Fig.

6). We compare the high-velocity gas with the linearly polarized filaments from Klein et al. in Fig. 2.26a. The two groups of filaments (high-velocity HI and "polarized") are offset from each other. In fact, they appear to be anti-correlated with a low correlation coefficient of 0.30. One exception is a small region near SGS 18 (and the SGS 20 outflow blob) that is bright in the polarized emission (and in CO as well: Cohen et al. 1988, Fukui et al. 1999), probably indicating that this region is very active. It appears that the eastern polarized filament might originate from there. The western polarized filament might be related to the 30 Doradus nebula. The proximity to each other, filamentary structure, and abnormality (compared to the rest of the LMC) of the two sets of filaments indicates a probable physical relationship between them; the exact nature of that relationship and the origin of the spatial offset remain unclear at this time.

These polarization and magnetic-field studies show that there is something violent happening in the region south of 30 Doradus that is likely related to the high-velocity gas and the SGSs. This corroborates circumstantially our suggestion that the SGSs may be blowing out the HI gas and creating the LMC filament of the Magellanic Stream and the Leading Arm. It is possible that the relativistic ions are being accelerated by the supernovae shocks from the SGSs, and that the aligned magnetic field is being caused by the stellar winds and supernovae shocks (also from the SGSs). It is not entirely clear how the magnetic loop fits into this picture. However, if there are magnetic fields in the Magellanic Stream it might explain how the filaments can remain so coherent over large distances.

2.6.7   Relative Distance of the High-Velocity Gas

There is some diagreement about whether the anomalous ("high-velocity") gas is in front of or behind the LMC disk. Luks & Rohlfs (1992) conclude that the low-velocity component is in front of the high-velocity component since they find no absorption of the 30 Doradus emission (associated with the low-velocity component) by the high-velocity component. Points et al. (1999) used ROSAT data to study the supergiant shell LMC 2 (SGS 19). They detected no X-ray absorption features that correlated spatially with the distribution of the high-velocity gas. Based on this evidence they concluded that the high-velocity gas is behind the plasma in LMC 2 (which presumably is in the disk of the LMC). However, this study only looked at a small subsection of the LMC.

Dickey et al. (1994) performed an absorption-line study of several sight-lines in the LMC. They used a kinematical argument to conclude that the high-velocity component is in front of the low-velocity component. Since the LMC disk is inclined, a cloud at a height above the LMC disk plane (and following the same rotation curve) will have an actual LMC-centric distance that is different than the projected one and therefore will have a different rotational velocity than the rest of the gas along that same sight-line (that is in the disk). Whether the rotation velocity will increase or decrease depends on the exact sight-line, and this information is embodied in a "velocity gradient"(dv/dr). Dickey et al. calculated the velocity gradient for each position at which they detected absorption lines using the smoothed velocity field by Luks & Rohlfs (1992; their Fig. 9) and assuming that the north-east is the near side of the LMC. Based on the velocity gradient at each position and the radial velocity offset from the disk radial velocity at that point, they conclude that the low-velocity gas is on the far side of the disk and the high-velocity gas is in front.

The kinematical argument by Dickey et al. works fairly well for arm B, which moves across a large part of the LMC. Based on the velocity gradient its velocity offset should at first be positive, then zero, and then negative, and this is actually what is observed. However, there is a problem with the gas "blobs" that are being blown out of the SGS mentioned above (§2.6.2). The gas moves to higher velocity at nearly the same position which would be interpreted to mean, without considering the rotation curve, that the gas is moving away from us. Furthermore, since it seems clear now that most, if not all, of the high-velocity gas in the south-eastern portion of the LMC is coming from the SGSs, the high-velocity gas should be on the same side of the disk as the "blob" gas. Even though the kinematical argument of Dickey et al. seems realistic, it assumes that the gas out of the disk plane is also in circular motion. However, we question if this assumption is a valid one. It is clear that the LMC's gravity is not the only force acting on the gas. As already stated, it seems clear that the SGSs are blowing gas out of the disk (probably away from us), and since arm B becomes the ~100° trailing LMC filament of the MS, tidal or ram pressure forces must be acting on it. Therefore, it seems unlikely that a simple model with the gas in relative equilibrium, such as proposed by Dickey et al., will work correctly in this highly dynamical situation with various contributing forces.

Finally, Klein et al. (1993) claim that two filaments visible in the linearly polarized emission are on the near-side of the disk. They conclude that the filaments are outside the disk since their rotation measures are much lower than would be expected if they were inside the LMC disk. The rotation measures would also be higher than expected if the filaments were on the far side of the disk. Due to the anti-correlation of the high-velocity HI and "polarized" filaments (mentioned above) it is doubtful that the claims by Klein et al. about the polarized filaments can be used to ascertain the position of

the high-velocity HI gas relative to the disk. However, the possible association of the HI filaments with the polarized filaments, and the "magnetized loop" hypothesized by Klein et al., deserve further study.

We conclude that the high-velocity gas of both arms E and B is on the far side of the LMC, mainly because we are attributing the dynamics to the force of the SGSs blowing out gas to higher velocity, and this must put higher-velocity gas away from us. This is consistent with the conclusions of both Luks & Rohlfs and Points et al., but inconsistent with Dickey et al. as well as with the Klein et al. assessment of the polarized filaments.

2.7 Discussion and Summary

Our exploration of the Magellanic System using a Gaussian decomposition of the LAB data in combination with other radio data has led us to several conclusions regarding the nature and origin of the Magellanic Stream.

2.7.1 The Large Magellanic Cloud as Progenitor of the Magellanic Stream and Leading Arm Feature

We have found evidence that one of the filaments of the Magellanic Stream and the Leading Arm can be traced back to the LMC and that both of these HI structures originate there. In our database of HI Gaussians the MS appears as two filaments as has been previously reported by Putman et al. (2003). But, capitalizing on the coherence of the filaments in ppv (position–position–velocity) space, we were able to track one of them back to the LMC in both velocity and position. After isolating the HI of this filament in one of the position-velocity diagrams (V_{LSR} vs. L_{MS}), we

were able to show that it originates in the SEHO of the LMC. Likewise we showed that the first complex of the LAF (LA I) begins (in position and velocity) near the end of S03's arm E from the LMC. The spatial and velocity progression of the three concentrations of LA I and arm E, as well as their continuity in the deeper HIPASS data, strongly suggest that they are physically connected.

An LMC origin of the MS is contrary to much of the current literature, which has largely supported an SMC/Bridge origin for the MS (e.g., P03 and B05). Even most modeling papers (especially those based on a tidal origin of the MS) have started with the SMC/Bridge assumption and adopt an N-body representation of the SMC influenced by only a static LMC (and MW) potential (e.g., Gardiner & Noguchi 1996; Yoshizawa & Noguchi 2003; Connors et al. 2004, 2006). Therefore, these models *by design* rely on the MS forming from the SMC and not the LMC. Models that represent *both* the LMC and SMC as N-bodies (Murai & Fujimoto 1980; Růžička et al. 2006) have also concluded that most of the Magellanic Stream came from the SMC; however, these simulations do show at least some debris coming off the LMC and this debris follows the position and velocity distribution of the main body of the Stream. The main reason that an SMC origin was preferred is because *more* material came off the SMC than the LMC in these models. The reasons cited for this observed mass-loss inequity is that the SMC potential is weaker than the LMC's and that the LMC has a much larger tidal influence on the SMC than vice versa. Even though these statements may be correct in the context of these models, it is likely that these models are missing important physical processes: none of the simulations include the potentially important dynamics of LMC star formation and SGSs that may *greatly* enhance gas outflow from the LMC. If SGSs propel gas faster than the escape velocity, this gas can then be swept away from the MCs by tidal and/or ram pressure forces.

Future simulations including these effects *subsequent* to blowout may come closer to matching the HI structural features that we have observed. First steps towards this goal have already been taken by Olano (2004) who has already demonstrated that blowout from the MCs can create the large scale features of the MS, as well as the HVC system of the MW. Olano's model explored blowout from the MCs that results from an interaction between the two Clouds 570 Myr ago. Our analysis here identifies a more specific site (the SEHO of the LMC) and timescale ($\sim$1.7 Gyr) for the creation of the MS that we believe ought to be accommodated by such models.

With the discovery of the two filaments of the MS (P03) it was suggested that one of the filaments originates from the Bridge, and that therefore the Bridge might be older than the $\sim$200 Myr suggested by the models of Gardiner et al. (1994) and the young blue stars discovered between the Magellanic Clouds by Irwin et al. (1990). However, now that this same HI filament can be traced to the LMC there is no reason to believe that the Bridge is old. In fact, the recent study of stellar populations in the Bridge by Harris (2006) shows that there are only young stars there and that star formation started in the Bridge only some 200–300 Myr ago.

According to Russell & Dopita (1992), the current mean metallicities of gas in the LMC and SMC are [Fe/H]$= -0.2\pm0.2$ and -0.6 ± 0.2, respectively, while the average metallicity of the MS is [Fe/H]$= -0.6\pm0.2$ (Wakker 2001). At first glance it appears that the metallicity information points towards an SMC origin of the MS. However, it is not the current metallicity of the MCs that is important, but the metallicity at the time that each part of the MS left the Clouds, starting around 1.74 Gyr ago (so that one might expect a metallicity gradient along the Stream). According to Pagel & Tautvaisiene (1998), the metallicities of the Clouds were $\sim$0.3 dex lower $\sim$1.7 Gyr ago, which would put them at [Fe/H]≈ -0.5 (LMC) and [Fe/H]≈ -0.9

(SMC). Thus, even though metallicity provides only a weak discriminant of the MS origins, it appears to slightly favor an LMC origin over an SMC origin.

Moreover, there continues to be a global problem reconciling large observed variations in the metallicities of different gaseous Magellanic features. For example, the low metallicity of the Bridge, [Fe/H]$= -1.1$ (Lehner 2002), compared to [Fe/H]$= -0.6$ for the SMC (where it is thought to have originated), has been used to argue that the Bridge is old. However, because other evidence supports a young age ($\sim$200 Myr) for the Bridge (see above), the enrichment level of the gas must be more complex than mere mass loss from a simple closed box model of the MCs. For example, Lehner (2002) suggests that the Bridge gas from the SMC may have mixed with other, less enriched gas. One possible source of less enriched gas could be earlier gas ejections from the SMC itself which could be accreted. Another possible explanation for the low metallicity of the Bridge gas is that it could have originated from gas in the outskirts of the SMC that might be more metal-poor than gas in the central part of the SMC. Whatever the explanation is, it seems clear that it is difficult at present to interpret the relative metallicities of Magellanic gas and the MCs.

2.7.2 Origins in the SE H I Overdensity

We have been able to track the MS back to the LMC, and argue, in §2.6, for its origin in the SEHO. What remains unresolved is whether the physics creating this intense star-forming region is tied to a particular, fixed dynamical hot spot that is the product of the bulk motion of the LMC, its rotation, and interaction with MW halo gas, or whether the SEHO participates in the general LMC rotation. The answer bears on how to evaluate an accounting of relative ages, masses, and energetics between the SEHO site and what is needed to produce the MS and LAF and their

apparent oscillations.

For example, de Boer et al. (1998) suggest that the leading edge of the LMC (the SE, where the SEHO is presently located) is being compressed as the LMC moves through the diffuse halo of the MW (creating a bow-shock), which produces a steep HI gradient (as observed), and triggers star formation. In this scenario, the southeast quadrant of the LMC will always remain an active star-forming site, with previous generations of stars formed there rotating off of the hot-spot due to LMC rotation, but with the evolution of massive stars constantly regenerating SGSs near their birthplace. This argues for considering a broader perspective in evaluating the age and energetics of MS production. Unfortunately, while it is obvious that there has been much recent star formation occuring in the 30 Doradus (Tarantula) nebula and its *immediate* surroundings, the star formation history of the SEHO and the annulus of the LMC it occupies have been less well established. But from our assessment of the mass, age, and required energy needed to produce the MS and LAF (§§2.6.4 and 2.6.5) we can hypothesize some general expectations.

We have given evidence in §2.6 that SGSs in the SEHO are currently blowing out gas and creating the MS and LAF. This scenario is supported by the high-speed outflows from the 30 Doradus starburst (Redman et al. 2003) and by the energetic outflows from the LMC (Lehner & Howk 2007). From the continuity of the MS we can infer that this process must have been going on continuously at a rate steady enough to not create gaps in the MS. In the de Boer et al. scenario one might expect a continuous cycle of star formation, SGSs, and gas blowout as long as the compression and bow-shock are present. As discussed in §6.3, to eject the $\sim4.1\times10^8$ M$_\odot$ of the MS and LAF out of the SEHO in ~1.7 Gyr would require ~400 SGSs (each blowing out $\sim10^6$ M$_\odot$). This exceeds the current HI mass of the SEHO ($\sim8\times10^7$ M$_\odot$, excluding the

high-velocity gas), but this comparison belies a complex calculus of mass exchange. On the one hand, some HI from the SEHO is converted into stars and stellar remnants, while some is lost to SGS blowout to produce the MS and LAF, and additional HI gas can be generated from the destruction of H_2, although this is likely to be a small amount.[5] On the other hand some gas may be inflowing from the MW halo (and indeed may be the source of less enriched material complicating the metallicity accounting discussed above).

If the MS and LAF were formed as part of the de Boer et al. scenario, then a >1.7 Gyr age for these gaseous structures is viable, but the star formation that produced these features would have created stellar populations that would have rotated around the LMC about five times. Therefore, we would expect that the stellar populations at any position in a 2 kpc radius to have five distinct peaks in age corresponding to the times when this position was in the SE corner of the LMC where the vigorous star formation is occurring. These peaks should be separated by ∼340 Myr (i.e. the LMC rotation period at this radius) but with approximately the same star formation rate. The exact ages of these peaks should be shifted with position in the 2 kpc annulus – older as you move clockwise (with the LMC rotation) and younger in the opposite direction. The total number of stars younger than ∼1.7 Gyr should be approximately constant with position around the 2 kpc annulus. Thus, a detailed analysis of the star formation history of the 2 kpc annulus could be used to check the validity of the de Boer et al. scenario. Unfortunately, radial and azimuthal mixing of stars in the LMC disk might smear out some of these patterns which could make this analysis difficult in practice.

It is not clear what caused the vigorous star formation in the SEHO region to

---

[5]According to Young & Scoville (1991) the mass in molecular hydrogen is typically an order of magnitude less than that in atomic form for very late-type spirals.

start ~1.7 Gyr ago and commence the SGS blowout and formation of the MS and LAF. One possibility is that the LMC and SMC had a close encounter that could have triggered star formation. The integrated star formation histories of the LMC (Harris & Zaritsky 2004) and SMC (Smecker-Hane et al. 2002) both show a "burst" of star formation ~2–2.5 Gyr ago which suggests that an interaction between the MCs might indeed have occurred around that time. The LMC globular cluster age–gap between 3 and 13 Gyr (e.g., Da Costa 1991; Geisler et al. 1997; Rich et al. 2001; Piatti et al. 2002) indicates an onset of star formation in the LMC around ~3 Gyr ago, however, such an age–gap is not seen in the SMC clusters (Da Costa 1991). As previously mentioned in §2.5.5, the orbits by Besla et al. (2007) indicate possible encounters of the MCs with each other around 0.2, 3 and 6 Gyr ago. Therefore, it does not seem unrealistic to suppose that a close encounter of the MCs ~2–3 Gyr ago triggered star formation in the LMC and SEHO region. Another possibility might be that ~1.7 Gyr ago the LMC was close enough to the MW that ram pressure due to the hot MW halo created a bow shock and started star formation in the SEHO (jump starting the de Boer et al. scenario mentioned above). However, according to the hyperbolic orbits of Besla et al. (2007) the LMC was ~300–500 kpc from the MW at this time (depending on the MW mass); even though the density of the gaseous MW halo is not well known it is doubtful that the density at those distances could be large enough to create the bow shock necessary to start star formation in the LMC. The trigger of the recent, vigorous star formation in the SEHO region of the LMC therefore remains an open, and interesting question.

It should be acknowledged that the SMC also has many giant shells and SGSs (Staveley-Smith et al. 1997), and it might be expected that the SMC is also blowing out gas that might be contributing to the MS. For example, it may be that the second

filament of the MS is coming from the SMC. Unfortunately, we have no evidence to support or disprove this based on our analysis. The lack of an obvious major source of frenetic star formation activity in the SMC may substantially lower the efficiency of and amount of SMC blowout relative to that in the LMC. Whether the SMC contributes to the MS and by how much requires further work to determine.

2.7.3   The Sinusoidal Velocity Pattern of the LMC Filament

Among the most striking features of the MS, as seen in Figures 2.9b and 2.10, are the velocity oscillations of the two filaments. These sinusoidal patterns have not been previously observed or predicted. We have hypothesized that this pattern for the LMC filaments may be an imprint of the motion of the gas ejection site according to the LMC rotation curve. Using this hypothesis, we estimated that the drift rate of the MS gas away from the LMC is $\sim$49 km s^{-1}, and, based on the length of the entire MS, we surmise that the MS is $\sim$1.7 Gyr old. As we mentioned in the previous subsection, this estimate of the age of the MS is fairly consistent with other studies.

However this hypothesis contradicts the de Boer et al. (1998) scenario by invoking the SEHO as a rotating star-formation site. In this case, the multiple generations of stars formed in this process should still be relatively near the ejection site. But without replenishment of gas, this scenario may require inordinately large amounts of mass to be processed through one particular star-formation site with no apparent driver and for a relatively long time.

A hybrid hypothesis that could incorporate the driving physics of the de Boer et al. scenario and still produce oscillating patterns in the MS and LAF might include gas streaming along the LMC bar, creating a "perfect storm" of compressional activity when combined with bulk LMC motion and LMC rotation. Kim et al. (1998) show

that the LMC HI velocity field deviates from circular rotation, especially at the north-western end of the stellar bar, and take this as evidence for large-scale streaming motions in the HI. In Figure 2.26b we show the high-velocity HI gas together with the density of 2MASS LMC red giant branch stars (Skrutskie et al. 2006) indicating the stellar bar. The eastern end of the bar is close to the SEHO where the HI filaments originate, suggesting that the bar may play a role in (1) the accumulation of the dense gas in SEHO and (2) the origin of the high-velocity filaments there. However, whereas the end of the bar on the *leading* side of the LMC coincides with intense star formation in the SEHO, no equivalent feature is found on the western side of the bar. If bar streaming provides the critical, extra dynamical contribution necessary for star formation activity at the level needed for persistent blowout, then oscillating motion of the ejection site would naturally correspond to the bar pattern rotation (which is not well known). But this would also imply periodic jumps in location every half period when there is a transition from one end of the bar being on the leading side of the LMC to the other end leading. This motion would be imprinted in the shape and velocity of the MS. Spatial jumps similar to that suggested may be visible (e.g., Fig. 2.13), but they are not as evident in the velocity distribution.

Clearly hydrodynamical modeling is needed to resolve the dilemma of how the ejection site is generated and to understand the expected effects of its motion, or lack thereof, on the MS and LAF. We consider this one of the most important challenges remaining to complete this new picture of how the MS and LAF formed.

2.7.4   Relevance to the Tidal vs. Ram Pressure Models

The MS origins debate has focused on the tidal versus ram pressure models. We have added a new mechanism, SGS blowout, to explain how the MS gas is removed

from the MCs. Once the gas has escaped its host galaxy, ram pressure and/or tidal forces are still required to disperse the unbound gas and move part of it forward (to create the LAF) and other parts backward (to create the MS). Therefore, the blowout model moves the tidal versus ram pressure debate from the mechanism for *removal* of gas from the MCs, to the mechanism for *dispersal* of the unbound gas.

It seems likely that *both* ram pressure and tidal forces are present and needed to explain the characteristics of the MS and LAF: The LAF *cannot* be satisfactorily explained without a tidal force, and ram pressure forces are evidently at work in building the steep density gradient in the leading edge of the LMC. The *combination* of ram pressure and tidal forces can also help explain the column density gradient along the Magellanic Stream (Moore & Davis 1994; Mastropietro et al. 2005) *and* the imbalance of mass in the MS and LAF, since it will be more difficult to move material ahead of the MCs due to the extra force pushing it backwards.

Our proposed scheme for the origin of the MS through blowout resolves a problem that has plagued tidal models, namely the lack of observed stars in the Stream. If most of the MS and LAF gas was blown out of the LMC from SGSs in the SEHO, as suggested here, then no stars would be expected in the Stream. The forces operating in the SGSs that blow out the gas (superwind and supernovae shocks) do not affect the stars, and therefore the mystery of the lack of stars in the Stream, even in the presence of tidal mechanisms, is easily explained.

Our model also resolves the paradox recently posed by Besla et al. (2007) that if the MCs are on hyperbolic orbits, as now indicated by HST proper motions (Kallivayalil et al. 2006a,b; Piatek et al. 2008), then the distance of the MCs from the MW at the time that the MS originated is too large ($\sim$300-500 kpc) for the ram pressure and tidal forces to strip the gas out of the LMC or the SMC. SGS blowout can do the

work of moving the gas to large enough LMC radii to where even weak ram pressure and tidal forces can take over for dispersal in the hyperbolic orbit scenario.

2.7.5 New Constraints For Modeling of the Magellanic Stream

In this paper we have used the detailed spatial and velocity distributions of Magellanic HI gas to lead us to a new paradigm for how the MS and LAF formed, namely through blowout from intense star formation in the SEHO of the LMC. But there are intriguing patterns in the MS and LAF that can provide additional clues at a more detailed level to the processes that shaped them. The most obvious clues are the periodic patterns. Among them:

1. The two MS filaments exhibit large velocity and spatial oscillations. The oscillation of the LMC filament has a velocity amplitude of 26.4 km s^{-1} with an angular period of 19.5° (17.1 kpc at a distance of 50 kpc) in L_{MS} (Fig. 2.17). The amplitude of the spatial oscillation in B_{MS} is $\sim$2° (Fig. 2.13).

2. There are three concentrations in LA I, elongated along B_{MS} ($\sim$2 × 7°) that look very similar to one another and that are each offset by $\sim$12° in L_{MS} and $\sim$9.5° in B_{MS} from the previous one (Fig. 2.8).

3. LA II and LA III are very similar in appearance (Fig. 2.8). They are both elongated along L_{MS} with sizes of $\sim$21 × 5° and parallel to each other (offset by $\sim$20° in B_{MS}).

4. The two filaments of the Magellanic Stream exhibit strong periodic patterns in position, and are composed of clumps elongated along L_{MS} with sizes of $\sim$6.0×1.5°, surprisingly similar in size to the LA I clumps and highly suggestive that they may have formed by the same process (Fig. 2.8b).

5. The two MS filaments are quite similar in appearance and mirror each other in their shape (from $L_{\mathrm{MS}} \approx -15°$ to $-45°$), only shifted by $\sim 1°$ in L_{MS} and $\sim 4°$ in B_{MS} (Figs. 2.8b and 2.13).

Future modeling efforts of the MS should not only incorporate an LMC/SEHO origin for both the MS and LAF, but strive to reproduce these other newly found distinctive observational characteristics of the MS. We propose that such models account for the energetics of supergiant shell blowout in the creation of the MS.

Chapter 3

The 200°–long Magellanic Stream System

3.1 Introduction

In this project we address the question of whether the BT04 emission really is an extension of the MS and if the MS is actually much longer than previously thought. In pursuit of this goal we conducted a 200 deg² Green Bank Telescope (GBT; Lockman 1998) 21–cm survey to bridge the ∼10° gap between the "classical" MS and the features found in the BT04 survey. Our GBT data, in combination with the Arecibo survey of Stanimirović et al. (2008, hereafter S08), demonstrate that the MS *is both spatially and kinematically continuous* across the gap. Therefore, the MS is at least 140° long (∼40° longer than previously thought) and probably even longer, and the entire Magellanic Stream "system" (MS and LAF) is 200° long. In addition, we combine all available HI data of the MS–tip into one datacube to investigate the structural characteristics of the MS in this region. The MS–tip is composed of many thin filaments, as previously noted by S08, but we identify a new filament in the east-

ern portion of the MS that markedly deviates from the equator of the MS coordinate system for more than 45°. Additionally, we find that there is a previously unknown velocity inflection at the MS–tip where the MS radial velocities reach a minimum and then begin to increase. The mass of the new portion of the MS–tip is $\sim 5 \times 10^7$ $M_\odot$ which increases the estimated mass of the entire MS by $\sim$10%.

3.2 GBT Survey

3.2.1 Observations

We used the GBT to conduct an $\sim$200 deg^2 21–cm survey (proposal ID: GBT06A-066, 102 hours) to bridge the $\sim$10° gap between the "classical" MS and the BT04 survey. The survey area is centered on $(l,b) \approx (94°,-40°)$ and extends $\sim$28°$\times$22° in $l \times b$ (but not completely filled; see Fig. 3.5). Our survey area was partly chosen to be complementary to the Arecibo survey of Stanimirović et al. We used the "On-the-Fly" mapping mode (scanning in Galactic longitude) to obtain frequency-switched, 21-cm spectral line data with the Spectrometer back end. The usable velocity range is $-960 < V_{\mathrm{LSR}} < +540$ km s^{-1} with a velocity resolution of 0.16 km s^{-1}. The observations were taken in 49 "bricks" of dimension 2.1°$\times$2.1°. Each brick consists of a 37$\times$37 array of 4–second integrations, with a 3.5$'$ spacing between each integration (which fully samples the GBT 21–cm half-power beam width of 9.2$'$). Neighboring bricks were overlapped by 6$'$ to allow for a consistent calibration across the survey area. The observing pattern of a brick is shown in Figure 3.1; the entire survey area can be seen in Figure 3.5.

During each observing session calibration data were obtained for the IAU standard positions S7 and S8 (Williams 1973), and for our own "secondary" standard position
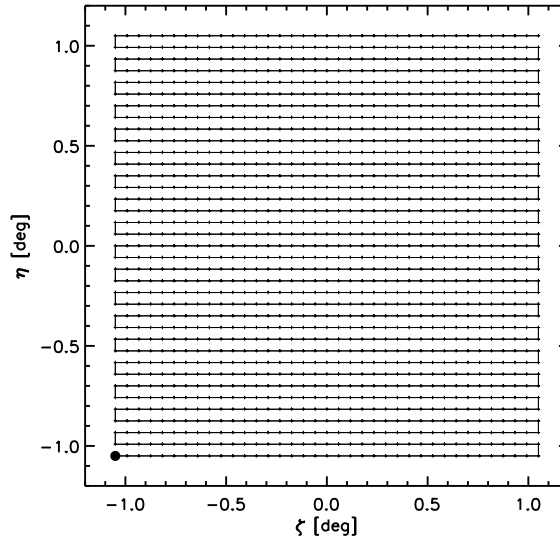
Fig. 3.1.— Our GBT "On-the-Fly" mapping pattern for one 2.1°×2.1° "brick" (37×37 4–second integrations). The large filled dot indicates the starting position. The telescope slewed in Galactic longitude during the observing.

at $(l,b) = (103.0°,-40°)$.

3.2.2 Data Reduction

We used the GETFS program in GBTIDL[1] to calibrate our frequency-switched data using a basic $T_a = T_{sys}^{ref} \times (sig - ref)/ref$ calibration. Each integration and linear polarization was calibrated separately.

During the observing we became aware of a sinusoidal pattern in velocity in the YY polarization which made it difficult to use the standard polynomial baseline fitting routines in GBTIDL. The sinusoidal pattern is a known standing wave with a period of ~1.5 MHz that arises from a total pathlength of ~200 m and a double reflection ($\pm\lambda/8$ focus shifts changing the phase by 180°). The standing wave is highly linearly polarized and only appears in the YY polarization. The origin of the standing wave

[1]http://gbtidl.nrao.edu/

is unknown (A. Minter 2008, private communication).

We used our own special-purpose IDL routines to perform the baseline fitting and removal. Before baseline removal, the data were binned 10× (giving a velocity resolution of ∼1.6 km s^{-1}) to decrease the noise. The baseline was fitted for each integration and polarization separately. For the XX polarization, a 5th-order polynomial was fitted to the 21-cm spectrum but excluding the Galactic emission at $-140 < V_{\mathrm{LSR}} < +100$ km s^{-1}. The fitting process was done iteratively so that emission lines (anything above 2σ in a Gaussian smoothed version of the spectrum) could be excluded from the fit.

Removing the sinusoidal pattern from the YY polarization was difficult because it was below the noise level of an individual spectrum (∼0.12 K), and therefore multiple steps were required. First, a 5th-order polynomial was iteratively fitted to the spectrum excluding Galactic emission and the emission lines previously excluded for the XX polarization. Next, a cosine was fitted to the spectrum with the initial polynomial baseline subtracted. The amplitude and wavelength were held fixed ($A = 0.02$ K, $\lambda = 305$ km s^{-1} [191 binned channels]) and only the phase was allowed to vary (with initial guess $\phi = 192$ km s^{-1} [120 binned channels]). Emission lines were similarly excluded from the fit. Finally, a polynomial+cosine function was fitted to the spectrum using the previously derived parameters as initial guess, and allowing all parameters to vary. The cosine parameters were limited to $0.0 < A < 0.04$ K, $280 < \lambda < 330$ km s^{-1}, and $0.0 < \phi < 400$ km s^{-1}. Galactic emission and emission lines previously excluded for the XX polarization and the initial YY cosine fit were excluded during this final fitting process. For some of the bricks the phase of the sinusoidal pattern shifted slowly with time, but for others it stayed fairly constant. We experimented with many variants of this method and parameter constraints until
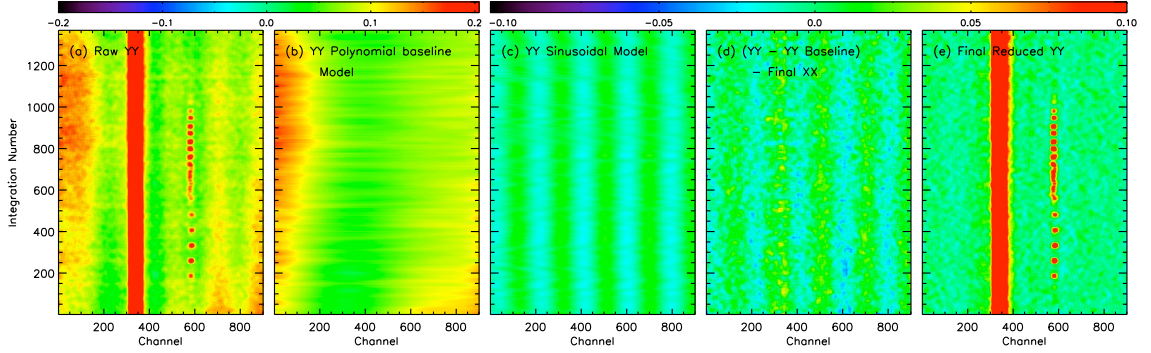
Fig. 3.2.— YY polarization data for the GBT brick centered at $(l,b)=(103.0°,−40.0°)$ showing our GBT baseline reduction steps and the sinusoidal pattern. The three-dimensional datacube (position, position, velocity) is shown in a two-dimensional diagram by plotting the two spatial dimensions on one axis as the sequential "integration number". (a) The raw YY data; (b) the YY-fitted 5th-order polynomial baseline; (c) the YY-fitted sinusoidal baseline model; (d) the polynomial-baseline-subtracted YY data minus the final XX reduced data showing the sinusoidal pattern in the data; (e) the final reduced YY data with both the polynomial baseline and the sinusoidal pattern removed – very little residual baseline is apparent. Each diagram has been smoothed with a 20×20 boxcar filter to make the fainter features more visible. The units of the color scale are K. The local Galactic zero-velocity gas and intermediate-velocity gas is indicated by the red vertical stripe at Channel≈350 and the Magellanic Stream is the vertical streak at Channel≈580. The MS appears clumpy because the integration pattern scans across the MS and the local velocity emission is continuous because it is pervasive.

we converged on the procedure outlined above, which is adequate for our purposes.

Figure 3.2 shows an example of the YY data for one brick. The three-dimensional datacube (position, position, velocity) is shown in a two-dimensional diagram by collapsing the two spatial dimensions on one axis as the sequential "integration number". This makes it easier to visualize the overall features in the data. Each diagram has been smoothed with a 20×20 boxcar filter to make the fainter features more visible.

Our baseline removal process is not perfect and there are some wiggles at the mK level. This is probably due to the effects of incomplete rejection of channels contaminated by wings of emission lines slightly skewing the baseline fits. However,

these baseline ripples do not affect our results for the MS.

After baseline removal, the median (calculated from an emission–free region of the spectrum) was subtracted from each polarization and then the two polarizations were averaged to obtain the final, reduced spectrum for that position. The RMS noise is $\sim$0.072 K per 1.6 km s^{-1} channel and our 3σ sensitivity is $\sim$4.9$\times$10^{18} cm^{-2} over 20 km s^{-1}.

All 49 bricks were regridded onto a single datacube with a Galactic cartesian grid and a 3.5$'$ spacing using the IDL routine TRIGRID with linear interpolation (each velocity channel independently). The datacube was then Gaussian smoothed in velocity (FWHM = 16 km s^{-1}) and spatially (FWHM = 10.5$'$), giving a final RMS noise level of $\sim$0.0075 K per 1.6 km s^{-1} channel. Our 3σ sensitivity is $\sim$5.2$\times$10^{17} cm^{-2} over 20 km s^{-1} in the final, smoothed datacube.

3.2.3 The GBT Hi Ghost

There is a persistent, but weak, emission line permeating our entire GBT datacube (Fig. 3.3 and Fig. 3.4, left panel). This line does *not* appear in the S08 Arecibo datacube or in the BT04 Westerbork datacube that both overlap portions of our survey and are both more sensitive than our data. Therefore, it is clear that this is not a real emission line, but a spurious artifact unique to the GBT data. The line has a Gaussian shape of A=0.004–0.013 K, V_{LSR} =$-$243.8 km s^{-1}, and $\sigma_v\approx$ 7.7 km s^{-1}, and appears in both polarizations (with equal strength) as well as in the pre-baseline-subtracted, frequency-switched data (both positive and negative images). The suspect line maintains a constant velocity and line-width across our entire datacube. The line is not radio frequency interference (RFI) because it is too wide ($\sim$200 unbinned channels) and because it has a constant V_{LSR} (RFI should have a constant velocity in
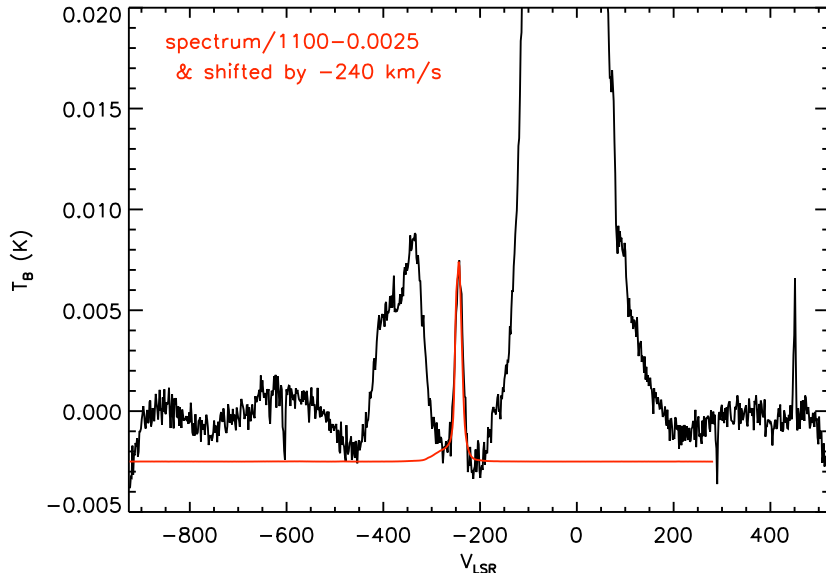
Fig. 3.3.— Average spectrum of our entire GBT datacube. The -243.8 km s^{-1} spurious emission line is clearly visible. A version of the average spectrum scaled by $1/1100$ and shifted by -240 km s^{-1} is overplotted in red and is an exact match to the mysterious line. This implies that the -243.8 km s^{-1} line is in fact a "ghost" spectrum in the GBT data. Some baseline ripples are still apparent in our data at the mK level, as are a few missed RFI lines.

the observer rest frame). The Gaussian shape of the line suggests that it originates from an astronomical source. However, it is unlikely that this is due to the stray radiation from forward spillover of the GBT secondary (Lockman & Condon 2005) because of the stability of the line (especially in $V_{\rm LSR}$ and σ_v) over some 200 deg^2 as well as the large negative velocity.

The only astronomical HI emission line that is so stable over such a large area is the local, Galactic zero-velocity emission. In fact, the line-shape of the -243.8 km s^{-1} emission is a very close match to that of the zero-velocity emission line. The average spectrum of our entire GBT datacube is shown in Figure 3.3 with the -243.8 km s^{-1} emission line clearly revealed. We have overplotted a version of the average

spectrum scaled by $1/1100$ and shifted by -240 km s^{-1} that *exactly* matches the mysterious emission line. This suggests that the -243.8 km s^{-1} emission line is in fact a "ghost" spectrum in the GBT data. We attempted to remove the ghost by subtracting a scaled and shifted version of the datacube from itself. The "before" and "after" images of the GBT data (averaged in Galactic longitude) are shown in Figure 3.4; the comparison indicates that the removal of the line was successful, leaving no significant residual behind. From this point forward we use the ghost-subtracted datacube for our analysis.

We propose that the ghost in our GBT data can be accounted for by a sideband with constant offset frequency on a local oscillator used in the frequency conversion process that was not filtered out properly. This would cause a reproduction of the input spectrum at a much lower amplitude and at the offset frequency, in this case $\sim$1.14 MHz, corresponding to 240 km s^{-1} at 21 cm. It is possible that this ghost is present in other GBT H I data and we suggest that other GBT observers watch out for it.

3.2.4 GBT Survey Results

Figures 3.5 and 3.6 show our final, smoothed GBT datacube. An "RMS map" that contains a robust measure of the RMS noise for each position was also created (not shown). To pull out real features the data were σ-filtered so that only pixels in the datacube that were above $3\times$ the RMS noise (for their respective position) were used to make the figures.

The column density of the MS gas ($-502 < V_{\mathrm{LSR}} < -266$ km s^{-1}) is shown in Figure 3.5a. Contours of the end of the "classical" MS from the Leiden-Argentine-Bonn (LAB) H I all-sky survey (Kalberla et al. 2005) (white) and the MS–like gas in
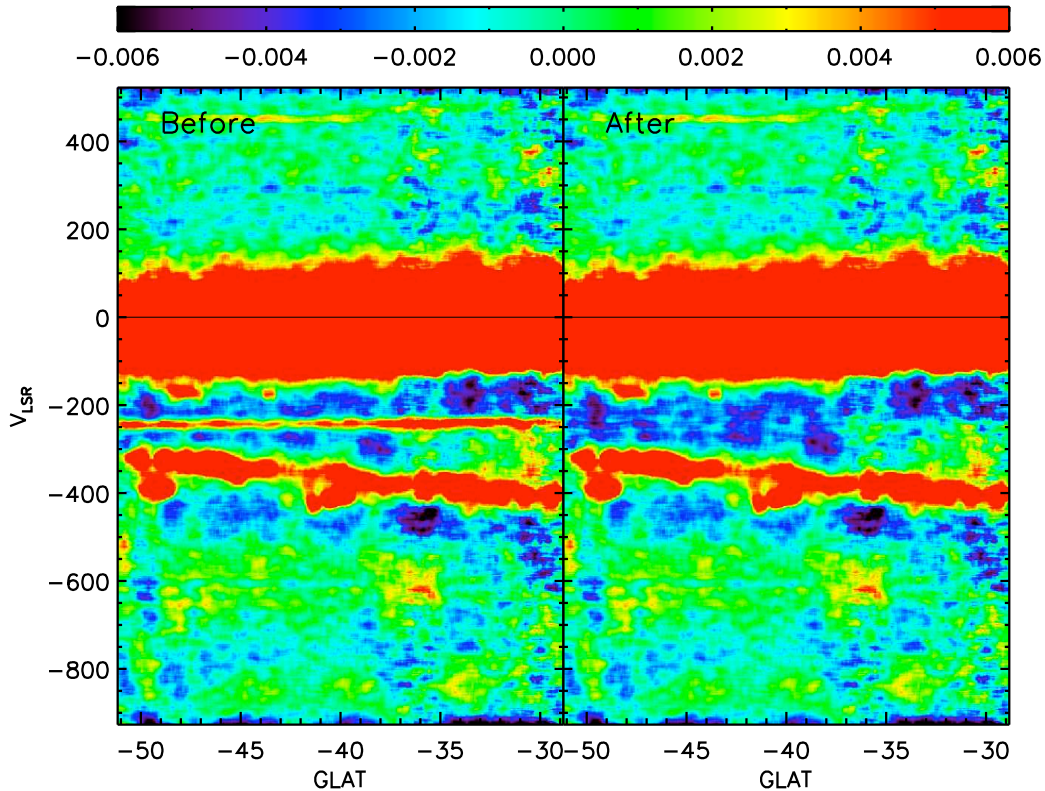
Fig. 3.4.— Intensities of the GBT data, averaged in Galactic longitude, in units of K. The left panel shows the data before removal of the -243.8 km s^{-1} "ghost" emission line, and the right panel shows the data after the ghost line is removed by subtraction of a scaled and shifted version of the datacube from itself. The unsmoothed datacube was used for the figure and the final V_{LSR}–b images were boxcar smoothed with a 20×20 filter to enhance fainter features.

the southern edge of the BT04 survey (gray) reveal the $\sim10°$ gap between the two that is filled by our GBT survey (mostly on the eastern part). There is nearly-continuous MS emission across our survey at $l \approx 93°$ and $l \approx 100°$ that bridges the gap between the "classical MS" and the BT04 survey for the eastern ($l \approx 100°$) portion of the MS. The northwestern region of our survey is filled with cloudlets at MS velocities and suggests that the western portion is also continuous across the gap. Figure 3.5b shows the velocity map for the MS gas. The gas at $l \approx 100°$ is at slightly lower velocity
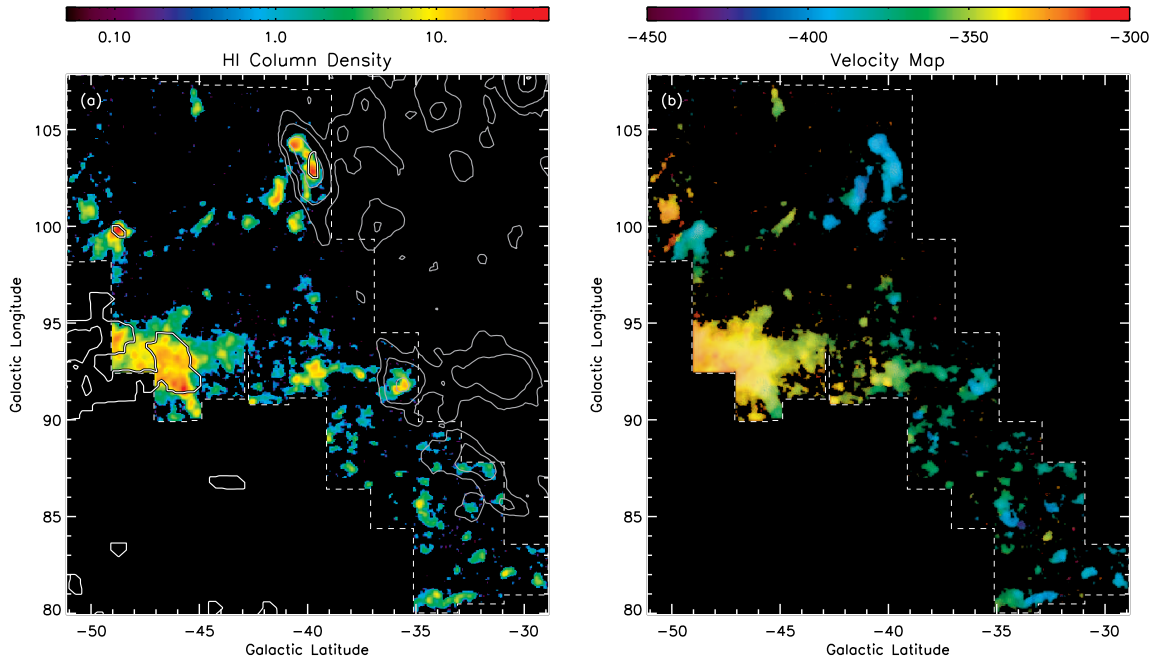
Fig. 3.5.— (*a*) H I column density, N_{HI}, (in units of 10^{18} atoms cm^{-2}) of the MS gas $(-502 < V_{\mathrm{LSR}} < -266$ km s$^{-1})$ after 3σ filtering of the GBT datacube. The end of the "classical" MS from the LAB data is shown in white contours (at 1 and 5×10^{19} atoms cm^{-2}), while gray contours show the MS–like gas in the southern edge of the BT04 survey (at 0.2, 1, and 5×10^{18} atoms cm^{-2}). There is nearly-continuous MS emission across our survey at $l \approx 93°$ and $l \approx 100°$. This bridges the gap between the "classical MS" and the BT04 survey for the eastern part of the MS (see §3.3.2). The northwestern region of our survey is filled with MS cloudlets and suggests that the western part of the MS is also continuous across the gap. (*b*) First-moment map for the data in (*a*). Hue indicates the flux-weighted velocity (V_{LSR} in km s^{-1} as indicated by the colorbar); intensity indicates N_{HI}. The velocity of the $l \approx 100°$ gas is $\sim$70 km s^{-1} lower than the gas at $l \approx 93°$. A dashed line demarcates the boundary of our survey. The figures have been oriented so that they are aligned with the other MS figures (e.g., Figs. 3.7 and 3.9).

(more negative) than the gas at $l \approx 93°$. Figure 3.6a shows the integrated intensity of the datacube along b and Figure 3.6b the integrated intensity along l. The velocity gradient of the MS with b is clearly apparent (since the MS nearly follows a constant line of Galactic longitude at this location). Some of the $l \approx 100°$ cloudlets can be
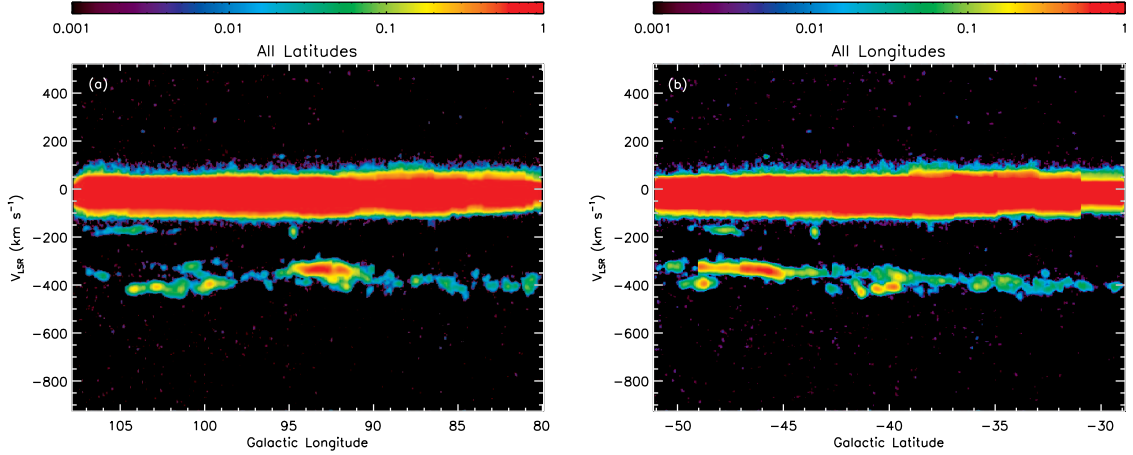
Fig. 3.6.— (*a*) Integrated intensity of the datacube along b (in units of K deg) after σ-filtering. The velocity of the $l \approx 100°$ gas ($V_{\mathrm{LSR}} \approx -406$ km s^{-1}) is $\sim$70 km s^{-1} lower than the gas at $l \approx 93°$ ($V_{\mathrm{LSR}} \approx -337$ km s^{-1}). (*b*) Integrated intensity of the datacube along l (in units of K deg) after σ-filtering. The velocity gradient of the MS with b is clearly apparent (since b is nearly parallel with the MS at this location). Some of the $l \approx 100°$ cloudlets can be seen slightly below the main linear trend of MS gas at $b \approx -49°$ and $-40°$.

seen slightly below the main linear trend of MS gas at $b \approx -49°$ and $-40°$.

In summary, our dataset shows that the MS is continuous across the gap between the "classical MS" and the BT04 survey. Therefore, the MS is much longer than previously recognized. In the next section we combine our data with other HI datasets in order to obtain a complete picture of the tip of the MS and to determine the full extent and distribution of the MS on the sky and in velocity.

3.3 The Combined Magellanic Stream Tip Datacube

In order to gain a clear picture of the entire tip of the MS we combined our GBT datacube with (1) the S08 Arecibo datacube, (2) a part of the Brüns et al. (2005,

hereafter Br05) Parkes datacube, and (3) the BT04 Westerbork datacube.

3.3.1 Combining the GBT, Arecibo, Parkes, and Westerbork Datacubes

Our combined "MS–tip" datacube is on a Cartesian grid on the MS coordinate system of Nidever et al. (2008)[2] with an angular step size of $3'$, a velocity step of 1.5 km s^{-1}, and a velocity range of $-548.5 \leq V_{\mathrm{LSR}} \leq -100.0$ km s^{-1}. A cubic spline was used to interpolate the datacubes onto the new velocity scale and the IDL function TRIGRID was used to regrid the datacube spatially one velocity channel at a time. Each dataset was regridded onto the new MS–tip grid separately before all datasets were combined.

GBT Data: The raw GBT data have an angular resolution of $9.2'$, angular sampling of $3.5'$, and velocity spacing of 0.16 km s^{-1} (before binning). The original, velocity-binned, GBT data were gridded onto the new datacube, and then smoothed with a Gaussian (FWHM=15 km s^{-1}) in velocity and spatially (FWHM=$6'$). The average final RMS noise is 0.011 K.

Arecibo Data: The S08 Arecibo datacube is a combination of three observing programs with differing S/N. The original data have an angular resolution of $3.5'$, angular sampling of $1.8'$, and velocity spacing of 0.18 km s^{-1}, but after gridding have an angular spacing of $3'$ and velocity spacing of 1.47 km s^{-1} (after binning). We masked out regions of the datacube with missing or bad data, as well as regions with poor S/N that overlapped the GBT data (mainly in the northern part). After the Arecibo datacube was regridded onto our MS–tip datacube it was smoothed with a Gaussian

---

[2]Note that this coordinate system is different from the "Magellanic coordinate system" used by Wakker (2001) and Putman et al. (2003).

(FWHM=15 km s^{-1}) in velocity. The average final RMS noise is 0.012 K.

Parkes Data: The Br05 Parkes data have an angular resolution of 14.1$'$, angular sampling of $\sim$5$'$, velocity spacing of 0.82 km s^{-1}, and cover a velocity range of $-410 < V_{\mathrm{LSR}} < 380$ km s^{-1}, but after gridding have an angular step of 10$'$ with the same velocity spacing. After the Parkes datacube was regridded onto our MS–tip datacube it was smoothed with a Gaussian (FWHM=15 km s^{-1}) in velocity. The average final RMS noise is 0.032 K.

Westerbork Data: The BT04 Westerbork auto-correlation data have an angular resolution of $\sim$50$'$ (effective telescope beam), an angular sampling of 15$'$, and velocity spacing of 8.3 km s^{-1} (Hanning smoothed to give a spectral resolution of 16.6 km s^{-1}). The gridded datacube was resampled onto the Local Group Standard of Rest (LGSR) velocity system with a velocity range of $-535 \leq V_{\mathrm{LGSR}} \leq 95$ km s^{-1} (approximately $-700 < V_{\mathrm{LSR}} < -50$ km s^{-1}). After converting the velocities to V_{LSR}, we discovered that there was a systematic velocity offset between the Westerbork data and the GBT and Arecibo data where they overlapped. We used the LAB survey to determine the velocity offset in all positions that had emission detected in both the LAB and Westerbork data. The velocity offset changed systematically with position with an average offset of $\sim$30 km s^{-1}. The additive offset (i.e. $v_{\mathrm{correct}} = v_{\mathrm{Westerbork}} + v_{\mathrm{offset}}$) was well-fitted by

$$v_{\mathrm{offset}} = 58.24 + 0.1954\alpha - 0.00959\alpha^2 - 0.7435\delta$$

where α and δ are in degrees. We applied this velocity offset to the Westerbork data and converted to V_{LSR} before regridding onto our MS–tip datacube. Since M31 and M33 are very prominent in the Westerbork datacube and would "contaminate" our MS position-velocity diagrams, we blanked their emission from the datacube. The

average final RMS noise is 0.0012 K.

We used a rank order of decreasing priority as GBT:Arecibo:Parkes:Westerbork to select which data to use for regions where the datasets overlap. We created a "hi-res" datacube, where all four datasets have their original resolutions, and a "low-res" datacube, where the combined GBT/Arecibo/Parkes data were smoothed to a resolution of $50'$ before being combined with the Westerbork data. In the hi-res datacube the intensity of the emission in the Westerbork part is generally low (by $\sim 2\times$) due to beam dilution, which creates an artificial drop in emission/column density at the interface between the Westerbork and GBT/Arecibo data. The low-res datacube gives generally smoother images because the data are relatively homogeneous in angular resolution.

We have also identified five Compact or extended High Velocity Clouds (C/HVCs) from de Heij et al. (2002) (numbers 237, 304, 307, 391, 402 in their Table 1) that lie outside the area covered by the four datasets in our MS–tip datacube and might be associated with the MS because they match the MS in position and velocity. The C/HVCs were added into the combined MS–tip datacubes with the structural Hı parameters given by de Heij et al. Since the Leiden/Dwingeloo Hı Survey (LDS; Hartmann & Burton 1997) was used to identify these Hı clouds, they have an angular resolution of $36'$ and velocity resolution of ~ 1 km s^{-1}. Most of the CHVCs of Westmeier & Koribalski (2008), which they identified as being associated with the MS, also lie outside the area surveyed by the four datasets. However, structural parameters are not available for these CHVCs and therefore we are not able to add them to our MS–tip datacube but instead plot them as crosses in Figures 3.7–3.12.
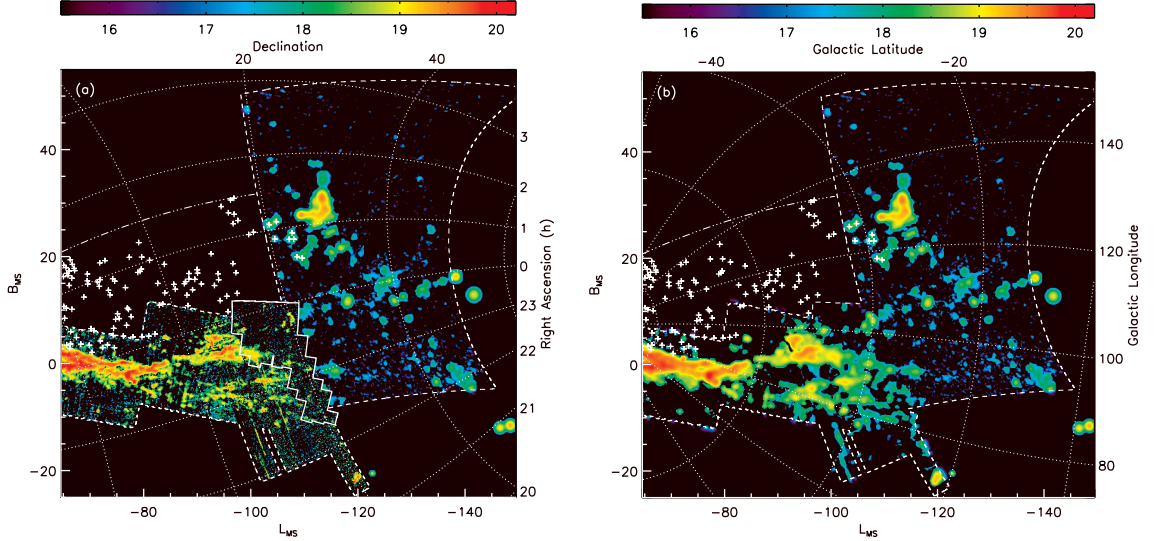
Fig. 3.7.— HI column density, N_{HI}, of the MS–tip combined datacube ($\log(N_{\mathrm{HI}})$ in units of atoms cm^{-2}) after an MS velocity selection and 3σ filtering have been applied. (a) The "hi-res" datacube with all four datasets (GBT, Arecibo, Parkes, and Westerbork) in their native resolutions. A celestial coordinate grid is overlaid. The boundary of our GBT survey is indicated by a solid white line. (b) The "low-res" datacube with all datasets at $50'$ resolution. A Galactic coordinate grid is overlaid. CHVCs from Westmeier & Koribalski (2008) that they associated with the MS are represented by white crosses. A dashed line indicates the boundary of the combined HI datacubes, and a dashed–dotted line delineates the eastern edge of the region studied by Westmeier & Koribalski (2008) ($0^{\mathrm{h}}00^{\mathrm{m}} \leq \alpha \leq 1^{\mathrm{h}}30^{\mathrm{m}}$ and $-30° \leq \delta \leq +25°$). The MS is seen here to be $\sim 40°$ longer than the "classical" MS (which ends at $L_{\mathrm{MS}} \approx -100°$), and now extends to the end of the Westerbork survey at $\delta \approx +50°$. The MS is very complex in this region with many forks and filaments — see text for details. Wright's Cloud is the backward "L"-shaped cloud at $(L_{\mathrm{MS}},B_{\mathrm{MS}}) \approx (-114°,+29°)$.

3.3.2 MS Tip Results

The HI column density map of the hi-res/low-res data can be seen in Figure 3.7 after an MS velocity selection (removing the well-separated local Galactic and intermediate velocity gas – see Fig. 3.10a) and 3σ filter have been applied. With the addition of the GBT and Arecibo data it is now clear that the entire "classical" MS (which ends near $L_{\mathrm{MS}} \approx -100°$) *is continuous* with the emission identified by BT04
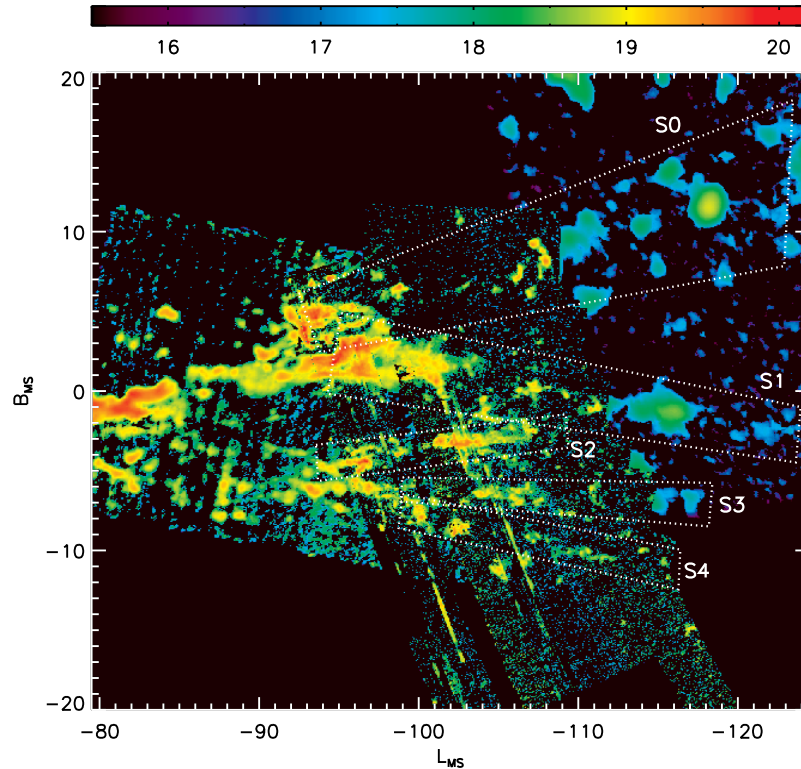
Fig. 3.8.— Close-up of Fig. 3.7a showing the various MS filaments. S1–S4 were defined in S08 and we extend them slightly with the addition of the BT04 data. We define the new eastern–most filament as S0; which splits with S1 near $L_{MS} \approx -95°$. The continuity of S0 as a filament of cloudlets is even clearer in Fig. 3.5.

as an extension of the MS (starting at $\delta = +20°$). The MS is at least $\sim 140°$ long and thus is $\sim 40°$ longer than previously known with certainty. The entire MS system — including the Leading Arm — is therefore $\sim 200°$ long. The MS extends to the limit of the MS–tip datacube (the Westerbork data) at $\delta \approx +50°$ and therefore is plausibly even longer than shown here. In fact, there is even one CHVC from de Heij et al. (2002) (number 424) that is consistent with being an extension of a filament on the eastern side of the MS at $L_{MS} \approx -163°$ (see Fig. 3.11 below).

The H I data of the MS–tip (Fig. 3.7) show a complex richness of patterns that look like forks and multiple filaments. The MS splits and diverges into two filaments

near $L_{\mathrm{MS}} \approx -80°$, which were already visible in previous data (e.g., Putman et al. 2003), but there are more forks farther along the Stream. Stanimirović et al. (2008) noted that the western region of the MS–tip separates into four thin filaments that they named S1–S4. Figure 3.8 is a close-up of Figure 3.7a that shows the filamentary structure in more detail. The four S08 filaments are indicated and extended slightly now that the BT04 survey data are included. S3 and S4 appear to run off the edge of the survey coverage while S1 and S2 are likely converging or overlapping for $L_{\mathrm{MS}} < -108°$.

A new filament of the MS (on the eastern side) is visible in our data that separates from S1 near $L_{\mathrm{MS}} \approx -95°$. Following the S08 nomenclature we call this filament S0. It is made up of many cloudlets, especially right after it separates from S1, but the continuity of S0 is clear in our GBT data (Fig. 3.5). As can be seen in Figure 3.7, S0 extends all way to the end of the coverage area near $L_{\mathrm{MS}} \approx -140°$. It deviates from the equator of the MS coordinate system and extends diagonally at an angle of $\sim 14.6°$ (slope of ~ 0.26). The S0 filament also follows a great circle with a north pole of $(l,b)=(205.20°,-15.40°)$ (Fig. 3.11; black–white dashed line) which is $\sim 18°$ from the north pole of the MS coordinate system $(l,b)=(188.5°,-7.5°)$. The western portion of the MS, which is probably a combination of S1, S2, and possibly S3[3], also extends to the end of the coverage area near $L_{\mathrm{MS}} \approx -140°$. More data are needed in the west and north to track the MS filaments further.

Figure 3.9 shows the velocity map of the low-res datacube with the Westmeier & Koribalski (2008) CHVCs plotted as colored crosses. The strong velocity gradient (~ 6 km s^{-1} deg^{-1}) with L_{MS} is apparent from the color coding. Figure 3.10 shows various V_{LSR}–L_{MS} position-velocity diagrams of the MS–tip low-res datacube. Figure 3.10a shows the total intensity of the entire datacube integrated in B_{MS}. The strong

---

[3]S4 runs off the coverage near $(L_{\mathrm{MS}},B_{\mathrm{MS}})=(-116°,-11°)$.
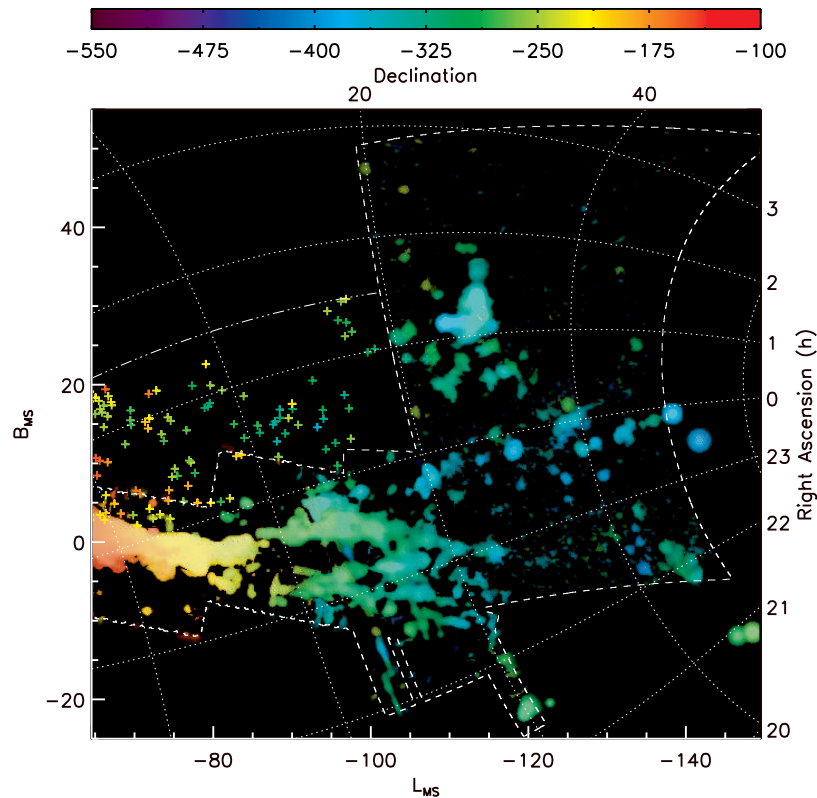
Fig. 3.9.— Velocity map of the $50'$–smoothed MS tip datacube. Hue indicates the flux weighted velocity (V_{LSR} in km s^{-1} as indicated in the colorbar) and intensity indicates N_{HI}. The crosses are CHVCs from Westmeier & Koribalski (2008). The velocity gradient along the MS is clear from the color coding.

velocity gradient with L_{MS} is again apparent, and so is a velocity inflection near $L_{\mathrm{MS}} \approx -120°$ where the velocity of the MS levels off and then starts to increase. This is the first evidence of a leveling-off of the MS velocity.

Figure 3.10b is a V_{LSR}–L_{MS} diagram similar to Figure 3.10a, but only for the western portion of the datacube ($B_{\mathrm{MS}} < 0°$) showing the velocity behavior of the S2–S4 filaments and part of S1. Most of the gas follows the velocity inflection (and the velocity fiducial line) including the low column density gas at $-132 < L_{\mathrm{MS}} < -117°$. There is a cloud at $(L_{\mathrm{MS}}, V_{\mathrm{LSR}}) \approx (-135°, -480$ km s$^{-1})$ that is consistent with

a near-linear extrapolation of the MS, and that might indicate that not the entire MS participates in the velocity inflection. The clouds at $(L_{\mathrm{MS}},V_{\mathrm{LSR}})\approx(-120°,-320$ km s^{-1}), above the main MS in the figure, are in the far western part of the datacube at $B_{\mathrm{MS}}\approx -20°$ and are not part of the main MS filaments (S0–S4).

A V_{LSR}–L_{MS} diagram of the central portion of the datacube ($0° < B_{\mathrm{MS}} < +15°$) including filament S0 (and parts of S1) is shown in Figure 3.10c. The velocity levels out and then increases, but not as quickly as for the western porton of the MS. The velocity scatter for the eastern portion is larger than for the western. There are two clouds near $(L_{\mathrm{MS}},V_{\mathrm{GSR}})\approx(-140°,-450$ km s^{-1}) that might not participate in the velocity inflection but continue to more negative velocities. Figure 3.11 extends the L_{MS} range of Figure 3.10c to include CHVC 424 from de Heij et al. (2002) which appears to be an extension of the S0 filament at $L_{\mathrm{MS}}\approx -163°$. This cloud, as well as the clouds at $L_{\mathrm{MS}}\approx -140°$, are consistent with a possible shallower velocity inflection for the S0 filament than for the rest of the MS.

Finally, Figure 3.10d shows the part of the datacube to the east of the S0 filament ($B_{\mathrm{MS}} > +15°$) which includes Wright's Cloud (Wright 1979) at $L_{\mathrm{MS}} \approx -114°$ and most of the Westmeier & Koribalski (2008) CHVCs. The clouds around Wright's Cloud appear to be an extension of the Westmeier & Koribalski (2008) CHVCs and they all generally follow the MS velocity trend. Some authors (Wright 1979, BT04) have previously considered the possibility that Wright's Cloud might be associated with the MS. The velocity agreement of the MS and Wright's Cloud in Figures 3.10a and d makes this association likely. We discuss this possibility further in §3.5.

We can calculate the mass of the newly-found part of the MS-tip by assuming various orbits or distances. In order to remove all of the HI emission that was previously observed (i.e., the "classical" MS) we subtract the Br05 Parkes data from
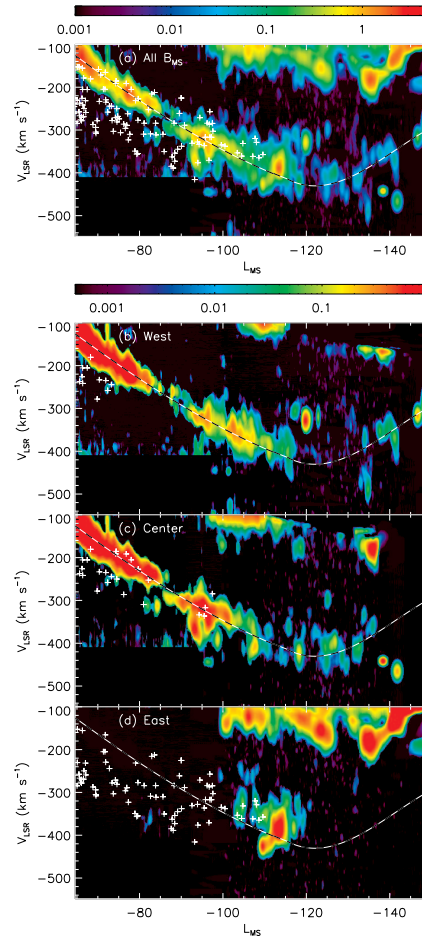
Fig. 3.10.— (*a*) Total intensity of the 50′–smoothed low-res MS tip datacube integrated along B_{MS} (in units of K deg on a logarithmic scale). There is a velocity inflection near $L_{\mathrm{MS}} \approx -120°$ where the velocity flattens out and begins to increase. White crosses are the CHVCs from Westmeier & Koribalski (2008), and a dashed fiducial line (same in all panels) shows the proposed general velocity trend. Wright's Cloud is the red blob at $(L_{\mathrm{MS}}, V_{\mathrm{LSR}}) \approx (-114°, -380 \text{ km s}^{-1})$. (*b*) Same as (*a*) but only for the western portion of the MS–tip datacube ($B_{\mathrm{MS}} < 0°$) showing the S2–S4 filaments and part of S1. (*c*) Same as (*a*) but only for the central portion of the MS–tip datacube ($0° < B_{\mathrm{MS}} < +15°$) showing filament S0 (and parts of S1). Two of the de Heij et al. (2002) CHVCs are at $L_{\mathrm{MS}} \approx -140°$. (*d*) Same as (*a*) but only for the eastern portion of the MS–tip datacube ($B_{\mathrm{MS}} > +15°$) showing the clouds around Wright's Cloud and many of the Westmeier & Koribalski (2008) CHVCs. The sudden cutoff in velocity at $V_{\mathrm{LSR}} = -410 \text{ km s}^{-1}$ for $L_{\mathrm{MS}} > -92°$ in all panels is due to the velocity limit of the Br05 Parkes datacube.
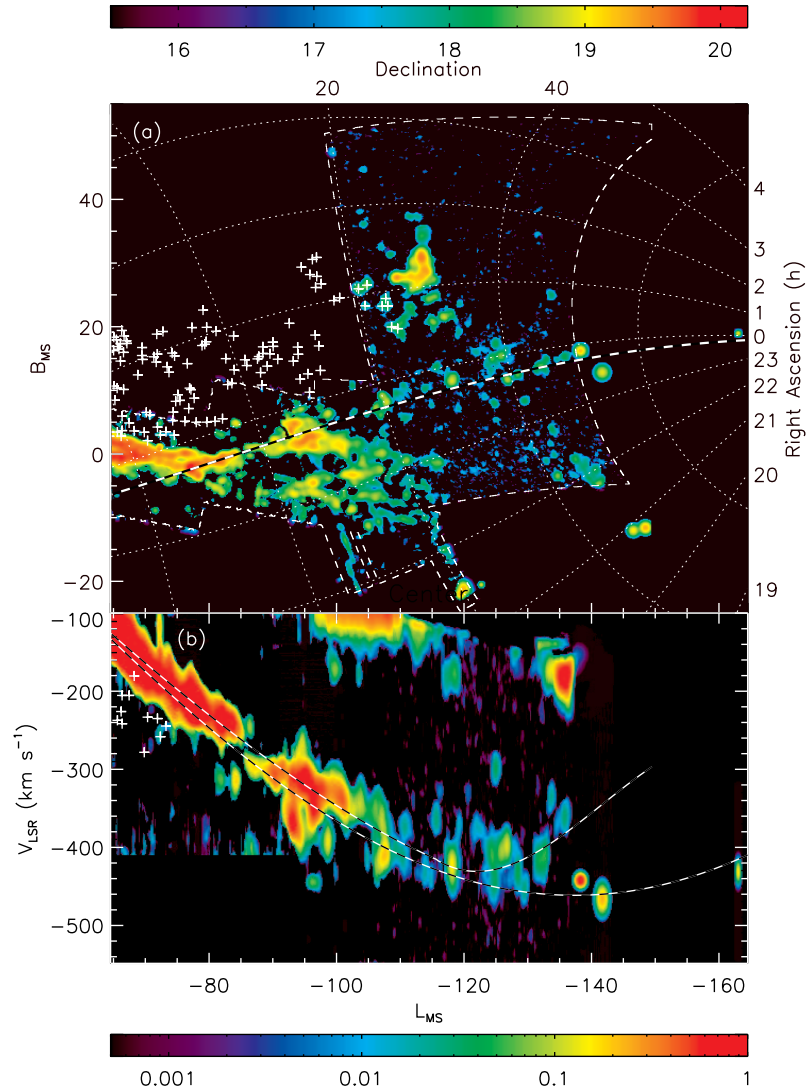
Fig. 3.11.— (*a*) Same as Fig. 3.7b but with an extended L_{MS} range and showing CHVC 424 from de Heij et al. (2002) at $L_{MS} \approx -163°$ that might belong to an extension of the S0 filament of the MS. The black–white dashed line indicates the great circle with north pole of $(l,b)=(205.20°,-15.40°)$ that best fits the S0 filament of the MS and which also passes close to CHVC 424. The great circle also fits the eastern portion of the MS (S0+S1 before they split) all the way to $L_{MS} \approx -80°$. (*b*) A similarly extended version of Fig. 3.10c. A second V_{LSR}–L_{MS} fiducial is shown that fits CHVC 424 .

our combined MS–tip column density map. For distances of the gas we use the K1 and GN96 orbits from Besla et al. (2007) and a uniform 120 kpc for all gas. The

derived masses, including Wright's Cloud, are then 6.3×10^8 M$_\odot$, 4.1×10^7 M$_\odot$, and 2.8×10^7 M$_\odot$ for K1, GN96 and 120 kpc respectively. Neglecting Wright's Cloud gives masses of 5.8×10^8 M$_\odot$, 3.0×10^7 M$_\odot$, and 1.8×10^7 M$_\odot$. The K1 masses are by far the largest because the high-velocity orbit reaches large distances (> 1 Mpc) for $L_{MS} < -125°$. Due to ram pressure, the unbound MS gas will slow down, lose angular momentum, and fall in its orbit around the MW. Therefore, the actual MS distances are likely to be smaller than those from the K1 orbit (which is based on the most accurate proper motion measurements), and a more realistic (and conservative) mass estimate is likely to be closer to $\sim 5 \times 10^7$ M$_\odot$. Since the mass of the "classical" MS is $\sim 5 \times 10^8$ M$_\odot$ (Br05), the mass of the newly-found $\sim40°$ of gas at the MS–tip corresponds to a $\sim10\%$ increase in the total mass of the MS.

3.4   The Entire Magellanic Stream

We combined the MS–tip datacube with the LAB MS Gaussians from Nidever et al. (2008) to create images of all the Magellanic gas. The column density, N_{HI}, of the entire $\sim200°$ MS+LAF system is shown in Figure 3.12a. The separation of the two main MS filaments at $L_{MS} < -80°$ is clearly visible. The very low column density of the MS–tip ($L_{MS} < -100°$) made it difficult to detect in previous surveys.

Figure 3.12b shows the V_{LSR}–L_{MS} position-velocity diagram (integrated in B_{MS} for $-40° \leq B_{MS} \leq +40°$; in units of K deg) for the entire MS. For most of the length of the MS ($-110° < L_{MS} < -30°$) its velocity follows a fairly linear gradient; this changes, however, at the very tip where the velocity levels out and starts to increase.

We can now see the Westmeier & Koribalski (2008) CHVCs (light blue crosses in Fig. 3.12a) and the cloudlets at the far eastern part of the MS–tip datacube (near Wright's Cloud) in the context of the entire MS. The Westmeier & Koribalski CHVCs
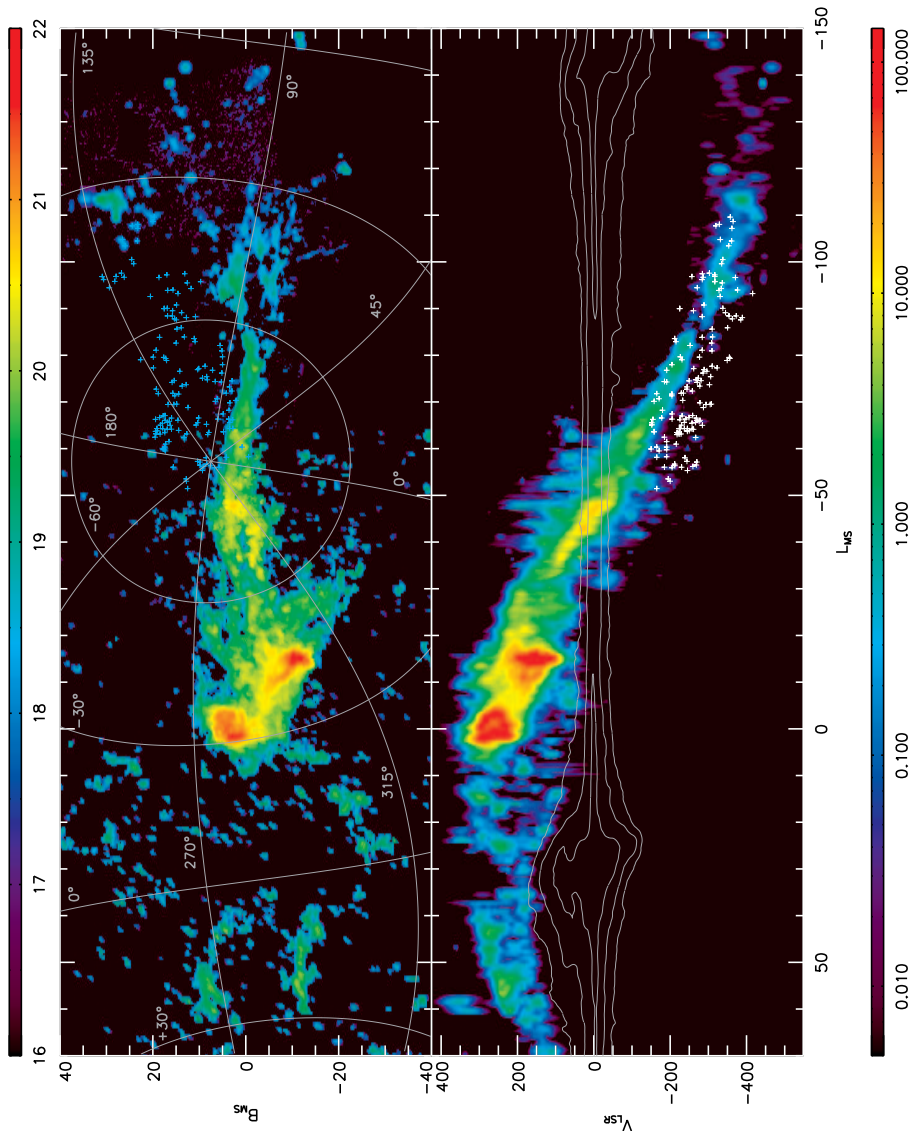
Fig. 3.12.— Combined data for all the Magellanic H I gas. (*Top*) H I column density ($\log(N_{\rm HI})$ in units of cm^{-2}). The MS–tip datacube is used for $L_{\rm MS} \leq -65°$ and the LAB MS Gaussians from Nidever et al. (2008) are used for the rest. The CHVCs from Westmeier & Koribalski (2008) are shown as light-blue crosses (not color-coded). (*Bottom*) Total intensity of the Magellanic H I integrated along $B_{\rm MS}$ (in units of K deg). The MS Gaussians are shown with their true width and not just at their center as in Nidever et al. (2008). The CHVCs from Westmeier & Koribalski (2008) are shown as white crosses. The Galactic H I emission is shown as gray contours (at 10, 100, and 1000 K deg).
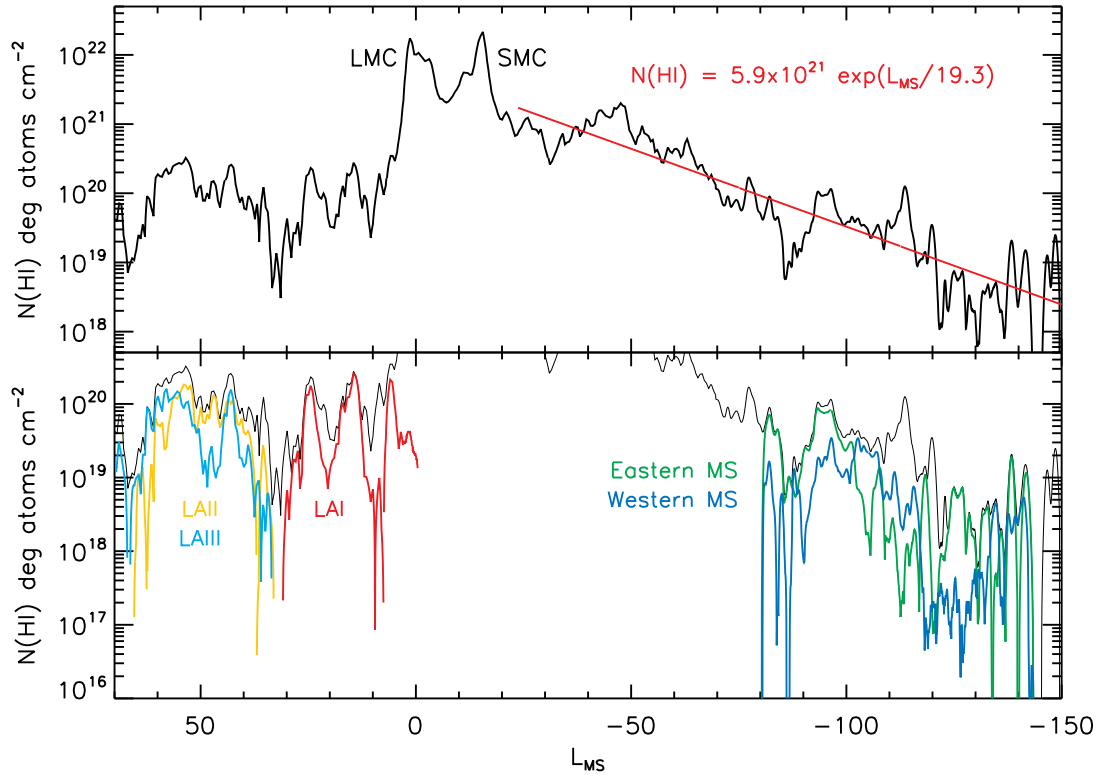
Fig. 3.13.— Total "cross–sectional" column density, N_{HI}, (integrated in B_{MS}) of all the Magellanic HI gas (same as Fig. 3.12) as a function of L_{MS} (in units of deg atoms cm^{-2}). There is a strong column density gradient along the MS which is well fit by $N_{HI} = 5.9 \times 10^{21} \exp(L_{MS}/19.3°)$ cm^{-2}. The Leading Arm, on the other hand, has a fairly constant column density along its $\sim 60°$ span. The lower panel shows various individual components of the MS and LAF: LAI–III, and the eastern (S0+S1) and western (S2–S4) portions of the MS.

appear to be an extension of the cloudlets near $(L_{MS}, B_{MS}) \approx (-45°, +15°)$, just above the main body of the MS, which themselves are probably an extension of the HI filament emanating diagonally from the center of the Magellanic Intercloud Region (ICR) at $(L_{MS}, B_{MS}) \approx (-9°, -2°)$. It appears as though all of these cloudlets are connected into one large filament that is parallel, but above in B_{MS}, the main body of the MS. This "parallel filament" has lower column density and is much clumpier than the main MS, and does not appear to continue past $L_{MS} \approx -120°$.

Figure 3.13 shows the column density integrated along B_{MS} for the entire MS+LAF system. There is a strong column density gradient along the MS as has been previously noted (Mathewson et al. 1974; Putman et al. 2003); this gradient is well fitted by $N_{HI} = 5.9 \times 10^{21} \exp(L_{MS}/19.3°)$ cm^{-2}. The Leading Arm, on the other hand, has a fairly constant column density along its $\sim 60°$ span. The lower panel shows various individual components of the MS and LAF: LA I–III, and the eastern (S0+S1) and western (S2–S4) portions of the MS.

3.5   Discussion

Besla et al. (2007) presented new orbits for the MCs that place them much farther from the MW in the past than previously thought. These models further suggest that it would be difficult for ram pressure or tidal forces to create a long MS since these forces require the MCs to be fairly close to the MW for quite some time to be effective, and therefore star formation is probably required to help the gas escape the MCs when at large distances from the MW. The suspected role of star formation in the formation of the MS by Besla et al. is in agreement with the independent observational findings of Nidever et al. (2008). Even so, Mastropietro (2009) was able to produce a 120°– long stream using ram pressure and the new, higher-velocity MC orbits. However, as shown in this paper, the MS is 40° longer than previously thought — and probably even longer. It is unclear from current simulations if ram pressure and/or tidal forces alone can account for a stream of this length. Thus, our finding of a longer MS offers an additional challenge to tidal and ram pressure models. Future surveys of the MS– tip will provide even more stringent requirements on MS models and possibly further constrain the MC orbits.

The deviation of the eastern portion of the MS from the equator of the MS co-

ordinate system was already seen by Putman et al. (2003), but the very coherent deviation of the new S0 filament for more than $\sim 45°$ has not been seen until now. The tidal MS models by Connors et al. (2006) have already reproduced this deviation fairly well (as well as multiple filaments), while Mastropietro et al. (2005) shows a deviation in the opposite direction and Mastropietro (2009) shows only a small deviation (both only with one filament). It is not entirely clear why the deviation of the S0 filament occurs.

We investigated the K1 and GN96 LMC orbits from Besla et al. (2007) and found that the velocity inflection does not correspond to any physically identifiable part of the orbit (unlike, e.g., $V_{\mathrm{GSR}} = 0$ km s^{-1} which corresponds to peri- or apo-galacticon). It is just the point in the orbit at which the satellite is approaching the observer with the maximum speed, and is then dependent on the position of the observer with respect to the orbit. However, at a given observing position, the position of the velocity inflection (and the maximum approach velocity) is sensitive to the initial space velocity of the orbit. This newly found, distinct feature in the otherwise remarkably linear velocity structure of the MS should provide an additional constraint for MS simulations.

We have shown that the velocity of Wright's Cloud is in close agreement with the velocity of the MS gas in the same region of the sky. This might be an indication that Wright's Cloud is part of the MS. Another interpretation is that Wright's Cloud is not gas that escaped from the MCs, but rather is part of the "Magellanic Group" of galaxies proposed by D'Onghia & Lake (2008) to have fallen into the MW together. Since the group is proposed to be quite extended, some objects will fall in before others, but the whole of the system will enter the MW with similar space velocities. Wright's Cloud, therefore, could be an HI cloud (primordial or previously stripped

from another galaxy) that is falling into the MW behind the MCs. Wright's Cloud should have a similar space velocity to the MCs (since they are part of the same group) and will experience similar tidal and ram pressure forces to the MS that should give rise to a radial velocity very similar to that of the MS.

Nidever et al. (2008) discovered that at the head of the Stream the two filaments of the MS have sinusoidal velocity patterns. One possible explanation is that this is an imprint of the LMC rotation curve. With this hypothesis Nidever et al. were able to measure the drift rate of the MS gas away from the LMC to be $\sim$49 km s^{-1} and the age of the $\sim$100°–long MS (at 50 kpc) to be $\sim$1.7 Gyr. Now that the MS is $\sim$40° longer the estimate of the age of the MS must also increase. Using the same drift rate the new age estimate for the MS is at least $\sim$2.50 Gyr. The heliocentric distances of any Magellanic orbit increase significantly at the tail of the MS which makes the MS older via two effects. A larger MS distance increases the linear length of the MS and probably decreases the drift rate (since the ram pressure and tidal forces are weaker at larger distances) both of which increase the age. Therefore the MS is likely to be even older than $\sim$2.50 Gyr.

The new MS age estimate of $\sim$2.50 Gyr closely coincides with "bursts" of star formation in the integrated star formation histories of the LMC (Harris & Zaritsky 2004) and SMC (Smecker-Hane et al. 2002) at $\sim$2–2.5 Gyr ago; these bursts are suggestive of an interaction between the MCs at that time. Also, the LMC globular cluster age–gap between 3 and 13 Gyr (e.g., Da Costa 1991; Geisler et al. 1997; Rich et al. 2001; Piatti et al. 2002) indicates an onset of star formation in the LMC around $\sim$3 Gyr ago, although such an age–gap is not seen in the SMC clusters (Da Costa 1991). Finally, the orbits by Besla et al. (2007) indicate possible encounters of the MCs with each other around 0.2, 3 and 6 Gyr ago. Therefore, a plausible scenario

is that the MCs had a close encounter at $\sim$2.5–3 Gyr ago that triggered a burst of star formation in the LMC and started the self-propagating SGS blowout of the Magellanic Stream and Leading Arm.

One point that the ram pressure simulations, tidal simulations, and new LMC orbits (Besla et al. 2007) agree on is that the distance from the MW at the MS–tip (beyond $\sim$110°) increases quite rapidly (almost exponentially). Therefore, the new length of the MS implies that the gas at the MS–tip is much farther away than the "classical" MS. The MS gas we are observing at $L_{MS} \approx 130°$ is likely at a distance on the order of $\sim$200 kpc and possibly even larger. This means that the MS spans a larger range of MW distances than previously thought which makes the MS an even more useful probe for constraining the total MW mass and the MW potential at large distances.

3.6 Summary

We conducted an $\sim$200 deg^2 21–cm survey of the MS–tip with the Green Bank Telescope that bridges the gap between the "classical" MS and the MS-like emission reported by BT04. Our survey, in combination with the Arecibo survey by S08, shows that the MS gas is in fact continuous across this gap. We made a combined MS–tip datacube incorporating our GBT datacube, the S08 Arecibo survey, the BT04 Westerbork data, and the Br05 Parkes data. This MS–tip datacube allows us to draw the following conclusions:

1. The MS is $\sim$140° long, approximately 40° longer than previously thought. The MS extends to the edge of the datacube, implying that the Stream may be even longer. Moreover, there is one CHVC from de Heij et al. (2002) at $L_{MS}\approx$

$-163°$ that is consistent with an extrapolation of the eastern-most filament of the MS in position and velocity.

2. The tip of the MS is composed of a multitude of forks and filaments. S08 previously identified filaments S1–S4 in the western region, and we identify a new filament, S0, on the eastern side. This filament splits from S1 near $(L_{\mathrm{MS}}, B_{\mathrm{MS}}) \approx (-95°, +3°)$ and deviates from the equator of the MS coordinate system for more than $\sim 45°$ until it reaches the end of the datacube.

3. There is an MS velocity inflection near $L_{\mathrm{MS}} \approx -120°$ where the MS velocity levels out and starts to increase.

4. The mass of the newly extended $\sim 40°$ at the MS–tip is $\sim 5 \times 10^7$ $M_\odot$ (but depends on the exact distances that are assumed) and increases the total mass of the MS by $\sim 10\%$.

Five C/HVCs from de Heij et al. (2002) (numbers 237, 304, 307, 391, 402 in their Table 1) match the MS in position and velocity and, therefore, might be associated with the MS. Wright's Cloud also matches the velocity of the MS and is nearby in position making an associated with the MS possible. The CHVCs that Westmeier & Koribalski (2008) associated with the MS follow the MS velocity trend in our V_{LSR}–L_{MS} diagrams and might belong to a "parallel filament" next to the MS that stretches from the head of the MS to cloudlets near Wright's Cloud.

The total column density (integrated in B_{MS}) along the MS drops markedly and follows an exponential decline with the angular distance from the LMC well-fitted by $N_{\mathrm{HI}} = 5.9 \times 10^{21} \exp(L_{\mathrm{MS}}/19.3°)$ cm^{-2}.

An increased length of the MS also increases the age estimate of the MS. Using the velocity sinusoidal pattern of the LMC filament of the MS as a chronometer (as was

previously done by Nidever et al. 2008), we estimate that the age of the $\sim$140°–long MS is $\sim$2.5 Gyr. This timescale coincides with bursts of star formation in both the LMC and SMC as well as a possible close encounter between the MCs that could have triggered the new era of star formation and the formation of the MS via SGS blowout.

These new observational characteristics of the MS should offer further constraints on MS simulations and provide the means to elucidate more accurate dynamical and structural information for the Magellanic System and its interaction with the MW.

We encourage further HI observations of the MS–tip to track the MS to ever greater lengths until its actual end is found.

Chapter 4

Summary and Future Directions

4.1 Summary

We have performed a detailed HI study of the Magellanic Stream using a Gaussian decomposition of the LAB HI all-sky survey, our 200 deg^2 HI GBT survey, and other HI data of the Magellanic Clouds and Stream. Our study has revealed new insights into the origin, structure and length of the Magellanic Stream and its relation to the Magellanic Clouds. The results of our study are summarized here.

4.1.1 The Origin of the Magellanic Stream

Contrary to previous assertions that the MS originates in the SMC and Bridge, we have shown conclusive evidence that one of the filaments of the MS and LA I originate in the LMC. Furthermore, we have identified the specific location from which the MS eminates – the SEHO region. The SEHO region is the perfect place for the MS to originate. It has a high concentration of gas and CO that helps produce prolific star formation. It is therefore also the site of many young clusters and supergiant shells.

In addition, the SEHO is on the leading edge of the LMC in a location where the ram pressure forces and the rotation of the LMC combine to create a very steep column density gradient. It is also at one end of the stellar bar which could be contributing to the "perfect storm" in this region. We encourage modelers to use an LMC origin for their MS simulations and not to exclude this possibility as has been done in the past (e.g., Gardiner & Noguchi 1996; Yoshizawa & Noguchi 2003; Connors et al. 2004, 2006)

4.1.2   The Blowout Model

We have shown that the high-resolution HI data reveal supergiant shells in the SEHO region blowing gas to high velocity and that are forming the beginning of the MS and LA I. Even though it was previously known that some young clusters in the LMC, such as 30 Doradus, are blowing out gas to high velocities, this is the first time that large-scale gas blowout from the LMC has been shown and has been linked to the formation of the MS. In fact, this is the first direct evidence of the formation mechanism of the MS. The very thin filamentary structure of both the LMC filament and LA I, and the fact that they can be traced back to very small regions in the LMC points directly to a localized formation mechanism such as SGS blowout and not a large, global mechanism such as ram pressure or tidal forces.

In Chapter 2 we laid out a new model for the formation of the MS, namely the "Blowout Model", that states that SGSs in the SEHO region of the LMC blow out HI gas to high velocity (at or close to the LMC escape velocity). Once the gas is far enough away from the LMC disk the global ram pressure and tidal forces take over to disperse the HI gas into the Leading Arm and trailing Magellanic Stream. Therefore, SGS blowout takes the role of gas removal from the MCs while the traditional

mechanisms take care of the gas dispersal.

In the blowout model the debate over ram pressure and tidal forces is less important. Actually, it is clear that both ram pressure and tidal forces are at work in the MCs and the MS. Tidal forces are required to create the Leading Arm and ram pressure is required to create the steep column density gradient at the leading edge of the LMC. The question is what is the relative strength of these two forces. This can be answered by varying the relevant parameters in the simulations (e.g., the density of the MW hot halo gas) until the observed properties of the LMC and MS are reproduced.

The blowout model solves the longstanding problem of why there are no stars in the MS since the SGS blowout only affects gas and not stars. Therefore, stars are not expected in the MS under this model even in the presence of tidal forces. The blowout model should also solve the problem that the Besla et al. (2007) first passage scenario poses for the ram pressure and tidal models since the large MW-centric distances of the MCs make these methods less effectual. SGS blowout can do the work of removing the HI gas from the LMC disk to where even weak ram pressure and tidal forces can take over for dispersal in the first passage scenario. In fact, the blowout model should fit all the currently known properties of the Magellanic system. A comparison of the three MS formation models is outlined in Table 4.1.

Table 4.1. Comparing MS Formation Mechanisms

	Tidal	Ram Pressure	Blowout
LMC Origin	X	$\checkmark$	$\checkmark$
Leading Arm	$\checkmark$	X	$\checkmark$
N_{HI} gradient	X	$\checkmark$	$\checkmark$
No Stars	X	$\checkmark$	$\checkmark$
First Passage	X	X	$\checkmark$
Long MS	X	X	$\checkmark$

4.1.3 The Length of the Magellanic Stream

As we discusssed in Chapter 3, our 200 deg^2 GBT survey in combination with other HI surveys shows that the MS is at least 140° long and possibly even longer. This extended MS could be another problem for the traditional MS formation mechanisms especially in the first passage scenario. As previously pointed out, all magellanic orbits have heliocentric (or MW-centric) distances that increase dramatically at the MS tip. This considerably weakens the ability of ram pressure and tidal forces to efficiently remove gas from the LMC. However, in the blowout model the SGSs can blow out gas from the LMC at any MW-distance, which will eventually get dispersed by the ram pressure and tidal forces.

4.1.4 The Age of the Magellanic Stream

The two filaments of the MS exhibit a striking sinusoidal pattern in velocity. This has not been previously observed or predicted. We hypothesize that the sinusoidal pattern in the LMC filament is an imprint of the LMC rotation curve. With this hypothesis we are able to measure the drift rate of the MS gas away from the LMC to be ∼49 km s^{-1}. Our estimate in Chapter 2 of the age of the ∼100°–long MS (at 50 kpc) was ∼1.7 Gyr. But with our discovery that the MS is at least 140° long this increases our estimate for the age of the MS to at least ∼2.50 Gyr. This new MS age estimate closely coincides with "bursts" of star formation in the integrated star formation histories of the LMC and SMC at ∼2–2.5 Gyr ago and the onset of LMC globular cluster formation after a gap from 3–13 Gyr ago. Additionally, the orbits by Besla et al. (2007) indicate possible encounters of the MCs with each other around

0.2, 3 and 6 Gyr ago. Therefore, a plausible scenario is that the MCs had a close encounter at ∼2.5–3 Gyr ago which triggered a burst of star formation in the LMC and started the self-propagating SGS blowout of the Magellanic Stream and Leading Arm.

4.2 Future Directions

There are a number of ongoing and planned projects related to the Magellanic Stream that I am working on. The MS projects aim to more fully understand the MS formation mechanism, the extent of SGS blowout in the LMC, the origin of the second MS filament, the true length of the Stream, and the interaction of the MS with the MW hot halo. Additionally, I am searching for young stars possibly being formed in the MS, and surveying the periphery of the Magellanic Clouds for evidence of a stellar component of the MS and stellar halos of the LMC and SMC. These stellar surveys will also allow me to gain a better understanding of the dynamics of the MCs and their stellar populations.

4.2.1 A Search for Young Stars in the Magellanic Stream

In the early 1990s, Irwin et al. (1990) discovered a new population of blue stars in the Magellanic Intercloud Region (ICR). Color magnitude diagrams (CMDs) showed a clear young, main-sequence and spectroscopy of a small sample of bright stars confirmed their identify as young, hot stars in the ICR. Most of the young blue stars are located close to the Small Magellanic Cloud (SMC) in the SMC eastern wing which has a high density of HI (the Magellanic Bridge, Muller et al. 2003), but blue stars at lower densities are spread across the entire ICR. Deep follow-up CCD observations (Grondin et al. 1990; Demers et al. 1991; Grondin et al. 1992; Demers

& Battinelli 1998; Battinelli & Demers 1998; Demers & Battinelli 1999) confirmed that many of the blue stars belong to young associations ($<$ 50 Myr old) either located in the SMC eastern wing or the western edge of the Large Magellanic Cloud (LMC). High-resolution spectroscopic observations (Hambly et al. 1994; Rolleston et al. 1999) confirmed the very young nature of the ICR B stars and showed that they are metal-poor.

We showed in Chapter 2 that one of the filaments of the bifurcated MS originates in the SEHO of the LMC and therefore also crosses the ICR. As can be seen in Figure 2.9, the LMC filament of the MS is distinguishable from the rest of the HI gas in the ICR by its high radial velocity (RV) due to the velocity sinusoidal pattern. Therefore, any young stars *born in* the MS should be identifiable by their RVs.

The goal of this project is to try to answer the question of whether any of the blue stars in the ICR are actually young stars born in the LMC filament of the MS. To date, no stars (young or old) have been detected in the MS (e.g., Philip 1976a,b; Recillas-Cruz 1982; Brück & Hawkins 1983; Kunkel et al. 1997; Guhathakurta & Reitzel 1998). Towards this end, we conducted a low-resolution spectroscopic survey with the SMARTS-1.5m and the RC-Spectrograph of 34 blue stars in the eastern ICR that are spatially coincident with the MS in order to use their RVs to associate them with the MS. We also obtained follow-up high S/N, high-resolution spectra of MS candidate stars with Magellan+MIKE in order to confirm their identity as young stars. We are still working on deriving reliable stellar parameters for these stars using synthetic spectral fitting and equivalent-width fitting to the high-resolution spectra. With the stellar parameters we can then calculate ages and distances to the stars which will allow us to associate them more definitively with the MS or other Magellanic structures. The initial results indicate that there are six moderately young

stars (as indicated by their $v \sin i$ and $T_{eff}/\log g$ values) with Magellanic RVs in our survey. Two of these stars have RVs that might associate them with the MS, while the other four are either associated with the LMC disk or the Magellanic Bridge/SMC eastern wing. We are hoping to finish up and publish this project soon.

4.2.2   Deep GBT MS Observations

One aspect of the Magellanic Stream that is not well understood is its interaction with the hot halo of the MW and how that shapes the evolution of the MS over time. I am collaborating with Lou Nigra and Snežana Stanimirović on a project to use deep GBT observations of the MS to investigate the interaction of the cool MS gas with the hot, diffuse halo gas of the Milky Way. This is part of Lou's thesis project at the University of Wisconsin. The HI velocity profiles of MS cloudlets and the low-density gas at their periphery will be compared to HI simulations in order to understand the interaction with the low-density halo gas. The GBT observations have already been obtained and Lou has reduced the data for the first region under investigation although the data for the second region shows some systematic baseline problems.

4.2.3   Galactic Australian SKA Pathfinder Spectral Line Survey

Australian radio telescopes (especially Parkes and ATCA) have been instrumental in our understanding of the Magellanic Clouds. The Australian Square Kilometer Array Pathfinder (ASKAP) is a next-generation radio interferometer comprised of 36 antennas (12m in diameter) with high dynamic range and a wide field-of-view. I am a collaborator on the Galactic Australian SKA Pathfinder Spectral Line Survey (GASKAP) proposal which was recently accepted by the ATNF. GASKAP is a 9000

hour high spectral resolution survey of HI in the Galactic plane, the Magellanic Clouds and the Magellanic Stream. The survey will cover the entire Magellanic System (for $\delta < +40°$) with a uniform high spatial and spectral resolution. I have volunteered to work on software to Gaussian decompose the HI profiles as I have done for the LAB survey, and, of course, work on the Magellanic Stream portion of the survey. ASKAP will start operation in 2013.

4.2.4 Comparison of HI MS Observations to Ram Pressure and Tidal Models

The Magellanic Stream literature is comprised mainly of observational and modeling papers with little comparison between the two and only in the most general terms. Therefore, I have been planning on making a detailed comparison of the HI observations of the Magellanic Stream with the ram pressure simulations by Mastropietro et al. and the Connors et al. tidal models. I have obtained the simulation data files and plan on making comparisons with column density on the sky, integrated position–velocity diagrams (including the velocity inflection), as well as looking at how the total column density integrated transverse to the MS varies along the Stream. The goal is to try to better understand the strengths and weaknesses of the MS formation models and identify features of the observed MS that remain to be modeled correctly. I am particularly interested in seeing if the velocity sinusoidal pattern at the head of the MS is reproduced in the simulations. From the figures in the literature the simulations do not seem to have the sinusoidal pattern.

4.2.5   The Origin of the Second Magellanic Stream Filament

One question left unanswerd in my work with the LAB data is the origin of the second filament of the MS. Since the publication of my findings in Nidever et al. (2008), I have used my Gaussian analysis program described in Chapter 2 to decompose the Br05 Hɪ datacube of the Magellanic Stream. This dataset has a resolution of $\sim$16$'$, more than two times higher than for the LAB survey, and a velocity resolution of 1 km s^{-1}. Therefore, this dataset is better suited than the LAB data for studying the spatial structure of the MS, especially in the ICR. Since the time of the initial analysis of the LAB data on the origin of the MS I have been trying to identify the origin of the second MS filament which gets "lost" in the Bridge gas in the ICR. One of the interesting features of the two MS filaments is that they have periodic spatial undulations and are composed (at least at the head of the MS) of clumps elongated in L_{MS} with sizes of $\sim$6.0$\times$1.5$°$. The column density maps of P03 show similarly aligned clumps of gas on the other (leading) side of the ICR near the Leading Arm. An extrapolation of the second MS filament through the SMC region connects it with these clumps. The periodic patterns in the two MS filaments mirror each other and when the spatial pattern of the LMC filament (which can be tracked all the way back to the LMC) is overlaid on the second filament it connects it to the two clumps near the LAF. I am planning to use the new Gaussian decomposition of the Br05 data to try to disentangle the second filament Gaussians from those of the SMC and the Bridge/SMC eastern wing. One interesting feature of the two Hɪ clumps that I believe are connected to the second MS filament is that they also connect to LA I and Arm E of the LMC. Therefore, if this connection can be made, then the LMC is the progenitor of the *entire* Magellanic Stream and Leading Arm.

4.2.6   SGS blowout from the northwest of the LMC

One of the interesting aspects of the Nidever et al. (2008) paper (Chapter 2 in this thesis) was the evidence suggesting that supergiant shells are blowing out gas from the LMC and that eventually form the MS and LAF. Since that publication I have studied the high-resolution ATCA Hɪ datacube of the LMC by Kim et al. (2003), the MCELS emission line maps of the LMC, and the MCPS optical catalog of the LMC (Zaritsky et al. 2004) to gain more insight into the LMC blowout process. Recently, I used the Gaussian decomposition of the Br05 datacube to investigate anomalous Hɪ gas in the LMC and identified what appears to be a new supergiant shell in the northwest region of the LMC that is blowing out gas to higher and lower velocities (i.e., from both sides of the disk). This evidence supports the "blowout hypothesis" and indicates that the SGS blowout is likely more common than we suspected. I hope to analyze and publish this interesting new feature in the near future.

4.2.7   More Observations at the tip of the Magellanic Stream

Our 200 deg^2 Hɪ GBT survey of the tip of the MS presented in Chapter 3 confirmed that the MS–like emission identified by Braun & Thilker (2004) was indeed an extension of the MS. It is likely that the new $\sim$140° length of the MS will be difficult for MS formation simulations to reproduce especially with the new hyperbolic orbit of the MCs (Besla et al. 2007). However, there is evidence that the MS is *even longer*. An MS that is 160–170° long might be impossible for ram pressure and tidal models to reproduce without the addition of star formation blowout or other mechanisms. The MC orbits themselves will probably be constrained by this type of data. Therefore, I am thinking of starting a new large-area ($\sim$2000 deg^2) sensitive Hɪ survey to extend the length of the MS by $\sim$30°. In order to cover the required area

and reach the necessary sensitivity to detect the MS in this region would require too much observing time on the GBT. The 100m Effelsberg radio telescope has a 7 beam L-band focal plane array that might make it a viable option for this project. However, in order to Nyquist sample such a large area at a spatial resolution of $\sim 9'$ would still require a lot of observing time. It would be possible to use the approach adopted by Braun & Thilker (2004). They used the Westbork array in auto-correlation mode to cover a 1800 deg^2 area at $\sim 50'$ resolution but with high sensitivity, and they detected MS gas emission. The advantage of the auto-correlation mode on an interferometric array is that the telescope collecting areas are effectively combined but at their native lower spatial resolution. This allows for faster coverage of large areas. On the other hand, since arrays are designed for interferometric work it might be difficult to obtain observing time for a large auto-correlation project. There are three telescope arrays in the northern hemisphere that could be used for this project: VLA, WSRT, and the GMRT. As can be seen in Table 4.2 the GMRT has the largest collecting area of the three arrays. This project will likely require ~ 300 hours of observing time in auto-correlation mode.

Table 4.2.   Comparing Telescope Facilities

Name	Diameter	Collecting Area	Resolution	Area × Resolution
	m	m^2	$'$	m^2 deg^2
GBT	100	7,854	9	555
Effelsberg	100	7,854	9	555/3,886 (1/7 beams)
WSRT	14×25	6,872	30	5,397
VLA	27×25	13,254	30	10,410
GMRT	30×45	47,713	26	28,147

4.2.8   The Stellar Periphery of the Magellanic Clouds

As previously mentioned, one of the problems that has plagued the tidal models of the MS is the lack of stars in the Stream that are predicted by the models. Starting in the late 1990s, Majewski and collaborators conducted a Washington+$DDO$51 photometric and spectroscopic survey of giant stars in a ring of fields around the Magellanic Clouds in order to search for evidence of the elusive stellar MS (Majewski 2004). The data obtained were complex and difficult to interpret, but in at least one region showed definitive Magellanic stars at large radii. Later on, in their detailed photometric and spectroscopic study of the Carina dwarf spheroidal galaxy, Muñoz et al. (2006) found a new, kinematically-cold, stellar moving group in the foreground of Carina ($\sim20°$ from the LMC) consistent with being LMC halo stars. After this discovery, I decided to undertake a large, partially-filled Washington+$DDO$51 photometric and spectrosopic survey of the Magellanic periphery (called MAPS) to try to understand this new component of the LMC better. The survey would also be able to undercover a stellar MS if one exists. The observations for the survey were completed in 2005–2007. Photometric observations for ~230 fields were taken with CTIO-4m+MOSAIC and when combined with the older Majewski survey (taken on the Swope-1m) cover ~130 deg^2 and sample an area of ~2000 deg^2. We also obtained multi-object spectroscopy for 107 fields with CTIO-4m+HYDRA, Magellan+IMACS, and du Pont+WFCCD. In total, 39 nights of observing were used to obtain the data for this survey. Figure 4.1 shows the MAPS observational coverage.

Due to the large number of photometric fields in the survey, I decided to write a pipeline to help reduce the data automatically. PHOTRED was completed in 2008 after ~8 months of developement and testing. Most of the photometric data (including the older dataset) have been reduced with PHOTRED and put on a common
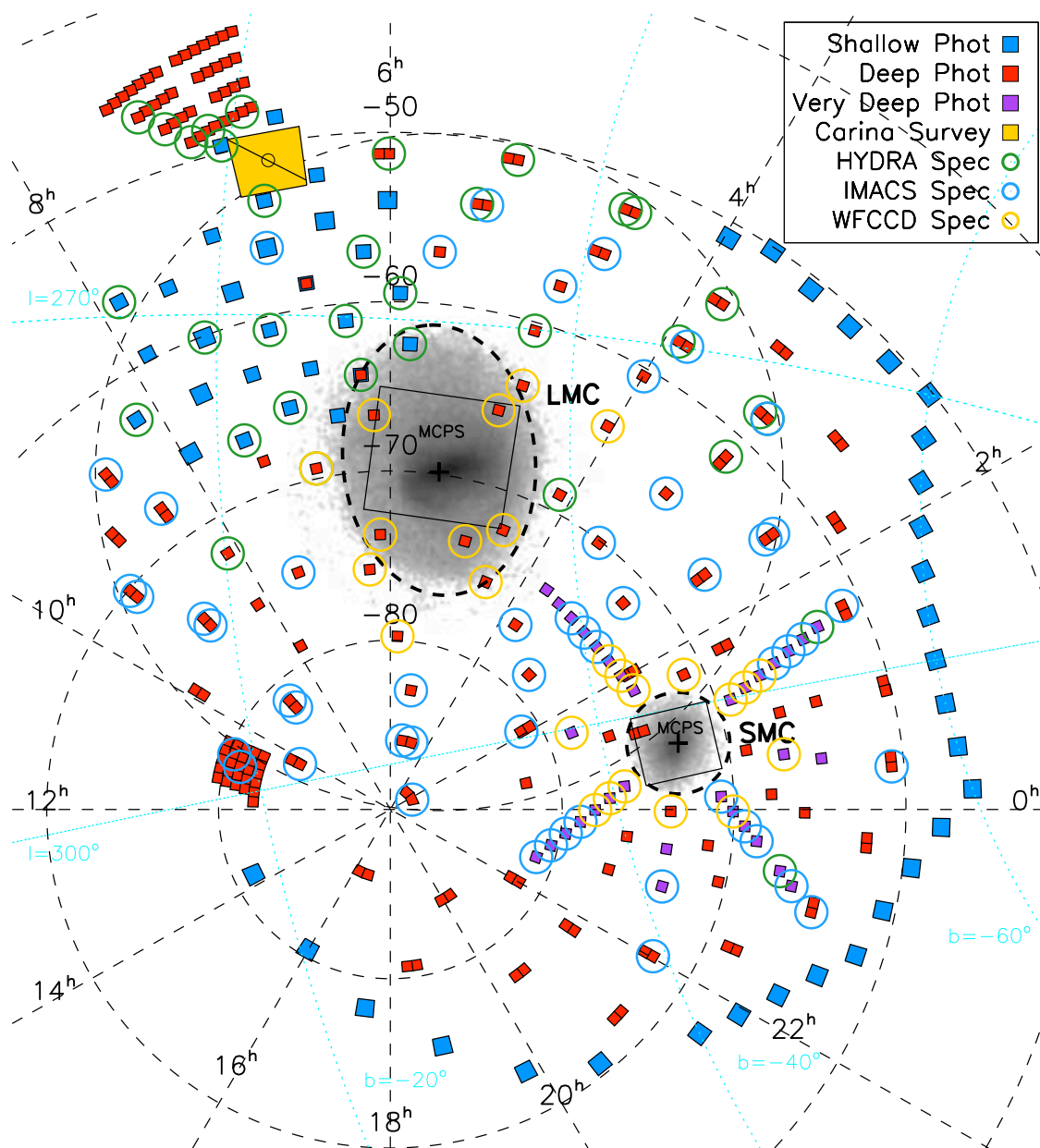
Fig. 4.1.— The observational coverage of the MAPS survey. Squares represent photometric fields: shallow Swope (blue), deep CTIO-4m+MOSAIC (red), and very deep CTIO-4m+MOSAIC (purple). Circles represent multi-object photometry: CTIO-4m+HYDRA (green), Magellan+IMACS (blue), du Pont+WFCCD (orange). The Muñoz et al. (2006) survey area of Carina is shown as an orange square. The grayscale image shows the density of red giant branch stars of the LMC and SMC from Skrutskie et al. (2006).

photometric system. All of the HYDRA spectroscopic observations (28 fields) have already been reduced, but the IMACS and WFCCD data remain to be processed. Some interesting preliminary results have already come out of the data that have been reduced and analyzed so far. At large radii from the LMC, the density of giants is so low that spectroscopic data is necessary to confirm any detection of LMC giants. LMC stars are detected in all 25 HYDRA fields around the LMC that cover a radial range of 7–23° and an azimuthal range of ∼100°. The density profile follows the LMC disk exponential in the inner region and follows a much shallower de Vaucouleurs profile at larger radii. At a radius of ∼13° the density of LMC giants is large enough to investigate with the photometry alone, and the full azimuthal coverage at this radius shows a nearly constant density suggesting that this new LMC population is in fact a stellar halo and not a stream. We have obtained metallicities from the spectra and the LMC stars show a general radial metallicity gradient. However, at large radii there is significant scatter in the metallicity suggestive of possible substructure in the LMC halo. We have also used StarFISH (Harris & Zaritsky 2001) to study the star formation history of the LMC at small radii which show a radial metallicity and age gradient.

The SMC data have not been reduced or analyzed as much as the LMC data. However, an initial analysis of the photometry shows metal-poor SMC giants extending out to at least ∼8° from the SMC center and possibly further. Once all of the spectrosopic data have been reduced the stellar halos of both the Magellanic Clouds can be studied in great detail. The photometric data of the inner SMC fields will also allow us to explore the star formation history of this galaxy. The MAPS survey will enable us to study the stellar components of the Magellanic periphery in greater detail than ever before.

References

Arnal, E. M., Bajaja, E., Larrarte, J. J., Morras, R., & Pöppel, W. G. L. 2000, A&AS, 142, 35

Bajaja, E., Cappa de Nicolau, C. E., Martin, M. C., Morras, R., Olano, C. A., & Poppel, W. G. L. 1989, A&AS, 78, 345

Bajaja, E., Arnal, E. M., Larrarte, J. J., Morras, R., Pöppel, W. G. L., & Kalberla, P. M. W. 2005, A&A, 440, 767

Barnes, D. G., et al. 2001, MNRAS, 322, 486

Battinelli, P., & Demers, S. 1998, AJ, 115, 1472

Beichman C., Neugebauer G., Habing H. J., Clegg P. E., Chester T. J., eds., 1988, IRAS Catalogues and Atlases Explanatory Supplement, NASA RP-1190, Vol. 1. GPO, Washington, DC

Belokurov, V., et al. 2006, ApJ, 642, L137

Besla, G., Kallivayalil, N., Hernquist, L., Robertson, B., Cox, T. J., van der Marel, R. P., & Alcock, C. 2007, ApJ, 668, 949

Bica, E.L.D., Schmitt, H.R., Dutra, C.M., & Oliveira, H.L. 1999, A&A, 117, 238

Bolatto, A. D., et al. 2007, ApJ, 655, 212

Braun, R., & Thilker, D. A. 2004, A&A, 417, 421 (BT04)

Brück, M. T., & Hawkins, M. R. S. 1983, A&A, 124, 216

Brüns, C., et al. 2005, A&A, 432, 45B (B05)

Brüns, C., Kerp. J., & Pagels, A. 2001, A&A, 370, L26

Bullock, J. S., & Johnston, K. V. 2005, ApJ, 635, 931

Burton, W.B. 1970, A&AS, 2, 291

Cho, H., & Kang, H., 2007, NewA, 13, 163

Cohen, R.J. 1982, MNRAS, 199, 281

Cohen, R. S., Dame, T. M., Garay, G., Montani, J., Rubio, M., & Thaddeus, P. 1988, ApJ, 331, L95

Connors, T. W., Kawata, D., Maddison, S. T., & Gibson, B. K. 2004, PASA, 21, 222

Connors, T. W., Kawata, D., & Gibson, B. K. 2006, MNRAS, 371, 108

Crane, J. D., Majewski, S. R., Rocha-Pinto, H. J., Frinchaboy, P. M., Skrutskie, M. F., & Law, D. R. 2003, ApJ, 594, L119

Da Costa, G. S. 1991, in IAU Symp. 148, The Magellanic Clouds, ed. R. Haynes & D. Milne (Dordrecht: Kluwer), 183

Davis, M., Efstathiou, G., Frenk, C. S., & White, S. D. M. 1985, ApJ, 292, 371

de Boer, K. S., Braun, J. M., Vallenari, A., & Mebold, U. 1998, A&A, 329, L49

de Heij, V., Braun, R., & Burton, W. B. 2002, A&A, 391, 159

Demers, S., & Battinelli, P. 1999, AJ, 118, 1700

Demers, S., & Battinelli, P. 1998, AJ, 115, 154

Demers, S., Grondin, L., Irwin, M. J., & Kunkel, W. E. 1991, AJ, 101, 911

Dickel, J. R., McIntyre, V. J., Gruendl, R. A., & Milne, D. K. 2005, AJ, 129, 790

Dickey, J. M., Mebold, U., Marx, M., Amy, S., Haynes, R. F., & Wilson, W. 1994, A&A, 289, 357

D'Onghia, E., & Lake, G. 2008, ApJ, 686, L61

Epchtein, N., et al. 1997, Messenger, 87, 27

Fukui, Y., et al. 1999, PASJ, 51, 745

Gardiner, L. T., Sawa, T., & Fujimoto, M. 1994, MNRAS, 266, 567

Gardiner, L. T., & Noguchi, M. 1996, MNRAS, 278, 191

Geisler, D., Bica, E., Dottori, H., Claria, J. J., Pitatti, A. E., & Santos, J. F. C., Jr. 1997, AJ, 114, 1920

Grillmair, C. J. 2006a, ApJ, 645, L37

Grillmair, C. J. 2006b, ApJ, 651, L29

Grillmair, C. J., & Dionatos, O. 2006, ApJ, 641, L37

Grondin, L., Demers, S., Kunkel, W. E., & Irwin, M. J. 1990, AJ, 100, 663

Grondin, L., Demers, S., & Kunkel, W. E. 1992, AJ, 103, 1234

Guhathakurta, P., & Reitzel, D. B. 1998 in ASP Conf. Ser. 136, Galactic Halos: A UC Santa Cruz Workshop, ed. D. Zaritsky (San Francisco: ASP), 22

Hambly, N. C., Dufton, P. L., Keenan, F. P., Rolleston, W. R. J., Howarth, I. D., & Irwin, M. J. 1994, A&A, 285, 716

Hartmann, D., & Burton, W. B. 1997, Atlas of Galactic Neutral Hydrogen, Cambridge University Press, ISBN 0521471117

Harris, J., & Zaritsky, D. 2001, ApJS, 136, 25

Harris, J. 2007, ApJ, 658, 345

Harris, J., & Zaritsky, D. 2004, AJ, 127, 1531

Haud, U. 2000, A&A, 364, 83

Haynes, M. P. 1979, AJ, 84, 8

Haynes, R. F., et al. 1991, A&A, 252, 475

Heller, P., & Rohlfs, K. 1994, A&A, 291, 743

Hibbard, J. E., Vacca, W. D., & Yun, M. S. 2000, AJ, 119, 1130

Ibata, R., Lewis, G. F., Irwin, M., Totten, E., & Quinn, T. 2001, ApJ, 551, 294

Irwin, M. J., Demers, S., & Kunkel, W. E. 1990, AJ, 99, 191

Johnston, K. V. 1998, ApJ, 495, 297

Kalberla, P. M. W., Burton, W. B., Hartmann, D., Arnal, E. M., Bajaja, E., Morras, R., & Poppel, W. G. L. 2005, A&A, 440, 775

Kalberla, P. M. W., & Haud, U. 2006, A&A, 455, 481

Kallivayalil, N., van der Marel, R. P., & Alcock, C. 2006b, ApJ, 652, 1213

Kallivayalil, N., van der Marel, R. P., Alcock, C., Axelrod, T., Cook, K. H., Drake, A. J., & Geha, M. 2006b, ApJ, 638, 772

Kaper, H. B., Smits, D. W., Schwarz, U., Takakubo, K., & van Woerden, H. 1966, Bull. Astron. Inst. Netherlands, 18, 465

Kim, S., Dopita, M. A., Staveley-Smith, L., & Bessell, M. S. 1999, A&A, 118, 2797

Kim, S., Staveley-Smith, L., Dopita, M. A., Freeman, K. C., Sault, R. J., Kesteven, M. J., & McConnell, D. 1998, ApJ, 503, 674

Kim, S., Staveley-Smith, L., Dopita, M. A., Sault, R. J., Freeman, K. C., Lee, Y., & Chu, Y.-H. 2003, ApJS, 148, 473

Klein, U., Haynes, R. F., Wielebinski, R., & Meinert, D. 1993, A&A, 271, 402

Konz, C., Brüns, C., & Birk, G. T. 2002, A&A, 391, 713

Kunkel, W. E., Irwin, M. J., & Demers, S. 1997, A&AS, 122, 463

Law, D., Johnston, K. V. & Majewski, S. R. 2005, ApJ, 617, 807

Lehner, R. 2002, ApJ, 578, 126

Lehner, R., & Howk, J. C. 2007, MNRAS, 377, 687

Lin, D. N. C., & Lynden-Bell, D. 1977, MNRAS, 181, 59

Lin, D. N. C., & Lynden-Bell, D. 1982, MNRAS, 198, 707

Lockman, F. J. 1998, Proc. SPIE, 3357, 656

Lockman, F. J., & Condon, J. J. 2005, AJ, 129, 1968

Luks, T., & Rohlfs, K. 1992, A&A, 263, 41

Majewski, S. R., Skrutski, M. F., Weinberg, M. D., & Ostheimer, J. C. 2003, ApJ, 599, 1082

Majewski, S. R. 2004, Publications of the Astronomical Society of Australia, 21, 197

Majewski, S. R., Ostheimer, J. C., Rocha-Pinto, H. J., Patterson, R. J., Guhathakurta, P., & Reitzel, D. 2004, ApJ, 615, 738

Mastropietro, C., Moore, B., Mayer, L., Wadsley, J., & Stadel, J. 2005, MNRAS, 363, 509

Mastropietro, C. 2009, IAU Symposium, 256, 117

Mathewson, D. S., Cleary, M. N., & Murray, J. D. 1974, ApJ, 190, 291

Mathewson, D. S., Ford, V. L., Schwarz, M. P., & Murray, J. D. 1979, in Proc. IAU Symp. 84, The Large-Scale Characteristics of the Galaxy, ed. W.B. Burton (Dordrecht: Reidel), 547

McGee, R. X., & Newton, L. M. 1986, PASA, 6, 471

Meaburn, J. 1984, MNRAS, 211, 521

Meaburn, J., & Blades, J. C. 1980, MNRAS, 190, 403

Meaburn, J., Marston, A.P., McGee, R. X., & Newton, L. M. 1987, MNRAS, 225, 591

Meixner, M., et al. 2006, AJ, 132, 2268

Melnick, J. 1985, A&A, 153, 235

Meurer, G. R., Bicknell, G. V., & Gingold, R. A. 1985, PASA, 6, 195

Mihos, J. C. 2001, ApJ, 550, 94

Mill, J. D., O'Neil, R. R., Price, S., Romick, G. J, Uy, O. M., & Gaposchkin, E. M. 1994, J. of Spacecraft & Rockets, 31, 900

Mizuno, N., et al. 2001, PASJ, 53, 971

Moore, B., & Davis, M. 1994, MNRAS, 270, 209

Moore, B., Ghigna, S., Governato, F., Lake, G., Quinn, T., Stadel, J., & Tozzi, P. 1999, ApJ, 524, L19

Morras, R. 1982, A&A, 115, 249

Morras, R. 1983, AJ, 88, 1

Morras, R. 1985, AJ, 90, 1801

Muller, E., Staveley-Smith, L., Zealey, W., & Stanimirović, S. 2003, MNRAS, 339, 105

Mũnoz, R. R., et al. 2006, ApJ, 649, 201

Murai, T., & Fujimoto, M. 1980, PASJ, 32, 581

Navarro, J. F., Frenk, C. S., & White S. D. M. 1996, ApJ, 462, 563

Navarro, J. F., Frenk, C. S., & White S. D. M. 1997, ApJ, 490, 493

Newberg, H. J., et al. 2002, ApJ, 569, 245

Nidever, D. L., Majewski, S. R., & Burton, W. B. 2008, ApJ, 679, 432

Odenkirchen, M., et al. 2001, ApJ, 548, L165

Olano, C. A. 2004, A&A, 423, 895

Pagel, B. E. J., & Tautvaisiene, G. 1998, MNRAS, 299, 535

Philip, A. G. D. 1976a, BAAS, 8, 532

Philip, A. G. D. 1976b, BAAS, 8, 352

Piatek, S., Pryor, C., & Olszewski, E. W. 2008, AJ, 135, 1024

Piatti, A., Sarajedini, A., Geisler, D., Bica, E., & Claria, J. J. 2002, MNRAS, 329, 556

Points, S. D., Chu, Y. H., Kim, S., Smith, R. C., Snowden, S. L., Brandner, W., & Gruendl, R. A. 1999, ApJ, 518, 298

Putman, M. E., et al. 1998, Nature, 394, 752

Putman, M. E., Staveley-Smith, L., Freeman, K. C., Gibson, B. K., & Barnes, D. G. 2003, ApJ, 586, 170 (P03)

Recillas-Cruz, E. 1982, MNRAS, 201, 473

Redman, M. P., Al-Mostafa, Z. A., Meaburn, J., & Bryce, M. 2003, MNRAS, 344, 741

Rich, R. M., Shara, M. M., & Zurek, D. 2001, AJ, 122, 842

Rocha-Pinto, H. J., Majewski, S. R., Skrutskie, M. F., & Crane, J. D. 2003, ApJ, 594, L115

Rocha-Pinto, H. J., Majewski, S. R., Skrutskie, M. F., Crane, J. D., & Patterson, R. J. 2004, ApJ, 615, 732

Rolleston, W. R. J., Dufton, P. L., McErlean, N. D., & Venn, K. A. 1999, A&A, 348, 728

Russel, S. C., & Dopita, M. A. 1992, ApJ, 384, 508

Růžička, A., Palouš, J., & Theis, C. 2007, A&A, 461, 155

Savitzky, A., & Golay, M. J. E. 1964, Analytical Chemistry 36, 1627

Schwarz, U. J., & van Woerden, H. 1974, in Galactic Radio Astronomy, eds. F.J. Kerr, & S.C. Simonson III (Dordrecht: Reidel), 45

Sembach, K. R., et al. 2003, ApJS, 146, 165

Skrutskie, M. F., et al. 2006, AJ, 131, 1163

Smecker-Hane, T. A., Cole, A. A., Gallagher, J. S., III, & Stetson, P. B. 2002, ApJ, 566, 239

Smith, A. M., Cornett, R. H., & Hill, R. S. 1987, ApJ, 320, 609

Smith, R. C., et al. 1998, PASA, 15, 163

Snowden, S. L., & Petre, R. 1994, ApJ, 436, L123

Stanimirović, S., Staveley-Smith, L., Dickey, J. M., Sault, R. J., & Snowden, S. L. 1999, MNRAS, 302, 417

Stanimirović, S., Dickey, J. M., Krčo, M., & Brooks, A. M. 2002, ApJ, 576, 773

Stanimirović, S., Hoffman, S., Heiles, C., Douglas, K. A., Putman, M., & Peek, J. E. G. 2008, ApJ, 680, 276 (S08)

Staveley-Smith, L., Kim, S., Calabretta, M. R., Haynes, R. F., & Kesteven, M. J. 2003, MNRAS, 339, 87 (S03)

Staveley-Smith, L., Soult, R. J., Hatzidimitriou, D., Kesteven, M. J., & McConnell, D. 1997, MNRAS, 289, 225

Takakubo, K., & van Woerden, H. 1966, Bull. Astron. Inst. Netherlands, 18, 488

Townsley, L. K., Broos, P. S., Feigelson, E. D., Garmire, G. P., & Getman, K. V. 2006, AJ, 131, 2140

van den Bergh, S. & Tammann, G. A. 1991, ARA&A, 29, 363

van der Marel, R. P. 2001, AJ, 122, 1827

van der Marel, R. P., Alves, D. R., Hardy, E., & Suntzeff, N. B. 2002, AJ, 124, 2639 (vdM02)

Wakker, B. P. 2001, ApJS, 136, 463

Wakker, B. P. 2004, in High-Velocity Clouds, eds. H. van Woerden, B. P. Wakker, U. Schwarz, & K. de Boer (Dordrecht: Kluwer), 25

Wakker, B. P., Oosterloo, T. A., & Putman, M. E. 2002, AJ, 123, 1953

Wannier, P., & Wrixon, G.T. 1972, ApJ, 173, 119

Wannier, P., Wrixon, G. T., & Wilson, R. W. 1972, A&A, 18, 224

Wayte, S. R. 1989, Proceedings of the Astronomical Society of Australia, 8, 195

Weinberg, M. D., & Nikolaev, S. 2001, ApJ, 548, 712

Westmeier, T., & Koribalski, B. S. 2008, MNRAS, 388, L29

White, S. D. M., & Rees, M. J. 1978, MNRAS, 183, 341

Williams, D. R. W. 1973, A&AS, 8, 505

Woosley, S. E., & Weaver, T. A. 1986, ARA&A, 24, 205

Wright, M. C. H. 1979, ApJ, 233, 35

Xu, C., Klein, U., Meinert, D., Wielebinski, R., & Haynes, R. F. 1992, A&A, 257, 47

Yamaguchi, R., et al. 2001, PASJ, 53, 985

Yanny, B., et al. 2003, ApJ, 588, 824

Yoshizawa, A. M., & Noguchi, M. 2003, MNRAS, 339, 1135

Young, J. S., & Scoville, N. Z. 1991, ARA&A, 29, 581

Zaritsky, D., Harris, J., Thompson, I. B., Grebel, E. K., & Massey, P. 2002, AJ, 123, 855

Zaritsky, D., Harris, J., Thompson, I. B., & Grebel, E. K. 2004, AJ, 128, 1606